

Fundamental parameters of QCD from non-perturbative methods for two and four flavors

DISSERTATION

zur Erlangung des akademischen Grades

doctor rerum naturalium (Dr. Rer. Nat)
im Fach Physik

eingereicht an der
Mathematisch-Naturwissenschaftlichen Fakultät I
Humboldt-Universität zu Berlin

von

Dipl.-Phys. Marina Marinković

Präsident der Humboldt-Universität zu Berlin:
Prof. Dr. Jan-Hendrik Olbertz

Dekan der Mathematisch-Naturwissenschaftlichen Fakultät I:
Prof. Dr. Stefan Hecht

Gutachter:

1. Prof. Dr. Ulrich Wolff
2. Dr. Rainer Sommer
3. Prof. Dr. Laurent Lellouch

eingereicht am: 15.04.2013

Tag der mündlichen Prüfung: 31.05.2013

*To my sister
and to the other strong women in my life,
who have always been my inspiration*

Abstract

The non-perturbative formulation of Quantumchromodynamics (QCD) on a four dimensional space-time Euclidean lattice together with the finite size techniques enable us to perform the renormalization of the QCD parameters non-perturbatively. In order to obtain precise predictions from lattice QCD, one needs to include the dynamical fermions into lattice QCD simulations. We consider QCD with two and four mass degenerate flavors of $O(a)$ improved Wilson quarks.

In this thesis, we improve the existing determinations of the fundamental parameters of two and four flavor QCD. In four flavor theory, we compute the precise value of the Lambda parameter in the units of the scale L_{max} defined in the hadronic regime. We also give the precise determination of the Schroedinger functional running coupling in four flavour theory and compare it to the perturbative results. The Monte Carlo simulations of lattice QCD within the Schroedinger Functional framework were performed with a platform independent program package Schroedinger Funktional Mass Preconditioned Hybrid Monte Carlo (SF-MP-HMC), developed as a part of this project.

Finally, we compute the strange quark mass and the Lambda parameter in two flavour theory, performing a well-controlled continuum limit and chiral extrapolation. To achieve this, we developed a universal program package for simulating two flavours of Wilson fermions, Mass Preconditioned Hybrid Monte Carlo (MP-HMC), which we used to run large scale simulations on small lattice spacings and on pion masses close to the physical value.

Abstract

Die nicht perturbative Formulierung der Quantenchromodynamik (QCD) auf dem vierdimensionalen euklidischen Gitter in Zusammenhang mit der sogenannten Finite-Size-Scaling Methode ermöglicht die nicht-perturbative Renormierung der QCD-Parameter. Um praezise Vorhersagen aus der Gitter-QCD zu erhalten, ist es noetig, die dynamischen Fermion-Freiheitsgrade in den Gitter-QCD-Simulationen zu beruecksichtigen. Wir betrachten QCD mit zwei und vier $O(a)$ -verbesserten Wilson-Quark-Flavours, wobei deren Masse degeneriert ist.

In dieser Dissertation verbessern wir die vorhandenen Bestimmungen des fundamentalen Parameters der Zwei- und Vier-Flavor-QCD. In der Vier-Flavor-Theorie berechnen wir den praezisen Wert des Lambda-Parameters in Einheiten der Skale L_{max} , welche im hadronischen Bereich definiert ist. Zudem geben wir auch die praezise Bestimmung der laufenden Schroedinger-Funktional-Kopplung in Vier-Flavor-Theorie an sowie deren Vergleich zu perturbativen Resultaten. Die Monte-Carlo-Simulationen der Gitter-QCD in der Schroedinger-Funktional-Formulierung wurden mittels der plattform-unabhaengigen Software Schroedinger-Funktional-Mass-Preconditioned-Hybrid-Monte-Carlo (SF-MP-HMC) durchgefuehrt, die als Teil dieses Projektes entwickelt wurde.

Schliesslich berechnen wir die Masse des Strange-Quarks und den Lambda-Parameter in Zwei-Flavor-Theorie, wobei die voll-kontrollierte Kontinuums- und chirale Extrapolation zum physikalischen Punkt durchgefuehrt wurden. Um dies zu erreichen, entwickeln wir eine universale Software fuer Simulationen der zwei Wilson-Fermionen-Flavor mit periodischen Randbedingungen, namens Mass-Preconditioned-Hybrid-Monte-Carlo (MP-HMC). Die MP-HMC wird verwendet um Simulationen mit kleinen Gitterabstaenden und in der Naehة der physikalischen Pionmasse ausfuehrlich zu untersuchen.

Contents

1	Introduction	1
2	Quantum Chromodynamics on the Lattice	7
2.1	Continuum QCD	8
2.2	Lattice formulation of QCD	9
2.3	Pure gauge action on the lattice	12
2.4	Wilson discretization of the fermion action	12
2.5	O(a) improved action	16
2.6	Renormalization	18
2.6.1	Renormalization of Wilson fermions	21
2.7	Continuum limit	21
3	Lattice QCD Simulations	23
3.1	Importance sampling	23
3.2	The Monte Carlo method and the Metropolis algorithm	24
3.2.1	Metropolis algorithm	25
3.3	Molecular Dynamics method	27
3.4	Hybrid Monte Carlo Algorithm	28
3.5	Integration of MD equations of motion	29
3.5.1	Leap-frog integrator	29
3.5.2	Omelyan-Mryglod-Folk integrator	30
3.6	HMC for the Wilson gauge theory	31
3.7	Including dynamical fermions in simulations	33
3.8	Algorithm preconditioning	36
3.8.1	Multiple Time Scales	38
3.8.2	Domain Decompositioning	40
3.8.3	Hasenbusch Preconditioning	41
4	MP-HMC program package	43
4.1	DD-HMC overview	44
4.2	Algorithmic choices in MP-HMC	45
4.2.1	Fermionic Forces	46
4.2.2	HMC stability and safety measures	57

Contents

4.3	Performance	59
4.3.1	Timings and scaling of the MP-HMC package	59
4.3.2	Comparison of DD-HMC and MP-HMC	62
4.3.3	Large scale simulations with MP-HMC	63
5	Schrödinger Functional	65
5.1	Non-perturbative renormalization	65
5.2	SF Renormalization Scheme	66
5.3	Renormalized coupling	69
5.4	Step scaling function	70
5.5	The $O(a)$ improved Wilson action with SF boundary conditions . .	71
5.6	Algorithmic challenges with SF formulation	73
5.6.1	Program package SF-MP-HMC: stability and scalability . . .	74
6	Running coupling in $N_f=4$ theory	77
6.1	Lattice step scaling function	77
6.2	Motivation for precise computation of $N_f=4$ running coupling . . .	79
6.3	Non-perturbative $O(a)$ improvement coefficients for $N_f=4$ theory .	80
6.3.1	Non-perturbative determination of c_A	82
6.3.2	Other $O(a)$ improvement coefficients in $N_f=4$ simulations .	85
6.4	Previous computation of the running coupling in $N_f=4$ Wilson QCD	86
6.4.1	Tuning criteria for the PCAC mass	87
6.5	New result of the running coupling in $N_f=4$ theory	90
6.5.1	Simulations	90
6.5.2	Improved lattice step scaling function	90
6.5.3	Continuum limit of the SSF	93
6.5.4	Cutoff effects	96
6.5.5	Running coupling	96
7	The strange quark mass and the Lambda parameter for $N_f=2$ theory	101
7.1	Lattice parameters	102
7.2	Setting the scale from f_K	102
7.2.1	Partially quenched SU(3) Chiral Perturbation Theory (Strategy 1)	103
7.2.2	SU(2) Chiral Perturbation Theory (Strategy 2)	107
7.3	Determination of the Lambda parameter	109
7.3.1	Continuum value of the Lambda parameter	109
7.4	Determination of the strange quark mass	111
7.4.1	Strange quark mass in the continuum limit	113
8	Conclusions and outlook	115

Appendix A	119
1 Chiral representation of gamma matrices	119
2 SU(3) group and su(3) algebra	120
Appendix B	121
3 Inverse of Qs via Q inverse	121
4 Hasenbusch preconditioning for Npf=3 pseudofermions	122
5 Run parameters of the Nf=2 ensembles produced with DD- and MP-HMC	123
Appendix C	125
6 Limits for the tuning of the PCAC mass	125
7 Tuning of the kappa critical on the new parameter sets	125
Appendix D	129
8 Error analysis	129
8.1 Autocorrelations	129
8.2 Autocorrelation function of the SF coupling	129
8.3 Improved error analysis of lattice QCD simulations	130
9 Observables used in chapter 7	131
Acknowledgments	133
Bibliography	145
List of Figures	148
List of Tables	150

1 Introduction

There are four fundamental interactions in nature: gravitational, electromagnetic, weak and strong. The Standard Model (SM) is the theory of elementary particles that provides unified description of three of them: electromagnetic, weak and strong nuclear interaction. It was developed throughout the last century and the current formulation was completed in the mid 1970s upon experimental confirmation of the existence of quarks. High energy experiments in the last decades found agreement with almost all predictions of the Standard Model. Even the mechanism of the spontaneous breaking of the symmetry of the electroweak force through which the quarks and leptons acquire their masses is confirmed, so far, in the recent findings from the LHC experiments running at CERN[1, 2] and will be tested more precisely as time goes on.

An important part of the Standard Model is the theory that describes strong nuclear interaction - Quantum Chromodynamics (QCD). This theory with local symmetry and only few parameters provides a description of strong interaction phenomena from very small distances (high energies) to large distances (low energies). QCD postulates the existence of two types of fundamental strongly interacting fields: quarks, as constituents of all nuclear matter, and gluons, as mediators of the interactions between the quarks. Gluons live in the adjoint representation of the SU(3) group, whereas quarks are in the fundamental SU(3) representation.

The strength of the gluon coupling to the quarks is parametrized with the dimensionless parameter g , which is subject to renormalization in the full quantum theory. Let us define a quantity that measures the strength of the interaction accounting for the energy dependence and call it a renormalized or physical coupling \bar{g} . The asymptotic expression of the corresponding *strong coupling constant* α_s , as a function of the scale μ , is given by [3]

$$\alpha_s(\mu) = \frac{\bar{g}^2(\mu)}{4\pi} = \frac{1}{4\pi} \frac{1}{b_0 \ln(\mu^2/\Lambda^2)} \left[1 - \frac{b_1}{b_0^2} \frac{\ln(\ln \mu^2/\Lambda^2)}{\ln(\mu^2/\Lambda^2)} + \mathcal{O}\left(\frac{1}{(\ln(\mu^2/\Lambda^2))^2}\right) \right], \quad (1.1)$$

with b_0 and b_1 being universal constants

$$b_0 = \frac{1}{(4\pi)^2} \left(11 - \frac{2}{3} N_f \right), \quad b_1 = \frac{1}{(4\pi)^4} \left(102 - \frac{38}{3} N_f \right). \quad (1.2)$$

1 Introduction

We quote here the two-loop coefficients[4, 5] that are independent of the renormalization scheme. The terms of $\mathcal{O}(\frac{1}{(\ln(\mu^2/\Lambda^2))^2})$ are scheme dependent and will be discussed later in this work. Λ denotes a low energy QCD scale at which the above asymptotic expansion breaks and it can be seen as a fundamental QCD parameter equivalent to the coupling itself. It is therefore also called the *Lambda parameter* of QCD.

The logarithmic decay of the coupling α_s reflects an important property of QCD, which is referred to as *asymptotic freedom*[6, 7]. Namely, as one moves towards higher energies, the coupling becomes increasingly weak and, in the region above the GeV scale, a systematic perturbative expansion in powers of the coupling is applicable and yields reliable results for the observables of interest in this regime.

Another crucial aspect of QCD is that quarks and gluons cannot be observed directly. This phenomenon is known as *confinement*. Quarks have never been observed isolated, instead they always appear as constituents of bound-state hadrons. All physical states are invariant with respect to the SU(3) group (color singlets).

At low energies, the QCD force becomes stronger. The associated increase in coupling consequently renders the perturbative expansion not feasible. It is thus necessary to develop the non-perturbative methods in order to study the low energy properties of QCD.

A way to study QCD at all energy scales from first principles is to formulate the theory on a four dimensional space-time Euclidean lattice, with lattice spacing a . This approach to QCD is known under the name of *lattice QCD*. In lattice QCD, the theory is regularized in a non-perturbative way and the inverse lattice spacing naturally imposes a cutoff at a^{-1} . Such a system can then be regarded as a statistical physics model and techniques from statistical mechanics can be applied. Since its original formulation in [8], lattice QCD has been a very powerful tool to study QCD, especially its non-perturbative nature. Due to the large number of degrees of freedom arising from the discretization of space-time, in practice, QCD on the lattice is mainly studied by means of computer simulations.

In the early days of lattice QCD simulations, the dynamical quark effects were neglected. Namely, lattice QCD simulations get computationally very expensive if the quark dynamics are directly incorporated in the numerical calculations. The reason why the dynamical fermion simulations are so costly is the non-locality of the fermion determinant and the so-called *critical slowing down*. The latter refers to an increase in computational effort while approaching critical points of a theory, beyond the naive scaling with the number of degrees of freedom of the system. To ensure the efficiency and correctness of the required dynamical fermion simulations, lattice QCD is closely related to the theoretical development and practical implementation of suitable Monte Carlo algorithms and high performance computers.

In this work, lattice QCD will be used to make non-perturbative predictions of QCD parameters in the low energy sector of QCD and to connect this sector to the perturbative high energy regime. The non-perturbative formulation of QCD on the lattice in combination with the finite size techniques, which will be discussed later in more detail, enable us to perform the renormalization of the QCD parameters non-perturbatively. One could wonder why this is needed. Namely, besides the fact that the QCD coupling becomes weak in ultraviolet, the asymptotic freedom also implies that the bare coupling goes to zero in the continuum limit. One would then naively expect to be able to compute the QCD parameters as power series in the bare coupling $g_0^2 \rightarrow 0$, while approaching the continuum limit $a \rightarrow 0$. However, this is not feasible due to the following practical point: if one wants to invest a realistic computational effort, even with modern supercomputers, there is a clear limit to the number of degrees of freedom that can be included in a simulation. This practical limitation does not allow us to choose a lattice spacing for the simulation that is much smaller than the relevant physical scales of the observable that we are interested in. Therefore, the momentum scale a^{-1} is not always large enough to justify the truncation of the perturbative series. Hence, if one wants to obtain reliable non-perturbative predictions in the low-energy sector of QCD, the renormalization should be done non-perturbatively as well.

The mentioned agreement of the SM with the experiment indicates that the new physics can only be hiding in relatively small effects beyond the Standard Model. Accordingly, precision theory is needed to test the Standard Model in even more detail. Lattice QCD, with its tools for non-perturbative renormalization, allows for a precise determination of the fundamental parameters of QCD from static experimental data, e.g. the kaon decay constant, f_K , and a few flavored pseudoscalar meson masses.

Computation of the fundamental QCD parameters has been a topic of intensive study for many lattice QCD collaborations (see for example [9–14]¹). Over the last two decades, the ALPHA Collaboration[16], of which the author of this work is a member, has been devoted to the precise calculation of fundamental QCD parameters [17–21] by employing the recursive finite size technique. The application of this technique had been proposed and demonstrated in Refs.[22, 23]. Presently, there is no alternative approach that can guarantee to reach reliable and precise numbers, while keeping systematic errors fully under control.

The application of non-perturbative renormalization in determining the fundamental parameters of QCD is the main motivation of this work. The importance of the precise determination of the fundamental QCD parameters will be demonstrated here with the example of the Lambda parameter. In Table 1.1 both non-perturbative and perturbative estimations of the value of the Lambda parameter

¹ The list of references is taken over from the latest PDG[15].

1 Introduction



N_f	Λ	Experiment	Theory
0	238(19)	$m_K, K \rightarrow \mu \nu_\mu, ; K \rightarrow \pi \mu \nu_\mu$	LGT,  [19]
2	310(25)	$m_K, K \rightarrow \mu \nu_\mu, ; K \rightarrow \pi \mu \nu_\mu$	LGT,  [24]
5	160(11)	DIS, HERA, ...	NNLO PT, fits to PDFs [25]
5	198(16)	DIS, HERA, ...	NNLO PT, fits to PDFs [26]
5	275(57)	$e^+e^- \rightarrow \text{hadrons}$, LEP	4-loop PT at M_Z

Table 1.1: Determination of the Lambda parameter from lattice gauge theory ($N_f = 0$ and $N_f = 2$) by the ALPHA Collaboration and perturbation theory estimations with different experimental input, for $N_f = 5$. For comparison, all given values of Λ are converted to the $\overline{\text{MS}}$ renormalization scheme. The first two rows indicate strong dependence of the Lambda parameter on the number of dynamical flavors in lattice simulations. The three results for $\Lambda_{\overline{\text{MS}}}(N_f = 5)$ obtained from perturbation theory disagree among themselves by more than one standard deviation.

are shown. The present precision for $N_f = 2$, achieved by our collaboration, is already comparable with the phenomenological determinations - if not better.

Previous determinations of the Lambda parameter from lattice QCD show a significant dependence on the number of dynamical quark flavors in the simulation (cf. $N_f = 0$ and $N_f = 2$ in Table 1.1). Therefore, it was very important to complete the program of the determination of the fundamental lattice parameters for $N_f = 2$ (one of the focuses of this thesis) and to make progress towards completing the precise computation for $N_f = 4$ dynamical flavors, which may then be perturbatively connected to e.g. 5-flavor $\overline{\text{MS}}$ coupling. That would give a final and most precise theoretical estimate of the Lambda parameter and resolve the discrepancy of its current phenomenological estimations (cf. Table 1.1). The goal of this work is to

- Give a final result for the strange quark mass and the Lambda parameter in two flavour theory, performing a well-controlled continuum limit and chiral extrapolation. To achieve this, we will have to develop a universal program package for simulating two flavours of Wilson fermions, which will need to run large scale simulations on small lattice spacings a on pion masses close to the physical value.
- Give a more precise determination of the running coupling in four flavour theory than it was done in [21]. For the successful realization of this part, a development of a dedicated program package is also needed.

This work reports on significant progress that has been made on both of these fronts. It is organized as follows: In the succeeding chapter, we give a brief introduction to the formulation of QCD on the lattice. After discussing the fermion formulation used in this work, namely Wilson fermions, we will explain the $O(a)$ improvement which is an important ingredient of our study. In the third chapter, we introduce the most frequently used algorithm for lattice QCD simulations, the Hybrid Monte Carlo (HMC) algorithm. In this chapter we also discuss the algorithmic advances that made the simulations including fermions at near-physical quark masses and small lattice spacings possible, the so-called preconditioning of the HMC algorithm.

Chapter 4 deals with our implementation of the mass preconditioned HMC algorithm (MP-HMC program package). This chapter describes the algorithmic choices we made in order to speed up of the simulations with $O(a)$ improved Wilson quarks.

Next, we give the theoretical foundations of the Schrödinger functional (SF) renormalization scheme on the lattice, which allows for a fully non-perturbative renormalization of QCD to be performed. For the purpose of computing the running of the coupling in the SF renormalization scheme, we develop an extension of the MP-HMC algorithm with SF boundary conditions (SF-MP-HMC) and describe its main features at the end of the Chapter 5.

In Chapter 6 we discuss the energy dependence of the QCD coupling with four flavors of $O(a)$ improved Wilson quarks in the Schrödinger functional scheme. In order to convert the obtained results to physical units, one has to determine the lattice spacing in the large scale simulations with four flavors of dynamical fermions. Performing this procedure systematically for $N_f = 4$ theory is beyond the scope of this thesis and requires the commitment of a large team of lattice physicists in the following years. Therefore, in Chapter 7, we illustrate the process of determining the fundamental parameters of QCD with the example of the $N_f = 2$ theory. The summary and outlook of this work are given in Chapter 8.

2 Quantum Chromodynamics on the Lattice

If one wants to solve the path integrals in theories with a large number of degrees of freedom, such as QCD, then applying numerical methods is a natural way to go. The numerical evaluation cannot be used for the vacuum expectation values (v.e.v.) of the products of fields in Minkowski space, since the oscillations of the complex weight in this formulation make the stochastic evaluation impossible. On the other hand, the formulation of the set of axioms that describe the correlation functions in Euclidean space by Osterwalder and Schrader [27, 28] has allowed for an analytic continuation of the Minkowski v.e.v. to the Euclidean Green function. After the continuation to imaginary time, the functional integral is interpreted as an average of the Euclidean field configuration space. The v.e.v. of a two point function is then given by

$$\langle \phi_1(x_1)\phi_2(x_2) \rangle = \frac{1}{Z} \int [D\phi] \phi_1(x_1)\phi_2(x_2) e^{-S^E[\phi]}. \quad (2.1)$$

The weight in this integral can be interpreted as the Boltzmann probability $e^{-S^E[\phi]}$ of the classical Euclidean action $S^E[\phi]$, whereas Z represents the partition function of the same statistical system

$$Z = \int [D\phi] e^{-S^E[\phi]}. \quad (2.2)$$

The details of performing the above integrations numerically, with the help of Monte Carlo simulations, will be discussed in chapter 3. We mentioned it here in order to motivate the exclusive usage of the Euclidean formulation throughout this work. Therefore, in the following the superscript “E” will be omitted and all the expressions that we are about to give are defined in the Euclidean space-time.

After a brief reminder of the (Euclidean) continuum QCD action and its properties, in this chapter we give a short introduction into the lattice formulation of QCD, with a focus on the discretization proposed by Wilson[8]. For detailed insight into the subject and many different discretization approaches that are not covered here, we refer the reader to the following textbooks [29–33] and reviews [34–36].

2.1 Continuum QCD

The action of QCD in the continuum is given by

$$S_{QCD}[\psi, \bar{\psi}, A] = S_F[\psi, \bar{\psi}, A] + S_G[A] \quad (2.3)$$

$$\begin{aligned} &= \sum_{f=1}^{N_f} \int d^4x \bar{\psi}^{(f)}(x) (\gamma_\mu (\partial_\mu + iA_\mu(x)) + m^{(f)}) \psi^{(f)}(x) \\ &+ \frac{1}{4} \sum_{i=1}^8 \int d^4x F_{\mu\nu}^{(i)}(x) F_{\mu\nu}^{(i)}(x), \end{aligned} \quad (2.4)$$

where $\psi^{(f)}$ and $\bar{\psi}^{(f)}$ describe the quark and antiquark fields at the space-time position x , coupled to the gauge field A_μ through minimal coupling. Quarks are spin 1/2 particles and have 12 independent components (4 Dirac \times 3 color components). The flavor index runs from 1 to the number of quark flavors N_f and the mass of the corresponding quarks is denoted with $m^{(f)}$. QCD postulates six flavors of quarks: up, down, strange, charm, bottom and top. For the computation of many observables, it is often enough to include a certain number (N_f) of the lightest quarks. For example, when we take into account only the dynamical effects of u and d quarks, we are talking about the $N_f = 2$ approximation of QCD, which will in the following be referred to simply as the $N_f = 2$ theory, etc.

The local gauge symmetry group of QCD is the non-Abelian color group $SU(3)$. Local rotations in color space $\Omega(x) \in SU(3)$ give the transformation law for color fields at each space-time point x

$$\psi(x) \rightarrow \psi'(x) = \Omega(x)\psi(x), \quad \bar{\psi}(x) \rightarrow \bar{\psi}'(x) = \bar{\psi}(x)\Omega^\dagger(x). \quad (2.5)$$

The gauge principle requires that the action and the measure for ψ and $\bar{\psi}$ is invariant under the gauge group transformation. This request is equivalent to defining the *covariant derivative*

$$D_\mu(x) = \partial_\mu + iA_\mu(x) \quad (2.6)$$

and, as the name says, imposing its invariance under the local gauge transformations

$$D'_\mu \rightarrow D_\mu(x) = \partial_\mu + iA'_\mu(x) = \Omega(x)D_\mu(x)\Omega^\dagger(x). \quad (2.7)$$

From eq. 2.7 we can derive the transformation law for the gauge fields in continuum

$$A_\mu(x) \rightarrow A'_\mu(x) = \Omega(x)A_\mu(x)\Omega^\dagger(x) + i(\partial_\mu\Omega(x))\Omega^\dagger(x). \quad (2.8)$$

2.2 Lattice formulation of QCD

In addition to the obtained local gauge invariance of the fermion part of the continuum QCD action, we have to make sure that the gauge part of the action has the same property. This is achieved by defining the field strength tensor $F_{\mu\nu}(x)$ from eq. 2.4 as the commutator of covariant derivatives

$$F_{\mu\nu} = -i[D_\mu(x)D_\nu(x)]. \quad (2.9)$$

It can be verified with a simple manipulation that

$$F_{\mu\nu}(x) \rightarrow F'_{\mu\nu}(x) = \Omega(x)F_{\mu\nu}\Omega^{-1}(x). \quad (2.10)$$

and therefore the full QCD action given in equation 2.4 satisfies the equivalence

$$S_{\text{QCD}}[\psi, \bar{\psi}, A] = S_{\text{QCD}}[\psi', \bar{\psi}', A'] \quad (2.11)$$

under the transformations given in equations 2.5 and 2.8. The commutation relations of the γ_μ matrices and their representation used in this thesis are given in appendix 1.

2.2 Lattice formulation of QCD

One way to regularize QCD is to formulate it on a four dimensional space-time Euclidean lattice. The four dimensional space-time continuum gets replaced by a hyper-cubic discrete grid of points with finite distance a , the *lattice spacing*. The quark and antiquark fields are restricted to the sites of the discretized space-time lattice $x_\mu = an_\mu$, $n_\mu = 0, 1, \dots, N_\mu - 1$, $\mu = 0, \dots, 3$, where the convention of using the zeroth direction as the time is introduced and N_μ denotes the number of lattice points in the direction μ . As well as in the continuum formulation, quark and antiquark fields $\psi(x)$ and $\bar{\psi}(x)$ carry color, Dirac and flavor indices. The regularization parameter a^{-1} serves as a momentum cutoff that modifies the theory at short distances and renders UV divergences finite. The introduction of the finite lattice spacing a breaks some symmetries, but we already try to keep as many as possible in the discretized theory. For example, the rotational symmetry obviously gets replaced by a hyper-cubic symmetry and the original symmetry is recovered in the continuum limit $a \rightarrow 0$, i.e. when the cutoff is removed. On the other hand, we are able to retain the local gauge invariance in the lattice formulation. Following a similar reasoning as for the construction of the gauge invariant action in the continuum QCD, we achieve the local $SU(3)$ invariance through an adequate introduction of the gluon fields. Derivatives on the lattice become finite difference operators. Let us use $\hat{\mu}$ to denote a *unit vector* in the direction μ . We can define the forward and backward gauge invariant derivatives acting on the

2 Quantum Chromodynamics on the Lattice

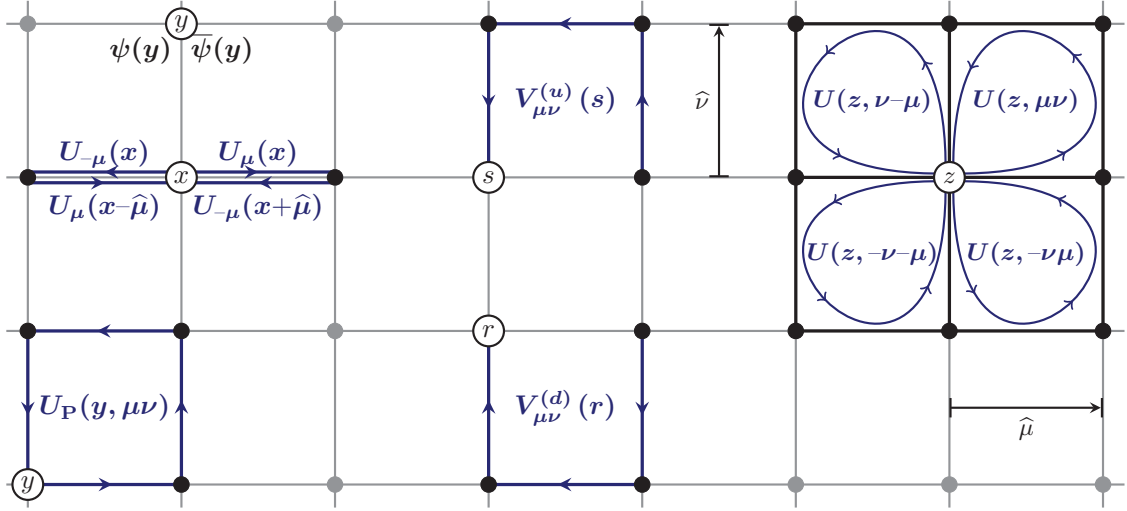


Figure 2.1: Illustration of the two dimensional lattice, with characteristic objects that are addressed in sections 2.2 and 2.3. Fermion fields are placed in the lattice points, while the gauge fields (links) connect the neighboring lattice points. In the lower left angle we have *plaquette* - an elementary loop on the lattice. The upper right corner contains the so-called *clover* contribution to the fermion action, which is introduced in section 2.5.

2.2 Lattice formulation of QCD

fermion fields on the lattice in the following way

$$\nabla_\mu \psi(x) = \frac{1}{a} [U_\mu(x) \psi(x + \hat{\mu}) - \psi(x)], \quad (2.12)$$

$$\nabla_\mu^* \psi(x) = \frac{1}{a} [\psi(x) - U_\mu^{-1}(x - \hat{\mu}) \psi(x - \hat{\mu})], \quad (2.13)$$

where $U_\mu(x)$ represents the parallel transporter of the field $\psi(x + \hat{\mu})$ along the link that connects it to $\psi(x)$. One can easily verify that this choice of the derivatives ensures that the quark fields transform under eq. 2.5 in the same way if the link parallel transporter $U_\mu(x)$ has the following transformation property

$$U_\mu(x) \rightarrow U'_\mu(x) = \Omega(x) U_\mu(x) \Omega^\dagger(x + \hat{\mu}). \quad (2.14)$$

$U_\mu(x)$ is an $SU(3)$ matrix assigned to the segment that connects neighboring sites on the lattice: x and $x + \hat{\mu}$. In Figure 2.1, we illustrate the *gauge links* and their property

$$U_\mu(x) = U_{-\mu}^\dagger(x + \hat{\mu}), \quad U_\mu(x - \hat{\mu}) = U_{-\mu}^\dagger(x), \quad (2.15)$$

together with some other objects that they can form on the lattice, which will be used in the subsequent sections. The relation between the matrix representation of the parallel transporters and the continuum gauge field is given by

$$U_\mu(x) = \mathcal{P} \{ e^{a \int_0^1 dt A_\mu(x + (1-t)\hat{\mu})} \} \quad (2.16)$$

$$= \mathbf{1} + a A_\mu(x) + O(a^2). \quad (2.17)$$

where \mathcal{P} preserves path-ordering of the exponentials, needed in the case of non-Abelian gauge groups, such as $SU(3)$.

2.3 Pure gauge action on the lattice

A gauge invariant action on the lattice was first put forward by Wilson[8]. For the discretized action, we need a local object defined on the lattice that is gauge invariant at the same time. The most simple choice is the so called *plaquette variable* which is the oriented product of parallel transporters around an elementary square on the lattice

$$U_P(x, \mu\nu) = U_\mu(x)U_\nu(x + \hat{\mu})U_\mu^{-1}(x + \hat{\nu})U_\nu^{-1}(x). \quad (2.18)$$

The plaquette variable is depicted in the lower left corner of Figure 2.1. The *Wilson gauge action* (also known as the Wilson plaquette action) is then given by

$$\begin{aligned} S_W[U] &= \beta \sum_x \sum_{\mu\nu, \mu \neq \nu} S_P(U_P(x, \mu\nu)) \\ S_P(U_P) &= 1 - \frac{1}{3} \text{Re Tr} U_P. \end{aligned} \quad (2.19)$$

where the summation is done over all plaquettes and $\beta = 2N/g_0^2$ for the $SU(N)$ gauge group. In the case of the color gauge group $SU(3)$ of QCD, we have $\beta = 6/g_0^2$. It can be shown that the Wilson gauge action reduces to the continuum Yang-Mills action in the naive continuum limit $a \rightarrow 0$, with the discretization errors of $O(a^2)$

$$S_G[U] = \frac{a^4}{2g_0^2} \sum_x \sum_{\mu\nu} \text{Tr} F_{\mu\nu}^2(x) + O(a^2). \quad (2.20)$$

This is the simplest gauge invariant discretization of the QCD action. In principle, it is possible to construct the gauge invariant action using arbitrary closed loops. However, one must make sure that it is appropriately averaged over all orientations and space-time translations, such that it reproduces the space-time symmetries when the continuum limit $a \rightarrow 0$ is taken. All such actions will differ only at the order $O(a^2)$. It is also possible to use the linear combination of differently shaped closed loops, such that the leading cutoff effects are canceled. This is known as the construction of the *improved actions* and although we will exclusively use the discussed Wilson formulation of the gauge action in this work (eq. 2.19), we use a similar strategy for improving the fermion action in section 2.5.

2.4 Wilson discretization of the fermion action

Before we discuss the lattice discretization of fermion action used in this work, let us take a quick look at some general issues that the discretization of the fermion action faces. A simple way to regularize the Dirac operator is the so-called naive

2.4 Wilson discretization of the fermion action

discretization of fermions on a lattice. One replaces the partial derivatives from the fermion part of QCD action (cf. eq. 2.4) with the symmetric combination of finite differences defined in eq. 2.13 and obtains

$$S_F^{naive} = a^4 \sum_x \bar{\psi}(x) \left(\gamma_\mu \frac{\nabla_\mu + \nabla_\mu^*}{2} + m \right) \psi(x), \quad (2.21)$$

where m denotes the bare quark mass from the original Lagrangian. It turned out that it is a highly non-trivial problem to regularize the Dirac operator in a way that preserves the chiral symmetry without violating other fundamental field theoretic properties, such as locality. In order to simplify the following considerations, we will first discuss the discretization of the Dirac operator on the case of the free Dirac particle. If we replace $U_\mu(x)$ with the trivial gauge fields $U_\mu(x) = \mathbb{1}$, the covariant derivatives ∇_μ, ∇_μ^* become naive lattice derivatives $\tilde{\nabla}_\mu, \tilde{\nabla}_\mu^*$:

$$\tilde{\nabla}_\mu \psi(x) = \frac{1}{a} [\psi(x + \hat{\mu}) - \psi(x)], \quad (2.22)$$

$$\tilde{\nabla}_\mu^* \psi(x) = \frac{1}{a} [\psi(x) - \psi(x - \hat{\mu})], \quad (2.23)$$

The free Dirac propagator in momentum space then reads

$$D(p)^{-1} = \left[\frac{i}{a} \sum_\mu \gamma_\mu \sin(p_\mu a) + m \right]^{-1} \quad (2.24)$$

$$= \frac{m - \frac{i}{a} \sum_\mu \gamma_\mu \sin(p_\mu a)}{m^2 + a^{-2} \sum_\mu \sin^2(p_\mu a)}, \quad (2.25)$$

where the quantized momenta $p_\mu \in [-\pi/a, \pi/a]$ are restricted to the first Brillouin zone of the lattice. It is particularly interesting to look at the case when the fermion becomes massless ($m = 0$). In this case the propagator in momentum space has the correct continuum limit for fixed momenta

$$D(p)^{-1} = \frac{-\frac{i}{a} \sum_\mu \gamma_\mu \sin(p_\mu a)}{a^{-2} \sum_\mu \sin^2(p_\mu a)} \xrightarrow{a \rightarrow 0} \frac{-i \sum_\mu \gamma_\mu p_\mu}{p^2}. \quad (2.26)$$

The continuum propagator in momentum space has a single pole at the origin, which corresponds to the fermion described by the continuum Dirac equation. On the other hand, the lattice propagator from eq. 2.26 has 15 additional unphys-

2 Quantum Chromodynamics on the Lattice

ical poles:

$$p = (\pi/a, 0, 0, 0), (0, \pi/a, 0, 0), (0, 0, \pi/a, 0), \dots, (\pi/a, \pi/a, \pi/a, \pi/a). \quad (2.27)$$

which are also known as *fermion doublers*. They represent contributions that are pure lattice artifacts and have no continuum analog. Even though the above argument holds for the free theory, due to the fact that the interacting theory is considered to be asymptotically free, we also expect the appearance of doublers in full QCD. The doubling was better understood after the formation of the *Nielsen Ninomiya no-go theorem* [37–39]. The theorem assumes some general properties of the lattice fermion action, such as unitarity, locality of action, symmetry under the cubic group and chiral symmetry in the continuum and then claim that the spectrum of free fermions is never going to be free of doublers. The reason why e.g. chiral symmetry is violated at the quantum level is the emergence of anomalies and this violation is related to topological properties of QCD. Namely, the Nielsen Ninomiya theorem implies that with the presence of fermion doublers there are as many states of positive chirality as of those with negative chirality, which render the theory anomaly-free and which is not in agreement with phenomenology.

One way to avoid the fermion doublers is to break the corresponding symmetry. Wilson's proposal does exactly that: an irrelevant (Wilson-) term is added to the naive fermion action (eq. 2.21), defining the Wilson-Dirac operator in position space

$$D_W = \frac{1}{2} \sum_{\mu} \{ \gamma_{\mu} (\nabla_{\mu}^* + \nabla_{\mu}) - ra \nabla_{\mu}^* \nabla_{\mu} \}. \quad (2.28)$$

The Wilson term is proportional to a , therefore it vanishes in the continuum limit. On the other hand, due to the additional term, the mass contribution to the doublers is proportional to the cutoff ($2r/a$). This can again be deducted from the free propagator in momentum space

$$D(p)^{-1} = [m + \frac{i}{a} \gamma_{\mu} \sin(ap_{\mu}) + r \frac{2}{a} \sin^2(\frac{a}{2} p_{\mu})]^{-1}. \quad (2.29)$$

We see that the Wilson term does not change the low energy spectrum of the theory - it disappears for components with p close to zero. The choice of the *Wilson parameter* $r = 1$ is most often used, which removes all the doublers at the same time. After these considerations, we give the Wilson fermion action for N_f

2.4 Wilson discretization of the fermion action

flavors, corresponding to the definition of the Dirac operator in equation 2.28

$$S_F = a^4 \sum_{f=1}^{N_f} \sum_x \bar{\psi}^{(f)}(x) (D_W + m^{(f)}) \psi^{(f)}(x). \quad (2.30)$$

A direct consequence of the explicit chiral symmetry breaking due to the Wilson term is the increase of discretization errors to $O(a)$. Nevertheless, the convergence rate to the continuum limit of $O(a^2)$ can be restored in a systematic way. This systematic improvement of the convergence will be discussed in section 2.5. Finally, let us just note that, as predicted in the Nielsen-Ninomiya theorem, the Wilson term has a trivial Dirac structure.

2.5 $O(a)$ improved action

In the previous two sections, we have introduced Wilson's original formulation of lattice QCD. The leading lattice corrections of the Wilson gauge action are of the order $O(a^2)$, while the lattice artifacts contribute to the Wilson fermion action already at the order of $O(a)$. These discretization errors vanish in the continuum limit $a \rightarrow 0$. However, performing lattice calculations towards the continuum limit is a non-trivial task and a higher rate of convergence to the continuum limit is advantageous.

Following the Symanzik improvement program [40, 41] it is possible to increase, order by order, the action's rate of convergence to the continuum limit and in a similar manner, the operators of interest. This is achieved by adding irrelevant operators, i.e. operators of a dimension larger than four, to the lattice Lagrangian. With properly chosen coefficients, the additional terms serve as counterterms to the leading order cutoff dependence and therefore speed up the convergence to the continuum limit. These coefficients are easily determined at the tree level of perturbation theory, but their determination on the higher loop level is more demanding. Symanzik argued that, when the lattice spacing is small enough, the lattice regularized theory is equivalent to a continuum theory with an effective action in powers of the lattice spacing a

$$S_{eff} = S_0 + aS_1 + a^2S_2 + \dots, \quad S_k = \int d^4x \mathcal{L}_k(x), \quad (2.31)$$

where the terms \mathcal{L}_k are linear combinations of local gauge-invariant composite fields. Additionally, these terms respect the exact symmetries of lattice theory and have canonical dimension¹ $4 + k$. For the $O(a)$ improvement of the lattice QCD action with Wilson fermions a possible basis of dimension-5 operators of fields for the Lagrangian \mathcal{L}_1 contains

$$\mathcal{O}_1 = \bar{\psi} \sigma_{\mu\nu} F_{\mu\nu} \psi, \quad (2.32)$$

$$\mathcal{O}_2 = \bar{\psi} D_\mu D_\mu \psi + \bar{\psi} D_\mu^* D_\mu^* \psi, \quad (2.33)$$

$$\mathcal{O}_3 = m \text{Tr} F_{\mu\nu} F_{\mu\nu}, \quad (2.34)$$

$$\mathcal{O}_4 = m \{ \bar{\psi} \gamma_\mu D_\mu \psi - \bar{\psi} D_\mu^* \gamma_\mu \psi \}, \quad (2.35)$$

$$\mathcal{O}_5 = m^2 \bar{\psi} \psi, \quad (2.36)$$

where $\sigma_{\mu\nu} = i[\gamma_\mu, \gamma_\nu]/2$. For the on-shell $O(a)$ improvement of the considered action, we can employ the field equations to reduce the number of basis fields in the effective Lagrangian. The cancellation of the effects of action S_1 in the

¹In the convention used here the explicit powers of the quark mass m are included in the dimension counting.

2.5 $O(a)$ improved action

effective theory in the on-shell amplitudes can be achieved by adding lattice representatives of the terms \mathcal{O}_1 , \mathcal{O}_3 and \mathcal{O}_5 to the unimproved lattice Lagrangian. The argumentation for the elimination of operators \mathcal{O}_2 and \mathcal{O}_4 is that, by using the field equations, one can express these operators as functions of \mathcal{O}_1 , \mathcal{O}_3 and \mathcal{O}_5 . The coefficients of the remaining three operators are the functions of the bare coupling g_0 only. We leave the discussion of suitable improvement conditions for chapters 5 and 6. However, note here that fields \mathcal{O}_3 and \mathcal{O}_5 already appear in the unimproved theory and thus merely lead to a reparametrization of bare parameters g_0 and m_0 . The relevance of these terms in connection with massless renormalization schemes is discussed in Ref. [42]. Finally, it turns out that a single independent dimension-5 operator \mathcal{O}_1 is sufficient to obtain the $O(a)$ improvement term for the Wilson fermion action,

$$S_{\text{SW}}[U, \psi, \bar{\psi}] = a^5 c_{\text{SW}}(g_0) \sum_x \sum_{\mu\nu} \bar{\psi}(x) \frac{i}{4} \sigma_{\mu\nu} \hat{F}_{\mu\nu} \psi(x). \quad (2.37)$$

Here $\hat{F}_{\mu\nu}$ represents the lattice version of the field strength tensor introduced by Sheikholeslami and Wohlert

$$\hat{F}_{\mu\nu}(x) = \frac{1}{8a^2} \{Q_{\mu\nu}(x) - Q_{\nu\mu}(x)\}, \quad (2.38)$$

$$Q_{\mu\nu}(x) = U_\mu(x) U_\nu(x + \hat{\mu}) U_\mu^{-1}(x + \hat{\nu}) U_\nu^{-1}(x) \quad (2.39)$$

$$+ U_\nu(x) U_\mu^{-1}(x - \hat{\mu} + \hat{\nu}) U_\nu^{-1}(x - \hat{\mu}) U_\mu(x - \hat{\mu}) \quad (2.40)$$

$$+ U_\mu^{-1}(x - \hat{\mu}) U_\nu^{-1}(x - \hat{\mu} - \hat{\nu}) U_\mu(x - \mu - \hat{\nu}) U_\nu(x - \hat{\nu}) \quad (2.41)$$

$$+ U_\nu^{-1}(x - \hat{\nu}) U_\mu(x - \hat{\nu}) U_\nu(x + \mu - \hat{\nu}) U_\mu^{-1}(x) \quad (2.42)$$

and c_{SW} is the coefficient that has to be tuned such that the $O(a)$ improvement is achieved. The lattice object $Q_{\mu\nu}$ which enters the Sheikholeslami-Wohlert term is depicted in the upper right corner of Figure 2.1. In order to perform all steps of $O(a)$ improvement non-perturbatively, one should determine c_{SW} in lattice simulations. The existing determinations of c_{SW} for different numbers of fermion flavors[21, 43–45] are given in Table 2.1. In all of these determinations, the Wilson plaquette action was used in the gauge sector.

The Symanzik improvement program is rarely applied to fermion actions with lattice artifacts beyond $O(a)$. Namely, the next step in the improvement would require including dimension-6 operators in the leading correction term of the effective action and the four fermion operators would appear among them. This causes technical difficulties, since the standard procedure for simulating dynamical fermions, which will be discussed in section 3.7, can only be applied to an action with fermion field bilinears. In order to simulate an action with four fermion operators, one has to introduce auxiliary fields [46].

2 Quantum Chromodynamics on the Lattice

$$c_{SW}^{N_f=0} = \frac{1-0.656g_0^2-0.152g_0^4-0.054g_0^6}{1-0.922g_0^2} \quad 0 \leq g_0^2 \leq 1 \quad [43]$$

$$c_{SW}^{N_f=2} = \frac{1-0.45g_0^2-0.175g_0^4+0.012g_0^6+0.045g_0^8}{1-0.720g_0^2} \quad 0 \leq g_0^2 \leq 6/5.4 \quad [44]$$

$$c_{SW}^{N_f=3} = \frac{1-0.19478g_0^2-0.110781g_0^4-0.230239g_0^6+0.137401g_0^8}{1-0.460685g_0^2} \quad 0 \leq g_0^2 \leq 6/5.2 \quad [45]$$

$$c_{SW}^{N_f=4} = \frac{1-0.1372g_0^2-0.1641g_0^4+0.1679g_0^6}{1-0.4031g_0^2} \quad 0 \leq g_0^2 \leq 6/5.0 \quad [21]$$

Table 2.1: Non-perturbative determinations of the Sheikholeslami-Wohlert coefficient c_{SW} for different number of dynamical quark flavors N_f . All of the given estimations were obtained using the Wilson plaquette action in the gauge sector.

Here we have outlined the procedure for obtaining the action of choice for the work that will be presented in the following chapters. However, to fully retain an $O(a^2)$ convergence to the continuum limit, the improvement of the action has to be followed by the improvement of the operators. We leave the discussion of additional work that still needs to be done in this respect for chapter 5.

2.6 Renormalization

We have previously chosen the ultraviolet regulator of the theory to be the lattice spacing a and now wish to obtain the physical observables from the quantities computed on the lattice. Before being able to achieve that, one first has to renormalize the theory. For further discussion, we choose to use a mass-independent renormalization scheme. Also, we initially suppose that the bare parameters of the Lagrangian m and g get multiplicatively renormalized by

$$\bar{g}^2 = g^2 Z_g(g^2, a\mu), \quad (2.43)$$

$$\bar{m} = m Z_m(g^2, a\mu), \quad (2.44)$$

where the renormalization factors do not depend on the quark mass.

Let us now consider a physical (renormalized) quantity $\bar{\mathcal{Q}}$. Its measurement should not depend on the renormalization scale μ , but only on the renormalized parameters of the theory, \bar{g} and \bar{m} . Therefore, the result has to be renormalization scale invariant, or in short

$$\frac{d}{d\mu} \bar{\mathcal{Q}}(\bar{g}(\mu), \bar{m}(\mu), \mu) \equiv 0. \quad (2.45)$$

2.6 Renormalization

This differential equation gives us the *Renormalization Group Equation* (RGE)

$$\left\{ \mu \frac{\partial}{\partial \mu} + \beta(\bar{g}) \frac{\partial}{\partial \bar{g}} + \tau(\bar{g}) \bar{m} \frac{\partial}{\partial \bar{m}} + \gamma_Q(\bar{g}) \right\} \bar{Q}(\bar{g}(\mu), \bar{m}(\mu), \mu) \equiv 0. \quad (2.46)$$

The β -function is, up to normalization, the anomalous dimension of the coupling constant, while the behavior of m and Q under a rescaling is contained in the τ and γ_Q functions respectively.

From eq. 2.46, we can deduce the formal definition of the β - and τ -function which will be relevant for the following discussion

$$\beta(\bar{g}) = \mu \frac{\partial \bar{g}}{\partial \mu}, \quad (2.47)$$

$$\tau(\bar{g}) = \frac{\mu}{\bar{m}} \frac{\partial \bar{m}}{\partial \mu}. \quad (2.48)$$

Finally, γ_Q is the anomalous dimension of Q

$$\gamma_Q(\bar{g}) = -\frac{\mu}{Z_Q} \frac{\partial Z_Q}{\partial \mu}, \quad (2.49)$$

with Z being the corresponding renormalization constant ($\bar{Q} = Z_Q Q$), which connects the renormalized observable \bar{Q} and the bare observable Q .

The definition of the functions β , τ and γ_Q does not depend on perturbation theory. On the other hand, if one wants to solve the RGE, a choice of a specific renormalization scheme is needed and the anomalous dimensions then become dependent on that scheme. In QCD, the β -function describes the scale dependence of the strong coupling constant, α_s in a given scheme (cf. chapter 1). The β -function has the asymptotic expansion

$$\beta(\bar{g}) \stackrel{\bar{g} \rightarrow 0}{=} -\bar{g}^3 (b_0 + b_1 \bar{g}^2 + b_2 \bar{g}^4 + \dots). \quad (2.50)$$

The β -function is usually quoted in a minimal subtraction ($\overline{\text{MS}}$) renormalization scheme. The coefficients of the expansion in eq. 2.50 have been computed in the $\overline{\text{MS}}$ scheme up to four loops so far [47], where the first two coefficients are unique for all mass independent renormalization schemes

$$b_0 = \frac{11 - \frac{2}{3}N_f}{(4\pi)^2}, \quad b_1 = \frac{102 - \frac{38}{3}N_f}{(4\pi)^4}. \quad (2.51)$$

2 Quantum Chromodynamics on the Lattice

The value of the succeeding coefficient in $\overline{\text{MS}}$ scheme reads [48]

$$b_2^{\overline{\text{MS}}} = \frac{(\frac{2857}{2} - \frac{5033}{18}N_f + \frac{325}{54}N_f^2)}{(4\pi)^6} \quad (2.52)$$

Another renormalization scheme relevant for this work, which will be defined in chapter 5 is the Schrödinger functional renormalization scheme. The two loop coefficient in this scheme is computed in Ref. [49]

$$b_2^{\text{SF}} = \frac{0.483(7) - 0.275(5)N_f + 0.0361(5)N_f^2 - 0.00175(1)N_f^3}{(4\pi)^3}. \quad (2.53)$$

The coefficients from equations 2.51, 2.52 are computed in the given references for an arbitrary number of colors, but the results we have quoted above are, for simplicity, given for the theory with three color degrees of freedom. Eq. 2.53 is computed for the case $N_c = 3$ only. The Λ parameter of QCD, previously introduced in chapter 1, is actually the integration constant required for solving the first order differential equation 2.47. It is *renormalization group invariant* (RGI) quantity, i.e. it does not depend on the renormalization scale μ

$$\Lambda = \mu(b_0\bar{g}^2(\mu))^{-\frac{b_1}{2b_0^2}} e^{-\frac{1}{2b_0\bar{g}^2(\mu)}} e^{-\int_0^{\bar{g}(\mu)} \{\frac{1}{\beta(x)} + \frac{1}{b_0x^3} - \frac{b_1}{b_0^2x}\} dx}. \quad (2.54)$$

On the other hand, Λ is renormalization scheme dependent and the exact relation between the two mass independent schemes is obtained through a 1-loop computation. We give here as an example the relation between the Lambda parameters in the Schrödinger functional scheme with $N_f = 2$ and the $\overline{\text{MS}}$ scheme, which will be used later in this work

$$\Lambda_{\overline{\text{MS}}}^{(2)} = 2.382035(3)\Lambda_{\text{SF}}^{(2)}. \quad (2.55)$$

Similarly to the case of the β -function, by formally integrating eq. 2.48 we obtain, for small couplings, the asymptotic expansion of the τ -function

$$\tau(\bar{g}) \stackrel{\bar{g} \rightarrow 0}{=} -\bar{g}^2(d_0 + d_1\bar{g}^2 + d_2\bar{g}^4 + \dots). \quad (2.56)$$

For this expansion, only the 1-loop coefficient is universal

$$d_0 = \frac{8}{(4\pi)^2}. \quad (2.57)$$

The corresponding integration constant for solving eq. 2.48 is the so-called RGI

invariant quark mass, given by

$$M = \bar{m}(\mu) (2b_0 \bar{g}^2(\mu))^{-\frac{d_0}{2b_0}} e^{-\int_0^{\bar{g}(\mu)} \left\{ \frac{\tau(g)}{\beta(g)} - \frac{d_0}{b_0 g} \right\}}. \quad (2.58)$$

The above RGI invariant mass is both scale and renormalization scheme independent. This quantity exists for each quark flavor separately and in the following considerations we will take the Λ parameter and the RGI quark masses M_1, \dots, M_{N_f} as fundamental parameters of QCD.

2.6.1 Renormalization of Wilson fermions

We now proceed to consider the renormalization of the unimproved Wilson theory, introduced in section 2.4. The chiral symmetry breaking of Wilson fermions requires an additional additive mass renormalization. Therefore, for Wilson fermions eq. 2.44 gets replaced with

$$\bar{m} = m_q Z_m(g^2, a\mu), \quad m_q = m - m_{\text{cr}}, \quad (2.59)$$

where m_{cr} represents the (bare) *critical quark mass* and takes the value of the lattice cutoff a^{-1} multiplied by a function of the bare coupling g . The so-called *bare subtracted quark mass* m_q defines the deviation from the *critical line*, i. e. the line where the renormalized quark mass vanishes

$$m_q = 0, \quad \text{or equivalently} \quad m_{\text{cr}} = m. \quad (2.60)$$

After the condition 2.60 has been fulfilled, the only remaining parameters are the couplings. Therefore, the critical line is parametrized by the bare coupling g . The estimation of $m_{\text{cr}}(g)$ will be further addressed in chapter 5. It has to be performed with the help of lattice simulations, although starting guidelines may be obtained from perturbation theory.

2.7 Continuum limit

Finally, we give some practical remarks about the extrapolation to the continuum limit, $a \rightarrow 0$. As already mentioned, performing the continuum limit in lattice QCD is a very important but, at the same time, very difficult topic. In order to obtain the continuum result for the quantity of interest, one has to compute this quantity several times at different values of the lattice spacing, and then extrapolate to $a = 0$ following the line of constant physics. Performing lattice QCD simulations at small lattice spacings is limited by the increasing computational costs. The reason for this is the slowing down of all currently known simulation

2 *Quantum Chromodynamics on the Lattice*

programs for lattice QCD with periodic boundary conditions at the rate of a^{-5} or even a larger power of a^{-1} (see Ref. [50]). The usual range of lattice spacings for modern lattice simulations is $0.05\text{fm} \leq a \leq 0.1\text{fm}$. Due to the aforementioned critical slowing down, simulating at smaller lattice spacings is not possible with the currently known algorithms for QCD. Given the above constraint on the range of lattice spacings that can be simulated, if one wants to ensure that the correct continuum limit is reached, a thorough theoretical understanding of the way that the continuum limit is approached is needed. We will extend this discussion further in chapter 7.

3 Lattice QCD Simulations

In the first decade of lattice QCD, the simulations were fairly limited by the necessity to neglect the quark contributions, which represent a significant computational challenge. Lattice QCD simulations with this approximation are usually denoted as *quenched computations*. Although already very successful in the early eighties at predicting the correct order of magnitude of some very important QCD quantities, precision calculations with this approximation were not within reach. Only after the introduction of the *Hybrid Monte Carlo algorithm* [51] could the fermionic degrees of freedom be simulated on the lattice and up to the present no alternative algorithm for successful fermion simulations has proven better in practice. We will introduce in this chapter some basic techniques of numerical simulations with the final goal of discussing the Hybrid Monte Carlo algorithm (HMC). Afterwards, we discuss a number of optimizations for the HMC algorithm that were crucial for making lattice QCD a precision tool and made it possible to obtain a number of original predictions of QCD observables from the lattice simulations, including the final results of this thesis.

3.1 Importance sampling

Importance sampling is a general technique for variance reduction in Monte Carlo simulations and we will illustrate it here on a simple example of the lattice quantum field theory with only bosonic fields. A partition function of this theory in the functional integral formalism has the form

$$Z = \int [d\phi] e^{-S(\phi)}, \quad [d\phi] = \prod_x d\phi(x), \quad (3.1)$$

where $S(\phi)$ is the action and $\phi(x)$ a bosonic field on lattice site x . $[d\phi]$ denotes the integration over the values of the field on all lattice sites x . The expectation value of the observable \mathcal{A} is then computed as an average with respect to the Boltzmann weight factor $e^{-S(\phi)}$

$$\mathcal{A} = \frac{1}{Z} \int [d\phi] \mathcal{A}(\phi) e^{-S(\phi)}. \quad (3.2)$$

3 Lattice QCD Simulations

The vast computation of multidimensional integrals needed for quantum field theory simulations on the lattice is numerically very demanding and it is performed using a variety of importance sampling methods. These are designed to select a sufficiently complete subset of points $\{\phi^{(k)}, k = 1 \dots N_{\text{cf}}\}$ in the integration domain, such that the ratio of integrals is well-estimated on the subset. The value of the field on all sample points of this subset will in the following be denoted as *field configuration*.

3.2 The Monte Carlo method and the Metropolis algorithm

The goal of Monte Carlo importance sampling is to approximate the integral 3.2 by sampling a relatively small number of random field configurations N_{cf} with an appropriate weight factor. Namely, the Monte Carlo method generates a sequence of N_{cf} configurations $\phi^{(k)}$, such that the probability distribution reads

$$P(\phi) \propto e^{-S(\phi)} \quad (3.3)$$

and that this distribution is positive. The v. e. v. of an observable is then given by the average over the sample configurations

$$\langle A \rangle = \frac{1}{N_{\text{cf}}} \sum_{k=1}^{N_{\text{cf}}} A(\phi^{(k)}) \quad (3.4)$$

in the limit $N_{\text{cf}} \rightarrow \infty$. The Monte Carlo method starts from an initial configuration and perform a sequence of random updates in the field values such that the desired probability distribution is approached. These random updates are prescribed in such a way that the sequence of probability distributions $\phi^{(0)}, \phi^{(1)}, \dots$ becomes a *Markov chain*. Similarly to statistical mechanics, the probability distribution to which this chain converges is called the *equilibrium distribution* and the process of reaching it is called *thermalization*. The expectation value of the observable is then evaluated after the distribution is suitably thermalized.

Let us denote the probability for a random transition $\phi \rightarrow \phi'$ as $R(\phi' \leftarrow \phi)$. The Markov chain denotes the sequence of probability distributions $P^{(k)}(\phi)$, such that the probability distribution $P^{(k+1)}(\phi')$ depends only on $P^{(k)}(\phi)$

$$P^{(k+1)}(\phi') = \int [d\phi] P^{(k)}(\phi) R(\phi' \leftarrow \phi). \quad (3.5)$$

The probabilities of ϕ' being initial or final configuration in a random update have

3.2 The Monte Carlo method and the Metropolis algorithm

to be equal, namely

$$\sum_{\phi} R(\phi' \leftarrow \phi) P(\phi) = \sum_{\phi} R(\phi \leftarrow \phi') P(\phi') \quad (3.6)$$

The sum on the right-hand side is trivial and can be calculated explicitly by using the normalization property of R

$$0 \leq R(\phi \leftarrow \phi') \leq 1, \quad \sum_{\phi} R(\phi \leftarrow \phi') = 1. \quad (3.7)$$

Therefore, the equilibrium distribution $P(\phi')$ is a fixed point of the Markov process

$$\sum_{\phi} R(\phi' \leftarrow \phi) P(\phi) = P(\phi'). \quad (3.8)$$

$$(3.9)$$

The solution of the balance equation 3.6 can be obtained if the so called *detailed balance* condition is fulfilled

$$R(\phi' \leftarrow \phi) P(\phi) = R(\phi \leftarrow \phi') P(\phi'). \quad (3.10)$$

It is also important to note that for the correctness of the results obtained, it is required for the Markov chain to be able to access all possible field configurations. This property is called *ergodicity*. A sufficient condition for it to be fulfilled is that the transition matrix $R(\phi' \rightarrow \phi)$ is strictly positive, for all pairs of ϕ and ϕ' . In realistic simulations, Monte Carlo updating algorithms often have problems connecting configurations with different topological sectors. In general, it is not trivial to show for a certain update method that starting from any point in a scheme leads to the unique, equilibrium distribution in the end. The transition methods used in this work are tailored such that they are sufficiently robust and that, for our choices of simulation parameters, the aimed distribution is always achieved.

3.2.1 Metropolis algorithm

The Metropolis method is the simplest algorithm that satisfies the condition 3.10. It makes a symmetrical proposal of an update $\phi \rightarrow \phi'$ with the probability $T_P(\phi' \leftarrow \phi)$ such that the reverse transition has the same probability

$$T_P(\phi' \leftarrow \phi) = T_P(\phi \leftarrow \phi'). \quad (3.11)$$

3 Lattice QCD Simulations

Next, a random number r is chosen from an uniform distribution on the real interval $[0, 1]$ and a proposal ϕ' is accepted if

$$P(\phi') \geq rP(\phi). \quad (3.12)$$

Taking 3.3 into account, the condition 3.12 can be rewritten as

$$\frac{e^{-S(\phi')}}{e^{-S(\phi)}} \geq r. \quad (3.13)$$

In other words, the effect of the Metropolis condition 3.11 is that

1. If $S(\phi') < S(\phi)$, the update is always accepted.
2. Otherwise, the change is accepted if $e^{-\Delta S} > r$

The condition for accepting the proposed field configuration ϕ' is referred to as the *accept/reject* condition. If 3.13 is not satisfied and the update is rejected, the old configuration is taken for the Markov chain and then a new attempt is made. The challenge in constructing an efficient algorithm for fast simulations is to find an a priori transition probability $T_P(\phi' \leftarrow \phi)$, such that the proposed states are accepted with high probability and, at the same time, the moves in the phase space are large.

In order to apply them in lattice QCD simulations, the above methods are generalised for gauge fields $U \in \text{SU}(3)$. The expectation value of the QCD observable \mathcal{O} in a pure gauge theory is computed as

$$\langle \mathcal{O} \rangle = \frac{\int D[U] \mathcal{O}(U) e^{-S_G[U]}}{\int D[U] e^{-S_G[U]}}, \quad D[U] = \prod_{x,\mu} dU \quad (3.14)$$

where dU is the integration measure for the link variables $U_\mu(x)$, which is invariant under $\text{SU}(3)$. We apply the described Monte Carlo method for generating a set of gauge configurations $U^{(k)}$, with probability $D[U]e^{-S_G[U]}$. Then the observable \mathcal{O} can be estimated as an average over N_{cf} gauge configurations

$$\langle \mathcal{O} \rangle = \frac{1}{N_{\text{cf}}} \sum_{k=1}^{N_{\text{cf}}} \mathcal{O}(U^{(k)}) + O\left(\frac{1}{\sqrt{N_{\text{cf}}}}\right). \quad (3.15)$$

The second term refers to the statistical error, and its estimation is addressed in Appendix 8. The probability to accept the gauge configuration U' as the update of configuration U , which satisfies the detailed balance condition 3.10 is given by

$$T_A(U' \leftarrow U) = \min(1, e^{-\Delta S}), \quad \Delta S = S[U'] - S[U]. \quad (3.16)$$

For the alternative Monte Carlo schemes that can be used for simulating pure gauge theory, such as the Heath Bath algorithm and Overrelaxation, we point the reader to the literature [29, 30].

3.3 Molecular Dynamics method

In 1982, Callaway and Rahman introduced a method that gives the desired statistical distribution by integrating classical equations of motion, known as the *Molecular dynamics* (MD) method [52, 53]. In order to apply this method to a theory with link variables in $SU(3)$, one needs to add to the theory with gauge fields in $SU(3)$ the set of their canonical momenta variables, which take values in $su(3)$ algebra (cf. Appendix 2)

$$\pi_\mu(x) = \sum_a \pi_\mu^a(x) T^a, \quad \pi_\mu^a(x) \in \mathbb{R}. \quad (3.17)$$

The associated Hamiltonian of the extended theory is now given with

$$\mathcal{H}(\pi, U) = \frac{1}{2}(\pi, \pi) + S(U), \quad (3.18)$$

where (π, π) represents the scalar product on $su(3)$ defined in Appendix 1. This Hamiltonian defines classical evolution in fictitious *molecular dynamics time* (from now on denoted by t_{MD}) and its equations of motion¹ are given by

$$\dot{\pi}_\mu(x) = -\frac{\partial \mathcal{H}(\pi, U)}{\partial U_\mu(x)} = F_\mu(x) \quad (3.19)$$

$$\dot{U}_\mu(x) = \frac{\partial \mathcal{H}(\pi, U)}{\partial \pi_\mu(x)} = \pi_\mu(x) U_\mu(x). \quad (3.20)$$

The dot in the above equations denotes the derivative with respect to molecular dynamics time t_{MD} , therefore the above equations are often referred to as *molecular dynamics equations*. Equation 3.19 defines the *molecular dynamics force* $F_\mu(x)$. Let us stress once more that the MD time t_{MD} is completely unrelated to the time coordinate of space-time. The solutions of the MD equations can be visualized as trajectories through phase space parametrized by MD time $[\pi^{t_{\text{MD}}}, U^{t_{\text{MD}}}]$ and they are uniquely defined by an initial choice of fields at MD time $t_{\text{MD}} = 0$. It can be easily shown that the introduction of the momenta fields does not change the

¹As noted in [34], the derivatives with respect to the gauge links $U_\mu(x)$ are formally defined by substituting $U_\mu(x) \rightarrow e^{w_\mu^a(x) T^a} U_\mu(x)$, differentiating with respect to the real variables $w_\mu^a(x)$ and setting $w_\mu^a(x) = 0$ at the end.

3 Lattice QCD Simulations

physics content of the theory

$$e^{-S(U)} = \text{const.} \times \int D[\pi] e^{-\mathcal{H}(\pi, U)}. \quad (3.21)$$

Therefore, the observable \mathcal{O} (eq. 3.15) can be evaluated using the additional molecular dynamics fields

$$\langle \mathcal{O} \rangle = \frac{\int D[\pi] D[U] \mathcal{O}(U) e^{-\mathcal{H}(\pi, U)}}{\int D[\pi] D[U] e^{-\mathcal{H}(\pi, U)}}. \quad (3.22)$$

3.4 Hybrid Monte Carlo Algorithm

For a fixed molecular dynamics trajectory length τ the Hamiltonian from eq. 3.18 does not remain a constant of motion, since the equations of motion can only be approximately (numerically) integrated

$$\Delta \mathcal{H} = \mathcal{H}(\pi^\tau, U^\tau) - \mathcal{H}(\pi, U) \neq 0. \quad (3.23)$$

This inaccuracy can be fixed by applying the Metropolis accept/reject step at the end of each MD trajectory. The method that combines the MD integration with the Metropolis method in this way is known as the Hybrid Monte Carlo algorithm (HMC). The motivation for constructing HMC was to find an algorithm that would update the fields globally and allow large steps through the configuration space without introducing additional systematic errors. Although formulated in the eighties [51], HMC is still the only known algorithm suitable for simulating dynamical fermions.

The basic idea is to view the molecular dynamics trajectory from the starting gauge field $U^{(0)}$ to the field at the end of the MD trajectory $U^{(\tau)}$ as a transition function for the Metropolis algorithm $T((U', \pi') \leftarrow (U, \pi))$. The HMC algorithm is summarized in following steps:

1. Momentum fields π are randomly generated, with probability distribution $e^{\frac{1}{2}(\pi, \pi)}$
2. The MD equations of motion are numerically integrated from time $t_{\text{MD}} = 0$ with initial values of the fields $[\pi, U]$ to some later time $t_{\text{MD}} = \tau$ where the fields take values $[\pi^\tau, U^\tau]$.
3. The new gauge field U' is set to the field U^τ with the acceptance probability

$$P_{\text{acc}}(\pi, U) = \min\{1, e^{-(\mathcal{H}(\pi^\tau, U^\tau) - \mathcal{H}(\pi, U))}\} \quad (3.24)$$

3.5 Integration of MD equations of motion

If the proposed change is rejected, the new gauge field U' is set to the field value at the beginning of trajectory U (Metropolis accept/reject step) and a new trajectory, starting with momenta refreshment, is followed.

3.5 Integration of MD equations of motion

In order to complete the discussion of the HMC algorithm, it is needed to define the method for the numerical integration of the equations of motion 3.19 and 3.20. The first request for the MD integration is that it should be *time-reversible*. This would mean that for any chosen trajectory length τ and for any update $U \rightarrow U'$, starting from the final configuration U' and running the trajectory backwards with the momenta flipped in sign gives to a required precision an initial gauge configuration U . Another important request for the update algorithm is that the functional integral measure $D[\pi]D[U]$ be preserved - a feature known as *area-preservation*. Any approximate integration that fulfills these two properties may be employed in the MD part of the HMC algorithm.

3.5.1 Leap-frog integrator

The simplest integration scheme that is reversible and satisfies the area-preservation is the *leap-frog algorithm*. The integration begins by dividing the trajectory of a length τ in N steps of size $\epsilon = \tau/N$. The discretization naturally gives the integration error, which disappears in the limit $\epsilon \rightarrow 0$. As we already mentioned, the error for finite ϵ is compensated in HMC by the inclusion of the Metropolis accept/reject step at the end of the MD trajectory.

The Taylor expansion of the equations of motion gives

$$\pi^{t_{MD}+\epsilon} = \pi^{t_{MD}} - \epsilon F|_{U=U^{t_{MD}}} + \mathcal{O}(\epsilon^2) \quad (3.25)$$

$$U^{t_{MD}+\epsilon} = U^{t_{MD}} + \epsilon \pi^{t_{MD}} U^{t_{MD}} + \mathcal{O}(\epsilon^2). \quad (3.26)$$

Based on the first terms of the expansion, we construct operations for the integration scheme that give an elementary update of the MD momenta (\mathcal{I}_π) and gauge fields (\mathcal{I}_U)

$$\mathcal{I}_\pi(\epsilon) : (U, \pi) \rightarrow (U, \pi - \epsilon F) \quad (3.27)$$

$$\mathcal{I}_U(\epsilon) : (U, \pi) \rightarrow (e^{\epsilon \pi} U, \pi), \quad (3.28)$$

The application of the leap-frog integrator to the trajectory $[0, \tau]$ is then defined

3 Lattice QCD Simulations

as

$$\mathcal{J}_{LF}(\epsilon, N) = \{\mathcal{I}_\pi(\epsilon/2)\mathcal{I}_U(\epsilon)\mathcal{I}_\pi(\epsilon/2)\}^N, \quad \epsilon = \frac{\tau}{N}. \quad (3.29)$$

It is constructed from N updates of the form $\mathcal{I}_\pi(\epsilon/2)\mathcal{I}_U(\epsilon)\mathcal{I}_\pi(\epsilon/2)$, each of them contributing to the integration error by ϵ^3 giving the total integration error $O(\epsilon^2)$. This integrator is widely used for its simplicity and it is easy to show that it is reversible and area-preserving. Nevertheless, there are many other integrators that preserve the previously mentioned good properties. In particular, the variants of the so-called *symmetric symplectic integrators* are manifestly area-preserving and reversible. It might be somewhat more complicated to implement some of them in practice, but the gain in the simulations is either equal to or larger than what the simple discretization error calculation would predict. An example of a simple symmetric symplectic integrator widely used in this work will be discussed in the following.

3.5.2 Omelyan-Mryglod-Folk integrator

Omelyan-Mryglod and Folk have suggested several symplectic numerical integration schemes in their work given in Ref. [54]. Through this work, we mainly use the 2nd order Omelyan-Mryglod-Folk (OMF) integrator. It amounts to applying the elementary combination of operations

$$\mathcal{J}_{OMF2}(\epsilon, N, \lambda) = \{\mathcal{I}_\pi(\lambda\epsilon)\mathcal{I}_U(\frac{\epsilon}{2})\mathcal{I}_\pi((1-2\lambda)\epsilon)\mathcal{I}_U(\frac{\epsilon}{2})\mathcal{I}_\pi(\lambda\epsilon)\}^N, \quad \epsilon = \frac{\tau}{2N} \quad (3.30)$$

The integrator updates the fields two times in each step size ϵ and depends on the parameter λ , which is a subject of tuning. As mentioned above, this is the main integration scheme that we used in most of the runs that will be discussed in the following. Recently, the 4th order *OMF* integrator was found to be advantageous in the particular simulation setup [55]. We have also considered it in our integrator tuning procedure. Therefore, we give here for completeness the combination corresponding to the elementary update of gauge fields and momenta of the 4th order *OMF* integrator

$$\begin{aligned} \mathcal{J}_{OMF4}(\epsilon, N) = & \{\mathcal{I}_\pi(\sigma\epsilon) \mathcal{I}_U(\rho\epsilon) \mathcal{I}_\pi(\lambda\epsilon) \mathcal{I}_U(\theta\epsilon) \\ & \mathcal{I}_\pi((1-2(\lambda+\sigma))\frac{\epsilon}{2}) \mathcal{I}_U((1-2(\theta+\rho))\epsilon) \mathcal{I}_\pi((1-2(\lambda+\sigma))\frac{\epsilon}{2}) \\ & \mathcal{I}_U(\theta\epsilon) \mathcal{I}_\pi(\lambda\epsilon) \mathcal{I}_U(\rho\epsilon) \mathcal{I}_\pi(\sigma\epsilon)\}^N, \quad \epsilon = \frac{\tau}{5N}. \end{aligned} \quad (3.31)$$

3.6 HMC for the Wilson gauge theory

The optimal values for the parameters in eq. 3.31 are fixed to

$$\sigma = 0.0839831526287669, \quad (3.32)$$

$$\rho = 0.2539785108410595, \quad (3.33)$$

$$\lambda = 0.6822365335719091, \quad (3.34)$$

$$\theta = -0.0323028676526997. \quad (3.35)$$

The above parameters are obtained numerically in Ref. [54]. Their determination is based on the observation that for each symplectic integrator there is a shadow Hamiltonian² that is exactly conserved[57]. By computing the higher order derivatives of the shadow Hamiltonian (either analytically [56, 58] or numerically [54]) one arrives at the optimal parameters for the higher order integrators such as the previously discussed 4th order OMF integrator. Let us finally note that the OMF_2 integrator for the parameter choice $\lambda = 0.25$ equals the leap-frog integration with a two times smaller elementary integration step size.

3.6 HMC for the Wilson gauge theory

In this section we shall discuss in more detail how to obtain the evolution of the gauge fields in pure gauge theory, while preserving the Hamiltonian

$$\mathcal{H}(\Pi, U) = \frac{1}{2} \sum_{x,\mu} \text{Tr}\{\Pi_\mu^2(x)\} + S_G(U), \quad (3.36)$$

where S_G denotes the Wilson action of the $SU(3)$ gauge group discussed in section 2.3. This section is based on the considerations in Ref. [59] and this is also where the notation comes from. The traceless Hermitian canonical momenta used in the above eq. 3.36 relates to the anti-Hermitian momenta previously considered in 3.18 as $\Pi_\mu = -i\sqrt{2}\pi_\mu$. Let us consider their evolution together with the gauge fields U_μ . In order for the link variables $U_\mu(x)$ to remain an element of $SU(3)$ after the derivation with respect to the molecular dynamics time (cf. eq. 3.20), their equation of motion must have the form

$$\dot{U}_\mu(x) = i\Pi_\mu(x)U_\mu(x) \quad (3.37)$$

²For its construction see e.g. Ref. [56].

3 Lattice QCD Simulations

or equivalently,

$$U'_\mu(x) = e^{i\Pi_\mu(x)\epsilon} U_\mu(x), \quad (3.38)$$

where $U'_\mu(x)$ denotes the (updated) gauge field after the infinitesimal change in molecular dynamics time ϵ when the dynamics is governed by the Hamiltonian 3.18. The equation of motion for \mathcal{H} is obtained if we require it to be a constant of the motion

$$\dot{\mathcal{H}} = \sum_{x,\mu} \text{Tr} \left\{ \dot{\Pi}_\mu(x) \Pi_\mu(x) + \frac{\beta}{6} (\dot{U}_\mu(x) V_\mu(x) + V_\mu^\dagger(x) \dot{U}_\mu^\dagger(x)) \right\} = 0. \quad (3.39)$$

Variables $V_\mu(x)$ represent the sum of the staples that are products of the other three links in the plaquettes containing $U_\mu(x)$

$$\begin{aligned} V_\mu(x) &= \sum_{\nu, \mu \neq \nu} (V_{\mu\nu}^{(u)}(x) + V_{\mu\nu}^{(d)}(x)) \\ V_{\mu\nu}^{(u)}(x) &= U_\nu(x + \hat{\mu}) U_\mu^\dagger(x + \hat{\nu}) U_\nu^\dagger(x) \\ V_{\mu\nu}^{(d)}(x) &= U_\nu^\dagger(x + \hat{\mu} - \hat{\nu}) U_\mu^\dagger(x - \hat{\nu}) U_\nu(x - \hat{\nu}). \end{aligned} \quad (3.40)$$

The objects $V_{\mu\nu}^{(u)}$ and $V_{\mu\nu}^{(d)}$ are depicted in Figure 2.1. Condition 3.37 is used to eliminate $\dot{U}_\mu(x)$ from eq. 3.39 and we find

$$\dot{\mathcal{H}} = 0 = \sum_{x,\mu} \text{Tr} \left\{ \Pi_\mu(x) (\dot{\Pi}_\mu(x) + iF_\mu^G(x)) \right\}. \quad (3.41)$$

Due to the fact that $\Pi_\mu(x)$ is traceless, eq. 3.41 will be satisfied if $\dot{\Pi}_\mu(x) + iF_\mu^G(x)$ is the multiple of the unit matrix. Since the derivative of $\Pi_\mu(x)$ remains traceless, $\text{Tr}\{\dot{\Pi}_\mu(x)\} = 0$ determines the remaining constant. Taking these considerations into account, we finally obtain the equations of motion for the conjugate momenta

$$i\dot{\Pi}_\mu(x) = 2[U_\mu(x) \mathcal{F}_\mu^G(x)]_{\text{T.A.}}. \quad (3.42)$$

The subscript T.A. denotes the traceless anti-Hermitian part of the matrix

$$A_{\text{T.A.}} \equiv \frac{1}{2} \left(A - A^\dagger - \frac{1}{3} \text{Tr}\{A - A^\dagger\} \right). \quad (3.43)$$

The right hand side of eq. 3.42 is the molecular dynamics force (or just *force* in the

3.7 Including dynamical fermions in simulations

following), which has previously been defined in eq. 3.19

$$F_\mu^G(x) \equiv 2[U_\mu(x)\mathcal{F}_\mu^G(x)]_{T.A.}. \quad (3.44)$$

From equation 3.39 we obtain the explicit expression for \mathcal{F}_μ^G in the case of the Wilson gauge action

$$\mathcal{F}_\mu^G(x) = \frac{\beta}{6} \sum_{\nu \neq \mu} (V_{\mu\nu}^{(u)}(x) - V_{\mu\nu}^{(d)}(x)), \quad (3.45)$$

where $V_{\mu\nu}^{(u)}$ and $V_{\mu\nu}^{(d)}$ are defined in eq. 3.40. The *force magnitude* is a real number defined by

$$||F^G||^2 \equiv 2\text{Tr}\{F^G F^{G\dagger}\} \geq 0, \quad (3.46)$$

and it will be recalled quite often in future considerations, also for different fermion forces that we will consider. $||F||^2$ is given by the trace of a sum of closed paths, therefore this expression is gauge invariant. As noted in [59], if we for example consider the gauge force in direction $\mu = 0$, we have

$$||F_0^G(x)||^2 = \left(\frac{2\beta}{3}\right)^2 \sum_{i,j} \text{Tr}\{E_i E_j\}, \quad (3.47)$$

where $E_i(x) \equiv \frac{1}{2} \left(U_0(x)(V_{0i}^{(u)}(x) - V_{0i}^{(d)}(x)) \right)_{T.A.}$ is the discretized electric field in lattice units.

3.7 Including dynamical fermions in simulations

So far we have considered a way to simulate the theory that takes into account only the gauge fields dynamics. This corresponds to neglecting the vacuum loops of quarks that are present in the full theory. The QCD partition function which, in addition to the gauge action $S_G[U]$, also includes fermionic dynamical degrees of freedom is given by the following

$$Z = \int [DU][D\psi][D\bar{\psi}] e^{-S_G(U) - S_F(U,\psi,\bar{\psi})}. \quad (3.48)$$

3 Lattice QCD Simulations

If we consider the case with two degenerate flavors of dynamical quarks, the corresponding fermion action reads

$$S_F(U, \psi, \bar{\psi}) = \sum_{f=1}^2 \bar{\psi}_f D(U) \psi_f, \quad (3.49)$$

where $D(U) = D_0(U) + m$ represents the massive Dirac operator.

The eigenvalues of the lattice Dirac operator $D(U)$ are complex and their real parts are not always positive definite. Therefore, if one would like to simulate just a single fermion flavor with the simple approach described above, the exponential in eq. 3.48 would not necessarily have to be real and positive and in general cannot be interpreted as a conventional probability measure. This is the reason we were from the start considering two degenerate dynamical quark flavors - in this case the Dirac operator enters quadratically in the effective action and the positivity is guaranteed.

Since Grassmann fields $\psi_f, \bar{\psi}_f$ are very difficult to incorporate directly into a computational simulation, we try to integrate over them in order to obtain the partition function that depends only on the gauge fields and on which the previously discussed algorithms could hopefully be applied. After taking into account the transformation properties of Grassmann variables, we can indeed integrate out the fermion field variables and the partition function now reads

$$Z = \int [DU][D\psi][D\bar{\psi}] e^{-S_G(U)} (\det D(U))^2. \quad (3.50)$$

For a detailed derivation, see for example [29]. Due to γ_5 -hermicity of the Dirac operators considered in this work ($\gamma_5 D = D^\dagger \gamma_5$) we have $\det D = \det D^\dagger$ and in the future we will take advantage of this property by writing $\det[D^2(U)]$ as $\det[D(U)D^\dagger(U)]$.

It is evident that the methods used to simulate pure gauge theory need to be modified to include the effect incorporated in the fermion determinant $\det D(U)$. This determinant is a non-local object, therefore its computation after each change of the gauge field would be numerically extremely expensive. The way out of this problem is to simulate the determinant by introducing the *pseudofermion field* ϕ . This is a bosonic field that has the same number of degrees of freedom as the corresponding fermionic variable (color, Dirac and space-time). Its introduction was motivated by the analogy between the fermionic and bosonic Gaussian integrals which allows us to express the fermion determinant as a Gaussian integral of the

3.7 Including dynamical fermions in simulations

pseudofermion fields

$$\det[D^\dagger D] = \int [D\psi][D\bar{\psi}] e^{-\sum_{f=1}^2 \bar{\psi}_f D(U) \psi_f} \propto \int [D\phi][D\phi^\dagger] e^{-\phi^\dagger (D^\dagger(U) D(U))^{-1} \phi}, \quad (3.51)$$

where the identity holds up to an irrelevant constant. The partition function with the new bosonic integration variables, for the considered system of two degenerate fermion flavors, is now proportional to

$$Z = \int [DU] e^{-S_G} \det(D^\dagger D) = \int [DU][D\phi][D\bar{\phi}] e^{-S^{\text{eff}}} \quad (3.52)$$

$$S^{\text{eff}}(U, \phi, \phi^\dagger) = S_G(U) + S_{\text{PF}}(U, \phi, \phi^\dagger), \quad (3.53)$$

$$S_{\text{PF}}(U, \phi, \phi^\dagger) = -\phi^\dagger (D(U) D^\dagger(U))^{-1} \phi. \quad (3.54)$$

If the determinant $\det D(U)$ is itself positive, then one may even be able to simulate a single fermion flavor from eq. 3.51. In this case, one approximates an inverse $D^{-1}(U)$ by some operator TT^\dagger during the molecular dynamics part of the HMC and corrects for this approximation in the accept-reject step at the end of the trajectory. For the approximation of TT^\dagger different polynomial or rational functions can be used. This approach is widely used in simulations of an odd number of flavors or in simulations with degenerate quark masses taken into account dynamically, for example the so-called $N_f = 2 + 1$ simulations, which include 2 degenerate massless u, d quarks and a heavier s quark. Since in this work we are interested exclusively in simulating an even number of dynamical fermion flavors with degenerate masses ($N_f = 2$ and $N_f = 4$), we will not discuss this approach further.

The argumentation similar to the one for two flavors holds for applying an arbitrary number of pseudofermions. For completion, we define the partition function for the theory of N_f fermion flavors, which can be interpreted as a probability measure if N_f is even

$$Z = \int [DU][D\phi][D\bar{\phi}] e^{-S_G} \det(D^\dagger D)^{N_f/2} = \int [DU][D\phi][D\bar{\phi}] e^{-S^{\text{eff}}} \quad (3.55)$$

$$S^{\text{eff}} = S_G - S_{\text{PF}}, \quad (3.56)$$

$$S_{\text{PF}} = -\phi_1^\dagger (DD^\dagger)^{-1} \phi_1 - \phi_2^\dagger (DD^\dagger)^{-1} \phi_2 + \dots \phi_{N_f/2}^\dagger (DD^\dagger)^{-1} \phi_{N_f/2}. \quad (3.57)$$

In the above formulae, we have dropped the dependence of the Dirac operator on the gauge field and from now on we will write it only when necessary.

The HMC algorithm may now be applied for simulating the theory with an even number of fermion flavors N_f . The creation of pseudo fermion fields is simple: they can, for example, be created by generating a complex vector χ with

3 Lattice QCD Simulations

Gaussian distribution $e^{-\chi^\dagger \chi}$ and then determining $\phi = D\chi$. They do not get updated during the HMC trajectory. The modification needed for the procedure discussed in section 3.4 is that now the momenta are generated with probability distribution

$$P(\pi) \propto e^{\frac{1}{2}(\pi, \pi)}. \quad (3.58)$$

The HMC steps for updating the gauge fields and momenta follow as for the pure gauge case, but instead of the one in eq. 3.36 the Hamiltonian used here is extended with the pseudofermion action

$$\mathcal{H}(\pi, U) = \frac{1}{2}(\pi, \pi) + S_G(U) + S_{\text{PF}}(U, \phi, \phi^\dagger). \quad (3.59)$$

The force that drives the molecular dynamics evolution now has a part coming from the gauge action (discussed in section 3.6) and a part coming from the pseudofermion action which will be discussed in detail in Chapter 4.

Introducing dynamical fermions into simulations was an important and necessary step in lattice QCD simulations for turning them into a precision tool. The effect of considering the fermions dynamically is not negligible and we illustrate it (cf. Figure 3.1) by quoting the figure from [60], which compares the values of several observables computed in pure gauge theory and in the theory with $N_f = 2 + 1$ dynamical fermions in the *asqtad* regularization.

3.8 Algorithm preconditioning

Introducing fermions into simulations requires a new evaluation of the fermion determinant for each update of the gauge field. We have seen in section 3.7 that this evaluation includes the inversion of the Dirac operator D . Such an inversion becomes very costly when the quark mass approaches physical values and when striving to achieve finer lattice resolutions in the simulations. The stochastic determination of the fermion determinant with pseudofermions introduces additional noise which tends to destabilize the HMC algorithm and requires smaller step sizes in the integration of the fermionic forces. The methods which attempt to reduce the noise of the stochastic estimator of the determinant will in the following be referred to as methods for *algorithm preconditioning*³. The algorithm

³Generally, *preconditioning* (or *solver preconditioning*) refers to the techniques for transforming the original linear system into one which has the same solution, but is more easily solvable by the iterative solver (has a smaller condition number). Although we use the term *algorithm preconditioning* in a different context, it usually gives us the factorization of the determinant such that the factors also have smaller condition numbers than the original problem. This should not be confused with *solver preconditioning* in terms of the above definition.

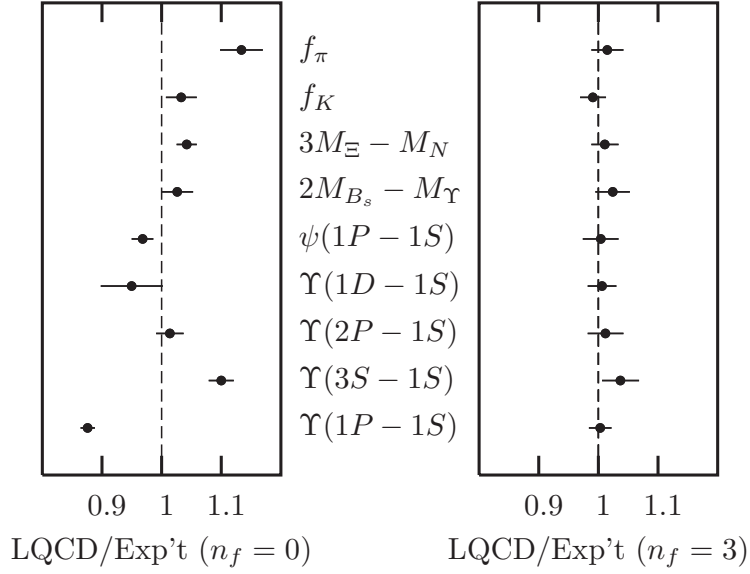


Figure 3.1: Comparison of the ratio of lattice QCD and experimental values for several observables, where the lattice QCD calculations are done in the quenched approximation (left panel) and with 2+1 flavors of asqtad sea quarks (right panel). The figure is taken over from [60].

preconditioning methods speed up the HMC simulations with dynamical quarks by factorizing the quark determinant such that the infra-red and ultra-violet contributions are treated separately. This leads to the reduction of the quark force magnitude in the molecular dynamics equations. Therefore, the associated integration step sizes can be set to larger values, which accelerates the algorithm. Different techniques for preconditioning the Hybrid Monte Carlo algorithm have played a key role in the process of making simulations with light sea quarks realistic with the available computational resources.

Up to the year 2000, performing continuum limit of simulations towards physical quark masses seemed impossible with the current algorithmic techniques for the dynamical fermion simulations (cf. the full line in Figure 3.2). The breakthrough in speeding up the dynamical HMC simulations was made by developing various HMC algorithm preconditioning methods, the most important being the so-called *domain decomposition* [64] and *Hasenbusch (mass) preconditioning* [65, 66]. In both of these approaches, the quark determinant is factorized into two or more parts, where some parts are dominated by infrared and at least one is largely ultraviolet. This leads to the reduction of the quark force magnitude in the molecular dynamics equations. Therefore, the associated integration step sizes can be set to larger values, and an acceleration of the algorithm is achieved. We will have a closer look at the principles on which these two methods are based in the following. Before we do so, we describe another method for the precondi-

3 Lattice QCD Simulations

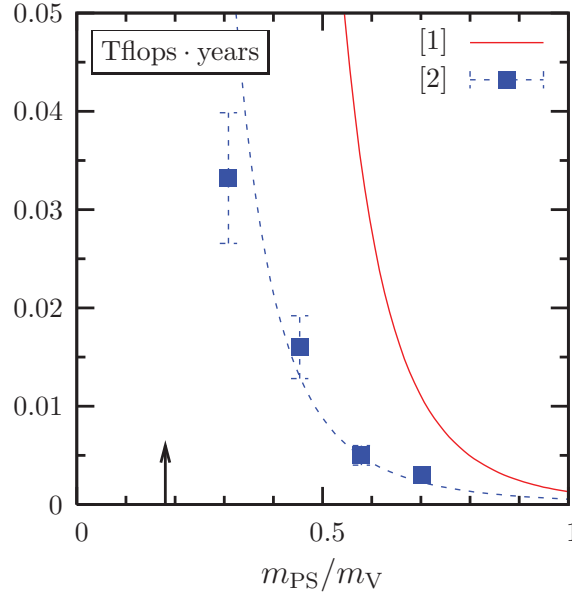


Figure 3.2: Computer resources needed to generate 1000 independent configurations of size $24^3 \times 40$ at a lattice spacing of about 0.08 fm with Wilson fermions in units of Tflops · years as a function of m_{PS}/m_V . The full line shows the prediction from the 2001 lattice conference in Berlin[61] (hence titled *Berlin Wall plot*), while the dashed line shows the cost of a mass preconditioned HMC algorithm published in [62] scaled to the same lattice extent. The plot is taken over from Ref. [63].

tioning of the HMC algorithm which was invented in the early nineties but only in combination with one of the previously mentioned methods for the determinant splitting leads to a significant acceleration of dynamical QCD simulations (cf. the dashed line Figure 3.2).

3.8.1 Multiple Time Scales

The first application of multiple time scales was made by Sexton and Weingarten [67], who noticed that separating the integration of the cheaper gauge force from the more expensive fermion force can be advantageous. Namely, reducing the error from the gauge force by integrating it in smaller MD steps allows a larger step size for the fermion force that costs more to evaluate. A careful choice of the step sizes ratio can make the total cost of the simulation smaller while keeping at the same time the acceptance rate roughly constant.

In practice it is performed as following. The Hamiltonian of the theory that includes dynamical fermionic degrees of freedom is given in eq. 3.59. Let us denote a single update of the momenta induced by the fermionic part of the Hamiltonian

3.8 Algorithm preconditioning

with $\mathcal{T}_F(\epsilon)$. $\mathcal{T}_F(\epsilon)$ is defined equivalently to the previously discussed momenta update governed by the gauge force in eq. 3.27,

$$\mathcal{T}_F(\epsilon) : (U, \pi) \rightarrow (U, \pi - \epsilon F^{\text{PF}}) \quad (3.60)$$

with a difference that F^{PF} denotes here the fermion force obtained from the variation of the pseudofermion action S_{PF} (for explicit expression of the fermion force see section 4.2.1). The step size of the momentum update from the fermion force is $\epsilon_F = \tau/N$. In other words, during the molecular dynamics trajectory of length τ , we integrate the fermion force in N steps $[\mathcal{T}_F(\epsilon_F)]^N$. If we want to update the pure gauge part of the Hamiltonian M times more frequently, then the overall update step for the time interval ϵ_F , in the case of the Leapfrog integrator, consists of

$$\mathcal{T}(\epsilon_F) = \mathcal{T}_F(\epsilon_F/2) [\mathcal{T}_{YM}(\epsilon_F/M)]^M \mathcal{T}_F(\epsilon_F/2). \quad (3.61)$$

\mathcal{T}_{YM} is a joint name for the evolution of the gauge fields \mathcal{T}_U and the evolution of momenta governed by the gauge force \mathcal{T}_G

$$\mathcal{T}_U(\epsilon) : (U, \pi) \rightarrow (e^{\epsilon\pi} U, \pi), \quad (3.62)$$

$$\mathcal{T}_G(\epsilon) : (U, \pi) \rightarrow (U, \pi - \epsilon F^G) \quad (3.63)$$

$$\mathcal{T}_{YM}(\epsilon_G) = \mathcal{T}_U(\epsilon_G/2) \mathcal{T}_G(\epsilon_G) \mathcal{T}_U(\epsilon_G/2). \quad (3.64)$$

Due to the recursive structure of 3.61, throughout the trajectory of the length $\tau = N\epsilon_F$ the total gauge/momenta update \mathcal{T}_{YM} is applied $N \times M$ times.

We have, for simplicity, used in our illustration the Leapfrog integrator, whereas Sexton and Weingarten originally applied this strategy to the variant of the Omelyan integrators (section 3.5.2) with the parameter choice $\lambda = 1/6$, which is, in combination with multiple time scales, also known in literature as the *Sexton Weingarten integration scheme*. This procedure can be generalized to the case where the fermion action itself is split into several terms

$$S = S_G + S_{\text{PF}_1} + S_{\text{PF}_2} + \dots + S_{\text{PF}_N}, \quad (3.65)$$

when computing some factors is more expensive than computing others. Different variants of preconditioning the fermion action will be discussed in following sections. With a clever choice of preconditioning and its parameters, the most expensive part can contribute least to the total force and can then be integrated with the largest step size, which makes a multiple scale integration a very useful computational tool. The optimal advantage of this method is achieved with the parameter choice where the residual error from the most expensive fermion force dominates the overall error.

3.8.2 Domain Decomposition

The application of the Schwartz alternating procedure to the HMC algorithm by M. Lüscher [68, 69] is based on the partitioning of the lattice into hypercubic subdomains - therefore this method is known as the *domain decomposed HMC* algorithm or, for short, *DD-HMC*. The division of the lattice is defined such that the

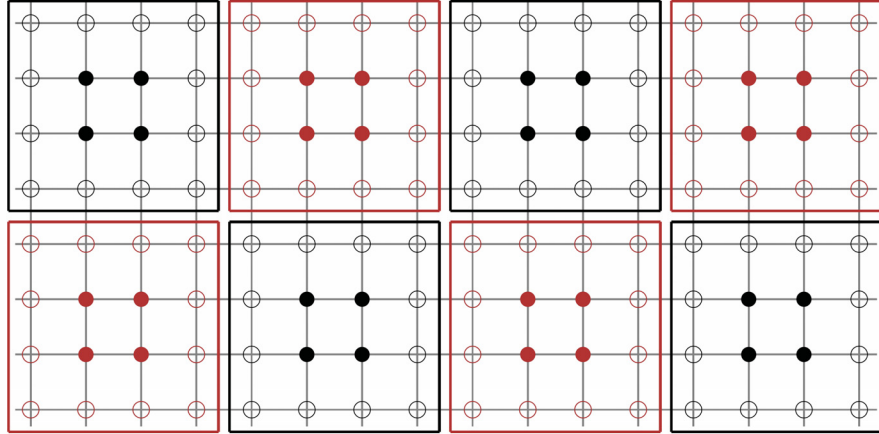


Figure 3.3: Two-dimensional cross-section of a $8^3 \times 16$ lattice covered by non-overlapping 4^4 blocks. The domains Ω and Ω^* are the unions of the black and red blocks respectively, and their exterior boundaries $\partial\Omega$ and $\partial\Omega^*$ consist of all points in the complementary domain represented by open circles.

blocks can be colored red and black in a chessboard style (see Figure 3.3). The idea is to utilize the subdomains to separate the short range interaction (interaction between the filled points inside each block) from ultraviolet contributions (interaction between the blocks) and, at the same time, have even-odd preconditioning. Let us denote the set of sites inside the black-colored blocks (filled circles) with Ω and the set of sites inside the red-colored ones with Ω^* . The Dirac matrix can now be decomposed as following

$$D = \begin{pmatrix} D_{\Omega^*} & D_{\partial\Omega^*} \\ D_{\partial\Omega} & D_{\Omega} \end{pmatrix}, \quad (3.66)$$

where we have denoted with $\partial\Omega$ and $\partial\Omega^*$ the sets of boundary points of black and red blocks (open circles), and D_X denotes the Dirac operator reduced on the set of points X . The matrix D can be further decomposed

$$D = \begin{pmatrix} D_{\Omega^*} & 0 \\ D_{\partial\Omega} & 1 \end{pmatrix} \begin{pmatrix} 1 & D_{\Omega^*}^{-1} D_{\partial\Omega^*} \\ 0 & D_{\Omega} - D_{\partial\Omega} D_{\Omega^*}^{-1} D_{\partial\Omega^*} \end{pmatrix}, \quad (3.67)$$

3.8 Algorithm preconditioning

such that the fermion determinant can now be written as

$$\det D = \det D_\Omega \det D_{\Omega^*} \det[1 - D_\Omega^{-1} D_{\partial\Omega} D_{\Omega^*}^{-1} D_{\partial\Omega^*}] \quad (3.68)$$

$$= \det D_1 \det D_2, \quad (3.69)$$

$$D_1 = \begin{pmatrix} D_{\Omega^*} & 0 \\ 0 & D_\Omega \end{pmatrix}, D_2 = 1 - D_\Omega^{-1} D_{\partial\Omega} D_{\Omega^*}^{-1} D_{\partial\Omega^*}.$$

The matrix D_1 describes the ultraviolet part of the fermion dynamics restricted to the interior of each subdomain and its complement D_2 couples the blocks and carries the infrared behaviour. In the simulation one uses separate pseudofermion fields for these two factors. The fermion force coming from the first factor is computed by inverting small matrices restricted to a single domain. In this step the Dirichlet boundary conditions are applied on each domain. Namely, the gauge fields across the domain boundaries are fixed to the values of its recent update and remain unchanged during the molecular dynamics trajectory. In the following, we will refer to the gauge links inside the blocks, which get updated during the trajectory, as *active links*. Updating only the links inside the domains results in reduced communication, and makes the computer simulations less expensive. In order to avoid artifacts from updating only a fraction of the links, after each MD trajectory the domains are shifted by a random space-time displacement.

The fermion force coming from the factor D_2 is computationally more expensive than the force inside the blocks, therefore applying the multiple time scales here, as previously discussed, is very advantageous.

3.8.3 Hasenbusch Preconditioning

In section 3.8.2 the basis for the factorisation of the fermion matrix was spacial decomposition. On the other hand, it is also possible to precondition the fermion matrix with the factors that can be written as a function of the fermion matrix. This preconditioning method has been introduced by M. Hasenbusch [65] and after a very promising test in the Schwinger model framework, its application to QCD [66] was no less successful. The fermion determinant is preconditioned with a fermion of a larger mass ($\Delta m > 0$)

$$\det D = \det W \det\{W^{-1}D\}, \quad (3.70)$$

$$W = D + \Delta m, \quad (3.71)$$

therefore this method is also known as *mass preconditioning*. The splitting of the fermion determinant 3.70 leads to the effective fermion action

$$S_F^{\text{eff}} = \phi_1^\dagger (WW^\dagger)^{-1} \phi_1 + \phi_2^\dagger (W^{-1}D(W^{-1}D)^\dagger)^{-1} \phi_2, \quad (3.72)$$

3 Lattice QCD Simulations

where each factor can be simulated with a separate pseudofermion pair. For a successful choice of Δm , the condition number of both W and $W^{-1}D$ needs to be smaller than their product. Additionally, if Δm is chosen such that the forces associated with the pseudofermion field ϕ_2 have significantly smaller magnitudes than those associated to ϕ_1 , then multiple time scale can be successfully applied and save several more factors in the total computational cost.

The value of the mass parameter Δm plays the role of the infrared cutoff in a similar way as the size of the blocks in domain decomposition. The advantage of the mass parameter here is that it is continuous and therefore allows for more tuning options. One can easily apply the above trick to the Hermitian Dirac operator or any of its even-odd preconditioned versions. Also, introducing more than one preconditioning fermion is straightforward (cf. Appendix 4).

4 MP-HMC program package

There are several publicly available lattice QCD packages that are able to simulate Wilson fermions, such as Chroma code [70], tmQCD [63], MIMD Lattice Collaboration (MILC) Code, DD-HMC [69] and the recently published openQCD package by M. Lüscher and S. Schäfer [71]. The DD-HMC with the deflated solver (versions DD-HMC-1.2.x) is a very efficient code for simulating $O(a)$ improved Wilson fermions [64, 68]. It has been shown in practice that this code scales particularly well with the quark mass [72] and this has encouraged the groups around CLS¹ [73] to make DD-HMC the algorithm of choice in their effort to simulate light Wilson quarks at fine lattice spacings in the two flavor approximation of QCD.

We have seen in section 3.8 that a preconditioning of the HMC algorithm is a prerequisite for simulating dynamical fermions with light quark masses (cf. Figure 3.2). Nevertheless, it is not a priori clear which choice of preconditioning the HMC algorithm is optimal for a particular lattice QCD setup. We recall that the core idea of HMC algorithm preconditioning is to separate ultraviolet from infrared contributions to the fermion determinant. In this way, the computationally more expensive and less stable part with the infrared modes ultimately corresponds to the relatively small force and therefore can be integrated less often. Both domain decomposition 3.8.2 and Hasenbusch preconditioning 3.8.3 achieve this separation.

Despite its high effectiveness, the intrinsic structure of the DD-HMC algorithm puts some constraints on the exploration of modern computational resources, in the simulations of large lattices. This was our motivation for using it to develop an implementation of the mass preconditioned HMC, reusing as many building blocks of DD-HMC as possible, most importantly its locally deflated solver which is in large part responsible for the excellent scaling behavior of the DD-HMC code. In this chapter we review shortly the basics of the DD-HMC program package and comment on the hardware constraints in the application of the DD-HMC algorithm. Afterwards, we describe in detail the algorithmic choices we made in our implementation of mass preconditioned HMC [74]. Next, we give a comparison of the two setups in a realistic simulation and give some final remarks on the

¹Coordinated Lattice Simulations (CLS) is a community effort, launched in 2007, whose aim is to bring together the human and computer resources of several teams in Europe. One of the main goals of CLS is to perform lattice QCD simulations in a wide range of quark masses, lattice spacings and lattice volumes, using a single lattice formulation of the theory.

4 MP-HMC program package

performance of the MP-HMC program.

4.1 DD-HMC overview

The program package DD-HMC utilizes the domain decomposition described in section 3.8.2 as a preconditioner of the HMC algorithm. It is designed to be able to simulate a doublet of $O(a)$ improved Wilson quarks at small quark masses and lattice spacings smaller than 0.1fm. This way of preconditioning the HMC algorithm is known under the names *domain decomposition* and *Schwarz alternating procedure*² (SAP). The decomposition of the lattice into non-overlapping domains, both in the solver and in the molecular dynamics updates makes this approach extremely suitable for parallel processing.

In the DD-HMC, the quark determinant is written as the product of the determinants of the Dirac operator restricted to the blocks and a factor that accounts for the remaining contributions to the fermion determinant (eq. 3.69). The latter factor couples the gauge fields on the different blocks and the quark force related to it includes the contributions of the low lying modes of the Dirac operator. Therefore, the calculation of the block-interaction force consumes most of the computer time needed for one molecular dynamics trajectory. Here the Dirac equation has to be solved for two quark source fields on the full lattice. The solver used for the computation of the global force combines the classical Schwarz alternating procedure with a standard Krylov space solver (the GCR algorithm)[76]. The latest version of this package (DD-HMC-1.2.0 and newer) include the acceleration of the GCR solver with the local deflation. The idea of local deflation of the Wilson Dirac operator is proposed and documented in Ref. [77, 78].

The inclusion of a deflated solver has brought a significant decrease in the average number of iterations in the computation of the block interaction force and reduced significantly the dependence of the time needed per MD trajectory on the quark mass. The later is illustrated in figure 4.1 taken over from Ref. [78].

As we have already noted in [74], the DD-HMC blocks separate the infrared from the ultraviolet physics and therefore should have a certain physical size of 0.5fm to 1fm. This, however, introduces some drawbacks in practical applications. Since the blocks are tied to the parallel layout of the lattice across the nodes of the computer, one would like them to be as small as possible to make full use of the massively parallel capabilities of the available supercomputers. In particular, due to an even/odd structure of the problem, two such HMC blocks have to reside on each core. On the other hand, from a certain point on, this degrades the performance of the algorithm, because the physical volume of a block become too

²The Schwartz alternating procedure (SAP) does not necessarily have to refer to the decomposition of the lattice into non-overlapping domains, as it is the case here. In fact, in Schwarz's original proposal [75], the procedure for the two overlapping domains has been worked out.

4.2 Algorithmic choices in MP-HMC

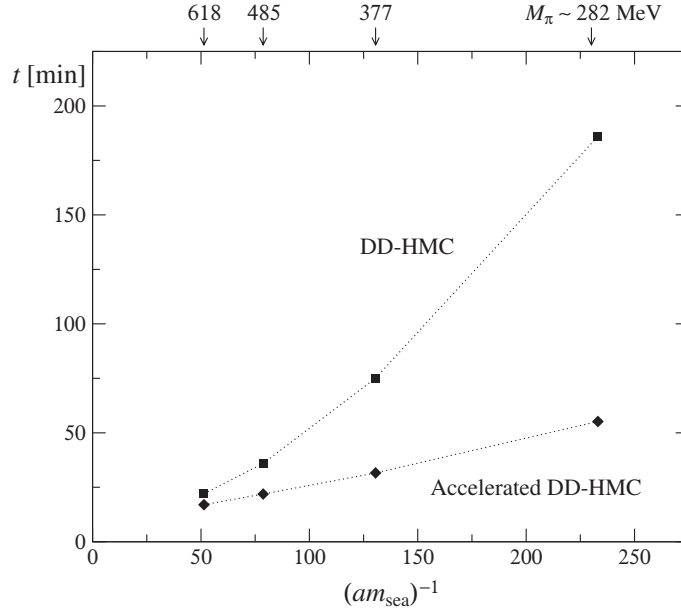


Figure 4.1: Average execution times required for a single MD trajectory plotted against the inverse of the bare current-quark mass m_{sea} given in lattice units, for a typical set of lattice parameters for the DD-HMC algorithm. The timings originate from a PC cluster with 64 cores and the lattice size in this test is 64×32^3 . The figure is taken over from Ref. [78].

small. Also small blocks with their large surface reduce the number of updated links. Let us recall that in this algorithm the links on the boundaries of the blocks are frozen and only the links inside the blocks or those touching the boundary are updated during the MD trajectory. While this has advantages in reducing overall communication, it increases the autocorrelation time. For the simulations of large lattices with small quark masses, the above restrictions are not any more outweighed by the excellent performance of the algorithm.

4.2 Algorithmic choices in MP-HMC

We have argued in the previous section that with the DD-HMC algorithm, there is a competition between the need of physics and the need of the computer, which sets a limitation on the maximal number of CPUs that can be used in the simulations. A solution that allows for more flexibility in the choice of parallelization, but also potentially stabilizes and speeds up the simulation in the framework we are addressing, was to replace the domain decomposition preconditioning of the quark determinant with the Hasenbusch mass preconditioning (cf. Sec. 3.8.3).

4 MP-HMC program package

Mass preconditioned HMC has been used previously for QCD simulations with periodic boundary conditions by different collaborations, e.g. [62, 79], but our work [74] represents the first experience of mass preconditioning together with the deflated solver.

Since DD-HMC is such an efficient program package incorporating all modern algorithmic improvements, we have started from the latest publicly available DD-HMC version, minimizing changes to the original code. In this way, we have managed to retain the advantages of this code, such as the highly optimized parallelization of the block solver, single precision acceleration and many others, but most importantly, the previously mentioned deflated solver for the Dirac equation at low quark masses.

We have named our package MP-HMC after the main characteristics of this code - the mass preconditioning of the HMC algorithm. MP-HMC simulates $N_f = 2$ degenerate flavors of non-perturbatively $O(a)$ improved Wilson quarks. We recall here the Dirac operator in this formulation

$$D(m) = D_W + c_{SW} \sum_{\mu, \nu} \frac{i}{4} \sigma_{\mu\nu} \hat{F}_{\mu\nu} + m, \quad (4.1)$$

where D_W represents the unimproved Wilson Dirac operator without the mass term, $\hat{F}_{\mu\nu}$ represents the clover contribution discussed in section 2.5, c_{SW} is the improvement coefficient and m is the bare mass of the unimproved Wilson fermions. In the gauge sector, as well as in the DD-HMC case, we use the Wilson gauge action discussed in section 2.3.

In the following we will discuss the main algorithmic choices we made for developing this code. We begin with the fermion force, since the HMC simulation program usually spends the largest fraction of the total execution time computing these forces. The discussion from section 3.6 will be extended to the case of $O(a)$ improved Wilson fermions, adopted to fit with our choices of the HMC algorithm preconditioning.

4.2.1 Fermionic Forces

In section 3.6 we derived the expression for the gauge force associated with the Wilson plaquette action (eq. 3.45). This is a local expression, therefore the computation of the gauge force is straightforward and computationally cheap compared to the force associated with fermions. The latter, on the other hand, involves parts that have to be estimated stochastically and there are different ways in which one can do fermion force evaluation. Here we describe in detail the computation of the fermion force, associated with the $O(a)$ improved Wilson action (eq. 4.1) and to our algorithmic choices.

For the following considerations, we shall exploit the fact that the Wilson Dirac

4.2 Algorithmic choices in MP-HMC

fermion matrix is γ_5 Hermitian, namely $\gamma_5 D(m) \gamma_5 = D^\dagger(m)$. We may now construct the Hermitian Dirac operator

$$Q(m) = \gamma_5 D(m). \quad (4.2)$$

Since the determinant of γ_5 matrix is $\det \gamma_5 = 1$ (cf. appendix A), for the evaluation of the fermion determinant we can use the Hermitian Dirac operator $Q(m)$. Equivalent considerations for the Dirac matrix $D(m)$ itself can easily be obtained by putting $D(m) = \gamma_5 Q(m)$ back in all expressions that will follow. From here on we also omit writing down the quark mass dependence of the Hermitian Dirac operator Q .

Symmetrical even-odd preconditioning of the HMC algorithm

The Hermitian Dirac operator can be written in block form

$$Q = \begin{pmatrix} Q_{ee} & Q_{eo} \\ Q_{oe} & Q_{oo} \end{pmatrix}, \quad (4.3)$$

where Q_{ee} is supported on the even sites³ of the lattice, Q_{oo} on the odd sites, while Q_{eo} and Q_{oe} denote the hopping terms from the odd to the even and the even to the odd points respectively. Blocks of Q that connect lattice points of equal parity correspond to the following contributions to the Hermitian Dirac operator

$$Q_{ee} + Q_{oo} = \gamma_5 \{ 4 + m_0 + c_{\text{SW}} \sum_{\mu, \nu} \frac{i}{4} \sigma_{\mu\nu} \hat{F}_{\mu\nu} \}, \quad (4.4)$$

and the sum of the hopping terms incorporating the interaction of the neighboring lattice points equals

$$Q_{eo} + Q_{oe} = -\gamma_5 \sum_{\mu=0}^3 \frac{1}{2} \{ U_\mu(x) (1 - \gamma_\mu) \delta_{x+\hat{\mu}, x'} + U_\mu^\dagger(x) (1 + \gamma_\mu) \delta_{x-\hat{\mu}, x'} \}. \quad (4.5)$$

The Schur complement of block Q_{oo} of the matrix Q is denoted as the asymmetrically preconditioned Dirac operator \hat{Q}

$$\hat{Q} = Q_{ee} - Q_{eo} Q_{oo}^{-1} Q_{oe}. \quad (4.6)$$

³A lattice site is defined to be even if the sum of all lattice coordinates is even, i.e. the point $x = (x_0, x_1, x_2, x_3)$ is even if $2|(x_0 + x_1 + x_2 + x_3)$, otherwise x is odd.

4 MP-HMC program package

The determinant of the Hermitian Dirac operator can now be written in the so-called *asymmetrically even-odd preconditioned* form

$$\det Q = \det Q_{oo} \det \hat{Q}. \quad (4.7)$$

Similarly, the symmetrically preconditioned Hermitian Dirac operator Q_S is obtained by multiplying the asymmetrical one with the inverse of Q_{ee}

$$Q_S = Q_{ee}^{-1} \hat{Q} \quad (4.8)$$

$$= 1 - Q_{ee}^{-1} Q_{eo} Q_{oo}^{-1} Q_{oe}. \quad (4.9)$$

Let us note how the above preconditioned matrices behave under Hermitian conjugation

$$\hat{Q}^\dagger = \hat{Q}, \quad (4.10)$$

$$Q_S^\dagger = Q_{ee} Q_S Q_{ee}^{-1}. \quad (4.11)$$

The determinant of a full Hermitian Dirac operator can now be split up in a more symmetrical way, which is known as *symmetrical even-odd preconditioning*

$$\det Q = \det Q_{ee} \det Q_{oo} \det Q_S. \quad (4.12)$$

This factorization was applied to the fermion determinant in a MP-HMC simulation program. The motivation for doing this comes from the fact that the Dirac operator we are considering only has a nearest neighbor coupling, therefore the first two factors on the right hand side of eq. 4.12 can be evaluated rather easily. In our case, their computation could be taken over completely from the DD-HMC program. The third factor, $\det Q_S$, is determined stochastically along the lines of section 3.7. We shall now derive explicit expressions for the molecular dynamics forces corresponding to the symmetric factorization of the $O(a)$ improved Wilson Dirac operator, with one important caveat. Namely, although we pursue the symmetric preconditioning of the Dirac operator, all the expressions we give will still be written as functions of the full Dirac operator Q . The reason for this is that we already had a very efficient solver for the full Dirac operator available from the DD-HMC program and we wanted to use it in our implementation of MP-HMC. Developing a special deflated solver for Q_S or even its further preconditioned factors would be an extremely tedious task and may not lead to better algorithm efficiency than the one we propose here⁴.

We consider two flavors of dynamical quarks, therefore the even-odd precon-

⁴To the knowledge of the author, this issue has not yet been addressed in existing publications and it would be an interesting topic for further investigations related to solver studies and the performance of HMC simulations in general.

ditioned determinant that we want to evaluate reads

$$\det QQ^\dagger = \det Q_{ee}^2 \det Q_{oo}^2 \det(Q_S Q_S^\dagger). \quad (4.13)$$

Using the identity 3.51, the determinant of the symmetrically preconditioned Hermitian Dirac operator can be expressed via the pseudofermion field ϕ_e which only lives the even lattice sites only

$$\det(Q_S Q_S^\dagger) = \int [D\phi_e] [D\phi_e^\dagger] e^{-S_{\text{PF}}}, \quad (4.14)$$

where the corresponding pseudofermion action reads

$$\begin{aligned} S_{\text{PF}} &= (Q_S^{-1} \phi_e, Q_S^{-1} \phi_e) \\ &= (\hat{Q}^{-1} Q_{ee} \phi_e, \hat{Q}^{-1} Q_{ee} \phi_e). \end{aligned} \quad (4.15)$$

In order to compute the force corresponding to this effective action, we need to compute its variation with respect to the change of the gauge field

$$\begin{aligned} \delta S_{\text{PF}} &= \phi_e^\dagger \delta \{Q_S^{\dagger-1} Q_S^{-1}\} \phi_e \\ &= \phi_e^\dagger \left[\delta \{Q_S^{\dagger-1}\} Q_S^{-1} + Q_S^{\dagger-1} \delta \{Q_S^{-1}\} \right] \phi_e. \end{aligned} \quad (4.16)$$

The inverse of the asymmetrically and symmetrically even-odd preconditioned Dirac operator can be expressed via the inverse of the full Dirac operator

$$\{\hat{Q}^{-1}\} = P_e Q^{-1} P_e, \quad (4.17)$$

$$\{Q_S^{-1}\} = P_e Q^{-1} Q_{ee} P_e. \quad (4.18)$$

Here P_e represents the projection operator to the even points of the pseudofermion field and full derivation of the above identities can be found in appendix 2. We obtain further the variation of Q_S^{-1} as the function of the variation of the full Hermitian Dirac operator Q :

$$\begin{aligned} \delta \{Q_S^{-1}\} &= \delta \{P_e Q^{-1} Q_{ee} P_e\} \\ &= P_e \delta \{Q^{-1} Q_{ee}\} P_e \\ &= P_e [\delta \{Q^{-1}\} Q_{ee} + Q^{-1} \delta \{Q_{ee}\}] P_e \\ &= P_e [-Q^{-1} \delta \{Q\} Q^{-1} Q_{ee} + Q^{-1} \delta \{Q_{ee}\}] P_e \end{aligned} \quad (4.19)$$

$$\begin{aligned} \delta \{Q_S^{\dagger-1}\} &= [\delta \{Q_S^{-1}\}]^\dagger \\ &= P_e [-Q_{ee} Q^{-1} \delta \{Q\} Q^{-1} + \delta \{Q_{ee}\} Q^{-1}] P_e. \end{aligned} \quad (4.20)$$

4 MP-HMC program package

In the previous derivation we have used that Q and Q_{ee} are both Hermitian operators, as well as the identity

$$\delta\{O^{-1}\} = -O^{-1}\delta\{O\}O^{-1}. \quad (4.21)$$

The equation 4.16 can now be rewritten as

$$\begin{aligned} \delta S_{pf} = & \phi_e^\dagger \left[P_e \left(-Q_{ee} Q^{-1} \delta\{Q\} Q^{-1} + \delta\{Q_{ee}\} Q^{-1} \right) P_e Q^{-1} Q_{ee} P_e \right. \\ & \left. + P_e Q_{ee} Q^{-1} P_e \left(-Q^{-1} \delta\{Q\} Q^{-1} Q_{ee} + Q^{-1} \delta\{Q_{ee}\} \right) P_e \right] \phi_e. \end{aligned} \quad (4.22)$$

In order to simplify the previous expression, we introduce the auxiliary variables

$$\begin{aligned} X &= Q^{-1} P_e Q^{-1} Q_{ee} P_e \phi_e = Q^{-1} P_e Q^{-1} Q_{ee} \phi_e \\ Y &= Q^{-1} Q_{ee} P_e \phi_e = Q^{-1} Q_{ee} \phi_e, \end{aligned} \quad (4.23)$$

and thus obtain

$$\delta S_{PF} = -Y^\dagger \delta\{Q\} X + \phi_e^\dagger P_e \delta\{Q_{ee}\} X + H.c. \quad (4.24)$$

If we now separate the contributions of the hopping and diagonal terms, the previous expression reads

$$\begin{aligned} \delta S_{PF} = & - \left(Y^\dagger \begin{bmatrix} 0 & \delta\{Q_{eo}\} \\ \delta\{Q_{oe}\} & 0 \end{bmatrix} X + H.c. \right) - \left(Z^\dagger \begin{bmatrix} \delta\{Q_{ee}\} & 0 \\ 0 & \delta\{Q_{oo}\} \end{bmatrix} X + H.c. \right) \\ = & \delta S_W + \delta S_{SW} \end{aligned} \quad (4.25)$$

where X and Y are those defined in equation 4.23 and Z can be obtained from Y and the original pseudofermion field

$$Z = \begin{bmatrix} Y_e - \phi_e \\ Y_o \end{bmatrix} = Y - \Phi, \quad \Phi = \begin{bmatrix} \phi_e \\ 0 \end{bmatrix}. \quad (4.26)$$

The first part of equation 4.25 corresponds to the hopping action that is equal to the unimproved Wilson fermion action, therefore the force coming from this variation will in the following be called *Wilson force* and denoted with the index “W”. The second term is the contribution of the Sheikholeslami-Wohlert term and its associated fermion force will be denoted with the index “SW”. In order to obtain the explicit expression for the Wilson force, we go back to equation 4.5

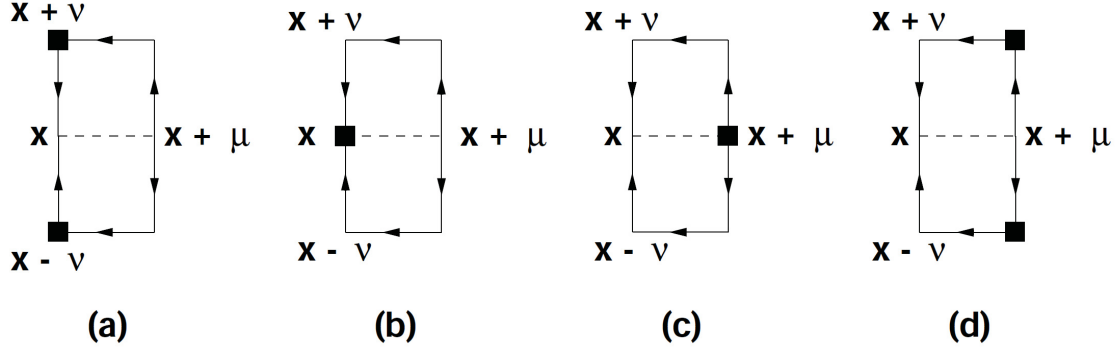


Figure 4.2: Diagrams of the contributions to F_μ^{SW} . The illustration is taken from Ref. [80].

and write down the variation of the hopping term of the action

$$\delta\{Q_{oe} + Q_{eo}\}_{xx'} = -\gamma_5 \sum_{\mu=0}^3 \frac{1}{2} \{ \delta U_\mu(x) (1 - \gamma_\mu) \delta_{x+\hat{\mu}, x'} + \delta U_\mu^\dagger(x) (1 + \gamma_\mu) \delta_{x-\hat{\mu}, x'} \}. \quad (4.27)$$

Using the definition of the molecular dynamics force 3.42 and the identity

$$Y^\dagger QX = \text{Tr}\{QX \otimes Y^\dagger\}, \quad (4.28)$$

we finally obtain the expression for the Wilson contribution to the fermionic force:

$$\begin{aligned} F_\mu^W(\text{x-even}) &= \frac{1}{2} \text{Tr} \{ \gamma_5 (1 - \gamma_\mu) Y_o(x + \hat{\mu}) \otimes X_e^\dagger(x) \\ &\quad + \gamma_5 (1 - \gamma_\mu) X_o(x + \hat{\mu}) \otimes Y_e^\dagger(x) \} \\ F_\mu^W(\text{x-odd}) &= \frac{1}{2} \text{Tr} \{ \gamma_5 (1 - \gamma_\mu) Y_e(x + \hat{\mu}) \otimes X_o^\dagger(x) \\ &\quad + \gamma_5 (1 - \gamma_\mu) X_e(x + \hat{\mu}) \otimes Y_o^\dagger(x) \}, \end{aligned} \quad (4.29)$$

where \otimes stands for the direct product in color space. Similarly, F_μ^{SW} is obtained from the second term in equation 4.25

$$F_\mu^{SW}(x) = (\text{diagrams in Figure 4.2}) \quad (4.30)$$

where the black squares denote the insertion obtained from the variation of equa-

4 MP-HMC program package

tion 4.4

$$(\blacksquare)_x = \frac{ic_{SW}}{4} \text{Tr} \left\{ \gamma_5 \sigma_{\mu\nu} X(x) \otimes Z^\dagger(x) + \gamma_5 \sigma_{\mu\nu} Z(x) \otimes X^\dagger(x) \right\} \quad (4.31)$$

The part of the determinant that involves only Q_{ee} and Q_{oo} does not need a stochastic estimation and can be computed exactly. Its contribution to the effective action is often denoted as the *determinant contribution*

$$(\det Q_{ee} \det Q_{oo})^2 = e^{-S_{det}}, \quad (4.32)$$

$$S_{det} = -2(\ln \det Q_{ee} + \ln \det Q_{oo}) \quad (4.33)$$

and its variation reads:

$$\delta S_{det} = -2 \delta \{ \ln e^{\text{Tr} \ln Q_{ee}} + \ln e^{\text{Tr} \ln Q_{oo}} \} \quad (4.34)$$

$$= -2 \text{Tr} \{ Q_{ee}^{-1} \delta Q_{ee} + Q_{oo}^{-1} \delta Q_{oo} \}. \quad (4.35)$$

Consequently, the corresponding contribution to the fermion force is called the *determinant force*. The force F_μ^{det} has two parts, originating from the even and the odd points, due to the symmetrical even-odd preconditioning, and it equals

$$F_\mu^{det}(x) = (\text{diagrams in Figure 4.3}) \quad (4.36)$$

where the black triangles in Figure 4.3 denote the following insertions depending on the parity of the point where the insertion is calculated

$$(\blacktriangle)_x = \frac{ic_{SW}}{2} \begin{cases} \text{Tr}[i\sigma_{\mu\nu} Q_{ee}^{-1}(x)] & \text{x-even,} \\ \text{Tr}[i\sigma_{\mu\nu} Q_{oo}^{-1}(x)] & \text{x-odd.} \end{cases} \quad (4.37)$$

The preceding discussion of the fermion forces does not yet include any of the preconditioning methods that separate infrared and ultraviolet contributions to the Dirac determinant, such as domain decomposition or Hasenbusch preconditioning. If one were to apply the expressions for the Wilson and Sheikholeslami-Wohlert force (equations 4.29 and 4.30) directly in the MP-HMC algorithm, moving towards the physical quark masses and small lattice spacings becomes unfeasible with the current computational resources (cf. Figure 3.2). Therefore, we proceed immediately to the computation of the forces that correspond to the mass preconditioned algorithm.

Hasenbusch preconditioning

The Hasenbusch preconditioning procedure is outlined in 3.8.3 and it can be applied in QCD simulations in many ways. In MP-HMC code we apply the Hasen-

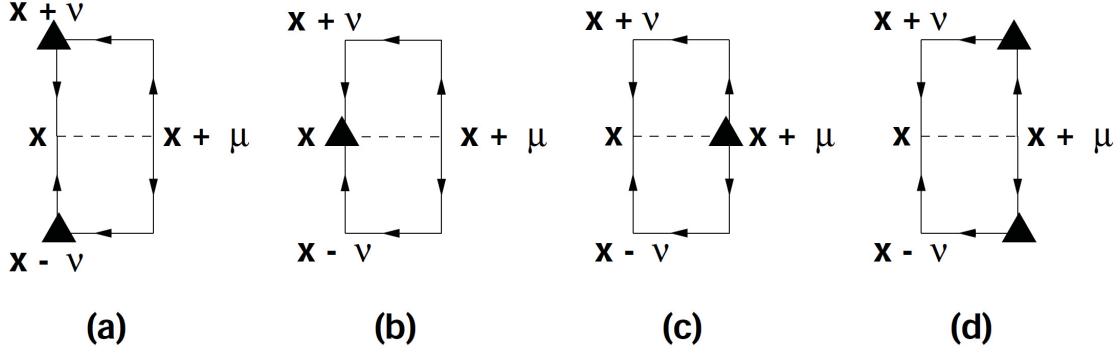


Figure 4.3: Diagrams of the contributions to F_μ^{det} . The illustration is taken from Ref. [80].

busch trick to the Schur complement from the symmetric even-odd preconditioning

$$\det[Q_S Q_S^\dagger] = \det[WW^\dagger] \det[(W^{-1}Q_S)(W^{-1}Q_S)^\dagger]. \quad (4.38)$$

The alternative would be to apply it to the full Hermitian Dirac matrix Q , or the asymmetrically preconditioned operator \hat{Q} . Preconditioning Q is obviously less effective than our choice of preconditioning Q_S , since Q_S is supported only in even points and its inversion is therefore much cheaper. On the other hand, the gain from applying mass preconditioning on top of symmetric or asymmetric even-odd preconditioning is not yet fully understood. Our motivation to start from the symmetric even-odd Dirac operator is based on the experience of the authors of [81], who found that applying the symmetric operator gives roughly 30% speed-up of the even-odd preconditioned HMC algorithm with respect to its asymmetric version. If a matrix W is chosen properly, the evaluation of the RHS of the equation 4.38 can have smaller computational costs than the direct evaluation of the LHS. The determinant could be split up in a more general way, into an arbitrary number of factors.

$$\begin{aligned} \det[Q_S Q_S^\dagger] &= \det[W_0 W_0^\dagger] \det[(W_0^{-1} W_1)(W_0^{-1} W_1)^\dagger] \\ &\dots \det[(W_{N_{PF}-1}^{-1} Q_S)(W_{N_{PF}-1}^{-1} Q_S)^\dagger]. \end{aligned} \quad (4.39)$$

For the evaluation of the above expression we need to introduce the additional pseudofermion field for each determinant appearing on the right hand side, therefore the counting of the terms goes up to N_{PF} . The corresponding effective fermion action reads

$$S_F^{eff} = -\text{Tr} \ln(W_0) - \text{Tr} \ln(W_0^{-1} W_1) - \dots - \text{Tr} \ln(W_{N_{PF}-1}^{-1} Q_S) \quad (4.40)$$

4 MP-HMC program package

The number of the pseudofermion fields is believed to add to the stability of the algorithm, but their number has to be balanced with respect to the total cost of the simulation with more pseudofermion pairs. For most of our runs, having three to five pseudofermion fields was the optimal choice (cf. section 4.3.3). In the following we discuss the special case with two pseudofermions defined in eq. 4.38. The generalization to more pseudofermions follows the same strategy and it is outlined in Appendix 4.

Let us denote the pseudofermion field used for the evaluation of the determinant of the preconditioning matrix W with ϕ_1 and the pseudofermion field needed for the evaluation of the preconditioned symmetrical Hermitian Dirac operator with ϕ_2 . We can then estimate the determinant of interest as follows

$$\det Q_S^\dagger Q_S \propto \int [D\phi_1^\dagger][D\phi_1][D\phi_2^\dagger][D\phi_2] e^{-\sum_{i=1}^2 S_{PF_i}} \quad (4.41)$$

$$S_{PF_1} = \phi_1^\dagger (WW^\dagger)^{-1} \phi_1 \quad (4.42)$$

$$S_{PF_2} = \phi_2^\dagger ([W^{-1}Q_S][W^{-1}Q_S]^\dagger)^{-1} \phi_2 \quad (4.43)$$

The identity 4.38 holds for an arbitrary invertible matrix W . In order to achieve a gain in the performance of the HMC algorithm by applying the Hasenbusch trick, the matrix W should be chosen such that it has a smaller condition number than Q_S . There are different ways in which one can make this choice and relate W to the operator that we want to precondition, namely Q_S . A standard and simplest choice would be to define it as

$$W = Q_S + \rho, \quad (4.44)$$

where ρ is real and positive. Let us first compute the variation of the second part of the pseudofermion action (equation 4.43), and later come back to its first part (equation 4.42)

$$\delta S_{PF_2} = \phi_2^\dagger \delta \{ W^\dagger Q_S^{\dagger-1} Q_S^{-1} W \} \phi_2. \quad (4.45)$$

After a few algebraic manipulations, we obtain

$$\delta S_{PF_2} = \phi_2^\dagger [(1 + \rho Q_S^{\dagger-1}) \rho \delta \{ Q_S^{-1} \} + H.c.] \phi_2. \quad (4.46)$$

With the help of equation 4.17 and 4.19 the inverse Q_S^{-1} and its variation become functions of Q^{-1} and this inverse can be computed with the efficient deflated solver from DD-HMC. Similarly to the single pseudofermion case, we can further simplify the expression

$$\delta S_{PF_2} = \phi_2^\dagger [(1 + \rho P_e Q_{ee} Q^{-1} P_e) \rho P_e (-Q^{-1} \delta \{ Q \} Q^{-1} Q_{ee} + Q^{-1} \delta \{ Q_{ee} \}) P_e + H.c.] \phi_2$$

by introducing auxiliary spinor variables

$$\begin{aligned} X &= \rho Q^{-1} P_e (1 + \rho P_e Q^{-1} Q_{ee} P_e) P_e \phi_2 = \rho Q^{-1} P_e (1 + \rho P_e Q^{-1} Q_{ee}) \phi_2 \\ Y &= Q^{-1} Q_{ee} P_e \phi_2 = Q^{-1} Q_{ee} \phi_2. \end{aligned} \quad (4.47)$$

Keeping in mind the modified definition of the auxiliary variable X , we obtain the expression for the variation equivalent to the one in equation 4.24. We again separate the contributions of the hopping and diagonal terms, and obtain

$$\delta S_{PF_2} = - \left(Y^\dagger \begin{bmatrix} 0 & \delta\{Q_{eo}\} \\ \delta\{Q_{oe}\} & 0 \end{bmatrix} X + Z^\dagger \begin{bmatrix} \delta\{Q_{ee}\} & 0 \\ 0 & \delta\{Q_{oo}\} \end{bmatrix} X \right) + H.c., \quad (4.48)$$

where X and Y are those from equation 4.47 and Z is again obtained from Y , keeping in mind that ϕ_2 , as well as ϕ_e in the previous section, is defined only on even points

$$Z = \begin{bmatrix} Y_e - \phi_2 \\ Y_o \end{bmatrix} = Y - \Phi, \quad \Phi = \begin{bmatrix} \phi_2 \\ 0 \end{bmatrix}. \quad (4.49)$$

The variation of the first part of the pseudofermion action also requires some more modifications with respect to the single pseudofermion case. Therefore, we write here all steps of its derivation

$$\begin{aligned} \delta S_{PF_1} &= \phi_1^\dagger \delta\{W^{\dagger-1} W^{-1}\} \phi_1 \\ &= \phi_1^\dagger \{W^{\dagger-1} \delta\{W^{-1}\} + H.c.\} \phi_1 \\ &= \phi_1^\dagger \{ \{W^{-1}\}^\dagger \delta\{P_e \tilde{Q}^{-1} Q_{ee} P_e\} + H.c.\} \phi_1 \\ &= \phi_1^\dagger [\{P_e \tilde{Q}^{-1} Q_{ee} P_e\}^\dagger P_e \delta\{\tilde{Q}^{-1} Q_{ee}\} P_e + H.c.] \phi_1 \\ &= \phi_{1e}^\dagger [\{P_e \tilde{Q}^{-1} Q_{ee}\}^\dagger (-\tilde{Q}^{-1} \delta\{\tilde{Q}\} \tilde{Q}^{-1} Q_{ee} + \tilde{Q}^{-1} \delta Q_{ee}) + H.c.] \phi_{1e} \\ &= \phi_{1e}^\dagger [Q_{ee} \tilde{Q}^{-1\dagger} P_e (-\tilde{Q}^{-1} \delta\{\tilde{Q}\} \tilde{Q}^{-1} Q_{ee} + \tilde{Q}^{-1} \delta Q_{ee}) + H.c.] \phi_{1e} \end{aligned} \quad (4.50)$$

The formula we used for inverse W^{-1} is derived in appendix 3, where the construction of the auxiliary operator \tilde{Q} is also explained. In order to write this variation in the form of equation 4.48, let us first note that the variables X and Y can be defined in the same way as in the case of a single pseudofermion, the only difference being that Q^{-1} is replaced by \tilde{Q}^{-1}

$$\begin{aligned} X &= \rho \tilde{Q}^{-1} P_e Q^{-1} Q_{ee} \phi_{1e} \\ Y &= \tilde{Q}^{-1} Q_{ee} \phi_{1e}. \end{aligned} \quad (4.51)$$

In order to get the form of variable Z , let us write once more the equation 4.50

4 MP-HMC program package

with the X and Y variables inserted

$$\delta S_{PF_1} = -(X^\dagger \begin{bmatrix} 0 & \delta\{Q_{eo}\} \\ \delta\{Q_{oe}\} & 0 \end{bmatrix} Y + X^\dagger \begin{bmatrix} \delta\{(1+\rho)Q_{ee}\} & 0 \\ 0 & \delta\{Q_{oo}\} \end{bmatrix} Y \quad (4.52)$$

$$+ X^\dagger \begin{bmatrix} \delta\{Q_{ee}\} & 0 \\ 0 & 0 \end{bmatrix} \phi_{1e}) + H.c. \quad (4.53)$$

One can easily see that the new definition of Z is

$$Z = \begin{bmatrix} (1+\rho)Y_e - \phi_2 \\ Y_o \end{bmatrix}. \quad (4.54)$$

Having derived the expressions for X, Y and Z , we can proceed to compute the separate contributions to the force corresponding to each part of the fermion action. This is done in a fashion similar to what was done for a single pseudofermion case.

4.2.2 HMC stability and safety measures

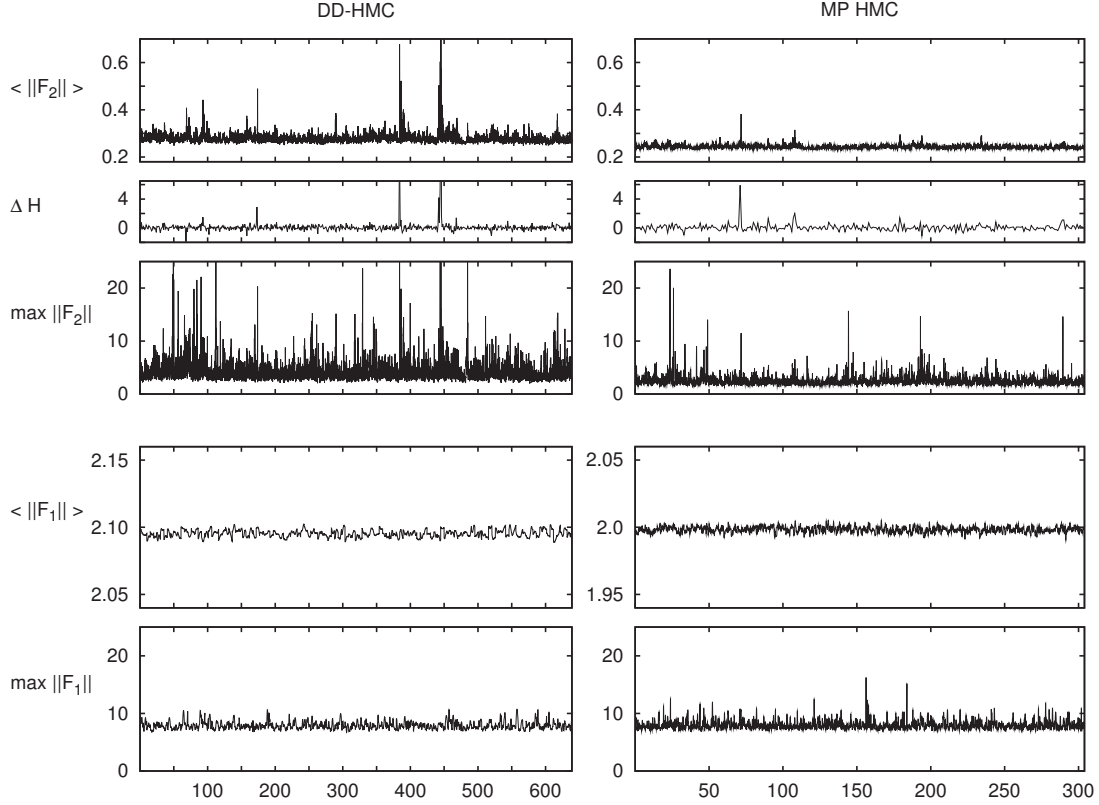


Figure 4.4: Histories of the energy violation ΔH , together with the maximum and average forces F_2 and F_1 , for each force update, plotted as a function of the trajectory number. Values obtained with the DD-HMC algorithm are shown to the left and the integration step-sizes for the two forces relate as $\Delta t_2 : \Delta t_1 = 1 : 6$. The values for MP-HMC are shown in the two right panels and the corresponding ratio of the integration steps is $\Delta t_1 : \Delta t_2 = 1 : 10$. The lattice size is 48×24^3 and $\kappa_{\text{sea}} = 0.13625$, corresponding to the pion mass 450MeV. In all the above plots, neither the *replay trick* in DD-HMC nor the *force cut* in MP-HMC was applied. The author has published this figure previously in [74].

HMC simulations of QCD with Wilson fermions suffer from occasional large forces during the MD trajectories. The reason for this is the potentially unstable numerical integration of the equations of motion in the MD procedure. The instability manifests through a large value of the force magnitude on a single link, sometimes even of order $\mathcal{O}(10^4)$, and the integrators become unstable at that point in the MD trajectory. Normally, large energy violation at the end of the trajectory (ΔH) then leads to the rejection of the new field configuration. The

4 MP-HMC program package

way to avoid these instabilities is to make the integration step size exceedingly small that makes the simulation very expensive. In Figure 4.4 we show the energy violations in a typical DD- and MP-HMC simulation (without any safety measure applied), together with the maximum and average forces in both algorithms. We see that large magnitudes of the IR force (F_2) occasionally appear in both algorithms. For the particular choice of the quark mass and the lattice spacing illustrated in Figure 4.4, despite the occasional bumps in the energy violation, the simulation still gives a correct distribution. On the other hand, going e.g. to smaller lattice spacings requires additional measures of precaution. In the DD-

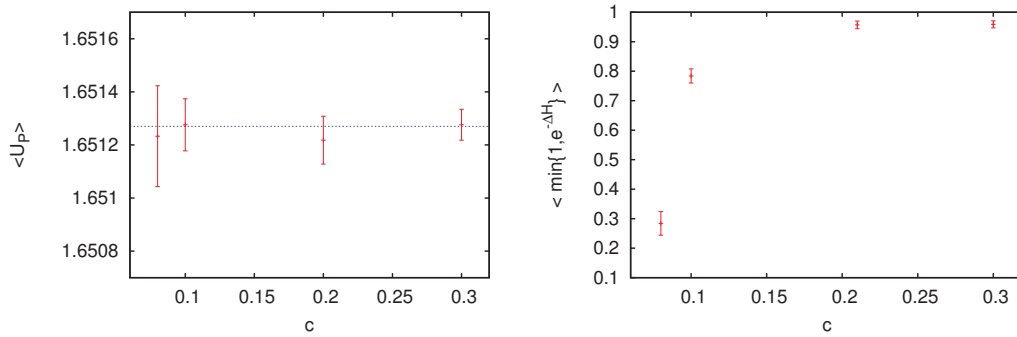


Figure 4.5: Average plaquette (left panel) and the theoretical acceptance (right panel) for different values of the cut parameter c on the 48×24^3 lattice and $\kappa_{\text{sea}} = 0.13625$, corresponding to the pion mass 450MeV. The dashed blue line in the left panel denotes the average plaquette with no cut of the forces introduced which corresponds to the value of the cut parameter $c \rightarrow \infty$. In the right panel we plot the theoretical acceptance $P_{acc}^{th} = \min\{1, e^{-\Delta H}\}$, which is a good estimate of the real acceptance on a small number of configurations ($N_{cf} < 100$).

HMC it was possible to turn on the so called *replay trick* and repeat with a smaller step size the trajectory where the instability would occur [68]. In MP-HMC we include a different safety measure, proposed in [82]. Namely, we regularize the MD force with the following modification

$$F_i^R(U) = \frac{\partial S_i}{\partial U} \times R(\delta t \left| \frac{\partial S_i}{\partial U} \right| / c) \quad (4.55)$$

where S_i represents the action corresponding to the regulated force F_i and c is the cutoff parameter that can be set in the input file of MP-HMC. Our choice of the

cutoff function reads

$$R(x) = \begin{cases} 1 & \text{at } x < 1/2 \\ \frac{1}{x}(1 - \frac{1}{2}e^{-(2x-1)}) & \text{at } x \geq 1/2. \end{cases} \quad (4.56)$$

The regularized force $F^R(U)$ depends only on U , therefore reversibility is guaranteed and thus the detailed balance is fulfilled. With an adequate choice of the cutoff parameter c as well as other algorithm parameters, the modification (eq. 4.56) has no effect on the acceptance rate. On the other hand, it allows the trajectory where the instability occurs to come to an end in a situation where the program without this safety measure would possibly crash. This modification is constructed such that the algorithm satisfies the detailed balance. We illustrate in Figure 4.5 that the plaquette average remains correct when varying the cut parameter c (left panel). What depends on the cut parameter c is the overall acceptance rate (right panel of Figure 4.5). If c is chosen to be small ($c \leq 0.1$), then a significant amount of links gets modified by the cut and this makes the acceptance drop below 50%. Within the errorbars (which get large due to the decreased acceptance), the average plaquette still agrees with the plaquette with no introduced cut.

Let us note here that, as long as the reversibility of the MD integration is not compromised, the above mentioned instabilities do not invalidate the algorithm of choice. On the other hand, they may affect the efficiency of the simulation (the acceptance rate is lowered, cf. Figure 4.5). This is true in general, but in all our runs we have chosen the value $c = 5.0$ which modifies links in small fraction of trajectories and does not affect the acceptance at all - only the trajectories for which the integrator would be inaccurate in any case are modified.

4.3 Performance

In this section we test the speed and the scaling of our implementation of the mass preconditioned HMC algorithm. We then confront MP-HMC to DD-HMC in two realistic simulation parameter sets with intermediate quark masses and relatively large lattice sizes. Finally, we give a summary of the long chains of large scale simulations performed with the MP-HMC program package.

4.3.1 Timings and scaling of the MP-HMC package

A good part of the motivation for developing the MP-HMC package was to apply it in the runs with a large number of processors. For optimal usage of the available computational resources, a good scaling of the code is required. We check

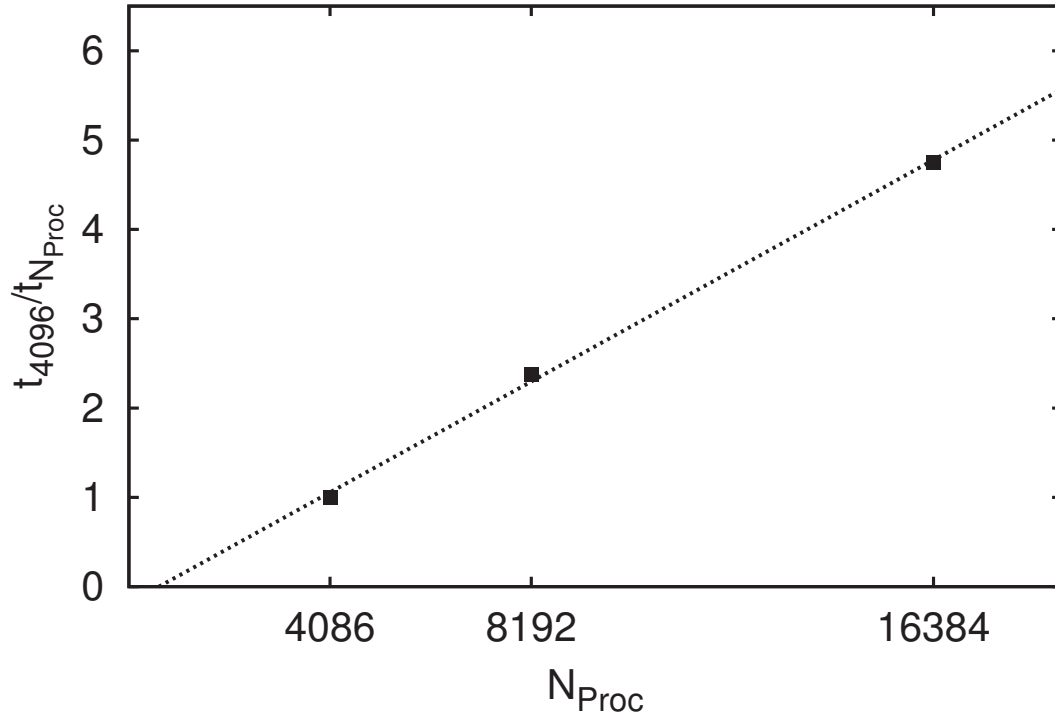


Figure 4.6: Inverse time needed for a single trajectory in MP-HMC versus the number of processors used. The trajectory length in all our runs is set to be 2 molecular dynamics units. The lattice size for the given test is 128×64^3 , denoted as O7 in Table 4.3. The chosen set of run parameters corresponds to the pion mass of the 270MeV and the lattice spacing in physical units of 0.05fm. The measured time is given in units of time per trajectory for 1 Rack (4096 cores) on the supercomputer JUGENE (Jülicher BlueGeneP).

4.3 Performance

the scaling of the code on one of our most difficult sets of parameters (O7 lattice, see Table 4.3). The result is shown in figure 4.6 and we observe here a very good, almost linear scaling of the code for the values of processors up to sixteen thousand. The costs of various computations during the MD trajectory are broken down in Table 4.1. The largest fraction of time during the MD trajectory is spent in the computation of fermion forces (cf. Table 4.1).

4 MP-HMC program package

Time/traj	4261.5s
F_3	31%
F_2	26%
F_1	38%
$\sum F_i$	95%
accept-reject	0.5%
other	4%

Table 4.1: Distribution of the total time of a single MP-HMC trajectory into different types of computation. The first two contributions contain inversions, therefore the largest fraction of time is spent here. The shown timings correspond to the O7 lattice (cf. Table 4.3) which was simulated with $N_{\text{PF}} = 3$ pseudofermions and the computation of their forces uses up the most of the simulation time. F_3 denotes the force of the sea quark, and F_2 and F_1 are the preconditioning forces.

4.3.2 Comparison of DD-HMC and MP-HMC

As we have already noted in Ref. [74], comparison between algorithms is in general a tedious task. The number of parameters that have to be set in modern lattice QCD simulations can go into the dozens. The optimal values of these parameters depend on each other and therefore it is virtually impossible to find the minimum at which each algorithm performs best and then make a true comparison. In particular, the performance is determined by the autocorrelation times of the observables of interest, whose measurements require runs with high statistics.

Domain decomposed and mass preconditioned HMC algorithms have been compared in [62], however, new to our study is the use of the deflated solver in both algorithms. The first comparison of the MP-HMC with the DD-HMC algorithm is done on the D5 lattice of size 48×24^3 with the corresponding lattice spacing of $a \approx 0.07\text{fm}$ and the pion mass of $m_\pi \approx 400\text{MeV}$. The summary of these results is shown in Table 4.2 and it is based on the results published in Ref. [74]. After the presented test with two pseudofermions ($N_{\text{PF}} = 2$) proved successful, we also implemented the mass preconditioner with one more pseudofermion pair. The $N_{\text{PF}} = 3$ case turned out to be even more advantageous for the simulation of large lattices with small quark masses, moving closer to the physical point.

In the simulation at the pion mass of 270MeV (O7 lattice, 128×64^3) for the lattice spacing of only $a \approx 0.05\text{fm}$ after suitable tuning of the mass preconditioning, the gain of MP-HMC over DD-HMC is roughly 4 times, again in the sense that MP-HMC produces the same error 4 times faster on the measured observable U_p using the same number of CPUs. A part of this gain was achieved by replacing

4.3 Performance

	time(64Core h.)/R	U_P	$\tau_{int}(U_P) \times R$	N_{traj}	P_{acc}
DD-HMC (D5)	0.56	1.65106(10)	10(5)	840	89%
MP HMC (D5)	0.43	1.65127(10)	10(4)	432	85%
DD-HMC (O7)	1112	1.719094(15)	14(6)	1250	84.8%
MP HMC (O7)	279.5	1.719104(5)	7(2)	1960	82.9%

Table 4.2: Comparison of the mass preconditioned version of the HMC algorithm with DD-HMC. Both simulations are done for the improved Wilson theory with two degenerate fermion flavors. The size of the lattice D5 is 48×24^3 , lattice spacing $a \approx 0.07\text{fm}$ and the pion mass $m_\pi \approx 400\text{MeV}$. The block size in DD-HMC is $6^2 \times 12^2$, while in the case of MP-HMC, the preconditioning pseudofermion mass is $m_1 \approx 8.5m_{\text{sea}}$. Here R represents the fraction of active links in the algorithm, $R = 0.37$ for DD-HMC and $R = 1$ for MP-HMC. The size of the lattice O7 is 128×64^3 , lattice spacing $a \approx 0.05\text{fm}$ and the pion mass $m_\pi \approx 270\text{ MeV}$. The block size in DD-HMC is 8^4 , while in the MP case, the preconditioning pseudofermion masses ($N_{\text{PF}} = 3$) are $m_2 \approx 2.5m_{\text{sea}}$, $m_1 \approx 27.1m_{\text{sea}}$. $R = 0.36$ for DD-HMC and $R = 1$ for MP-HMC.

the standard leapfrog integration scheme by the Omelyan integrator discussed in section 3.5.2. Apart from the fact that the new algorithm is faster and stable, an important advantage is that in the runs with the new implementation, we are able to use several times as many processors than was possible with DD-HMC, due to the constraints discussed in section 4.1. Hence, with our algorithmic and implementation choices, we have gained additional flexibility to exploit the power of today's massive parallel computers in order to get the statistics needed for attacking interesting physics problems in a significantly shorter period of time.

4.3.3 Large scale simulations with MP-HMC

We have seen so far that MP-HMC is a very efficient code for simulating improved Wilson fermions. As already mentioned, this is largely due to the highly efficient deflated solver from DD-HMC. The additional improvements and larger freedom in the choice of preconditioning parameters allow us to obtain the same acceptance with a smaller number of integration steps in the molecular dynamics trajectory of a fixed length, than needed in DD-HMC. On top of this, the MP-HMC has looser constraints over the maximal number of processors that can be used in the simulation. Also, in DD-HMC, only a fraction of links is updated during a MD trajectory, while in MP-HMC all links are updated, which manifests through smaller autocorrelation times. All this makes MP-HMC favorable for simulations with the quark masses towards the physical point, where the lattice

4 MP-HMC program package

id	L/a	β	κ	$m_\pi[\text{MeV}]$	$m_\pi L$
A5	32	5.2	0.13594	330	4.0
G8	64	5.3	0.13642	192	4.1
N6	48	5.5	0.13667	340	4.0
O7	64	5.5	0.13671	270	4.2

Table 4.3: Overview of the ensembles generated with MP-HMC. We give the label, the spatial extent of the lattice, $\beta = 6/g_0^2$, the hopping parameter κ of the sea quarks, the mass of the sea pion m_π and the product $m_\pi L$, which has to be larger than or equal to 4 to avoid finite volume effects. All lattices have the dimension $T \times L^3$ with $T = 2L$.

sizes need to be large to keep finite volume effects under control.

The summary of all our simulations performed with MP-HMC is given in Tables 4.3 and 4.4. Table 4.3 contains the general parameter sets that characterize a simulation point in a physical phase space and are independent from the simulation algorithm (lattice size, bare gauge coupling, hopping parameter of the sea quarks), as well as the estimated pion mass. The length of the MD trajectory is set to $\tau = 2.0$ in all MP-HMC runs. The integration step numbers $N_i = 1 \dots N_{\text{NPF}}$ are set to the values given in Table 4.4. Beside these HMC parameters, we also give in Table 4.4 the number of processors, the total number of MD units that has been simulated and the achieved acceptance rate in each of these runs. The successful production of the ensembles given above for $N_f = 2$ improved Wilson fermions was a crucial ingredient for obtaining the final result of the strange quark mass and Lambda parameter in $N_f = 2$ QCD, which will be presented in chapter 7.

id	N_0	N_1	N_2	N_3	N_4	N_5	N_{proc}	acc. rate	MDU
A5	2	9	1	32	-	-	512	0.92	2860
G8	18	1	1	1	1	23	16384	0.80	1100
N6	2	9	1	16	-	-	2048	0.84	4000
O7	2	9	1	16	-	-	16384	0.83	4000

Table 4.4: Overview of the HMC parameters, the number of processors used in the simulations, the achieved acceptance and the total number of MDU in the produced ensembles. The number of pseudofermion pairs used in the simulation vary from $N_{\text{PF}} = 3$ to $N_{\text{PF}} = 5$ and we give here the number of integration steps for each of them.

5 Schrödinger Functional

The standard continuum formulation of quantum field theories takes place in infinite volume. We have seen in Chapter 2 how the corresponding discretized theory can be formulated on the lattice introducing (anti-)periodic boundary conditions in space and time. An alternative approach would be to define QCD in a finite volume and choose the boundary conditions convenient for both perturbative calculations and preferably inexpensive MC simulations. The Schrödinger functional (SF) boundary conditions, which will be discussed in the following, provide this amenity. The Schrödinger representation of quantum field theory was considered to be non-renormalizable, until the existence of the Schrödinger picture in renormalizable quantum field theories was proven by Symanzik [83]. The studies of the scale transformations in asymptotically free theories with boundaries by Wolff [84, 85] lead to the idea of utilizing finite-size scaling method to compute the running coupling in a lattice regularized theory[22]. After the computation of the coupling in the pure gauge theory has been completed, the same method was used by the ALPHA collaboration to compute the running coupling and mass in $N_f = 2$, as well as the running coupling in $N_f = 4$ theory [19–21]. In this chapter we outline the importance of non-perturbative renormalization and then proceed to the lattice formulation of the SF which is applied throughout this work. The SF formulation is advantageous in various applications that will not be covered here, such as the Heavy quark effective theory, Chirally rotated SF etc. For reviews on the Schrödinger functional renormalization scheme and its applications see for example [86–89].

5.1 Non-perturbative renormalization

As it was outlined in chapter 1, QCD is theory described in terms of few parameters, namely the strong coupling constant α_s and the masses of the quarks. Like all other coupling constants in the Standard Model, α_s also depends on the energy transfer μ in the interaction process. At energy scales of $\mu \approx 10\text{GeV}$ or higher, the perturbative method for the determination of the coupling constant of the theory still works well. When addressing lower energy scales, e.g. $\mu \approx 1\text{GeV}$, the QCD coupling constant becomes so large that perturbation theory becomes unreliable. Obviously, this brings us to the need for non-perturbative methods that would allow us to deal with the large values of α_s and to work out the predictions of

5 Schrödinger Functional

QCD in this situation. Before making the predictions for experimental observables, the coupling, masses and fields have to be renormalized. In order to perform a completely non-perturbative study of QCD, the renormalization also has to be performed non-perturbatively. To achieve a determination of the QCD parameters in one non-perturbatively well-defined renormalization scheme at large scales ($\mu \gtrsim 10 \text{ GeV}$ - in order to connect to the perturbation theory results in a controlled manner), several other criteria have to be fulfilled. First, the scale μ has to be remote from the lattice cutoff a^{-1} to avoid large discretization errors and to be able to extrapolate to the continuum limit. Another requirement for some part of the simulations is to keep the box size L large compared to the relevant correlation length in the system, in this case the confinement scale and the mass of the lightest physical state (mass of the pion, m_π). These requirements summarized give the following hierarchy of scales

$$L \gg \frac{1}{m_\pi} \sim \frac{1}{0.14\text{GeV}} \gg \frac{1}{\mu} \sim \frac{1}{10\text{GeV}} \gg a. \quad (5.1)$$

The scales from the above inequalities would have to be well-separated in the lattice QCD simulations. There are several strategies for non-perturbative renormalization and most of them assume that the mentioned relevant physical scales can all be accommodated on a single lattice. The size of that lattice should be sufficiently small for the required calculations to be performed using numerical simulations with currently available computational resources. If this is the case, then the energy range where the low energy (non-perturbative) scheme can be matched to perturbation theory is rather narrow and, in this approach, systematic errors are not easy to control.

This difficulty can be overcome [22] by simulating a sequence of lattices where any single lattice covers only a limited range of energy scales, but through the use of the finite-volume renormalization scheme it is possible to match subsequent lattices. In this way, in a few steps one is able to reach the energies high enough to compare with perturbation theory, with complete control over systematic errors. The technique for achieving this is the finite size scaling in combination with the Schrödinger functional renormalization scheme and we will directly proceed to the definition of the later in the discretized theory.

5.2 SF Renormalization Scheme

The Schrodinger functional is the Euclidean propagation kernel of a field configuration C at time $x_0 = 0$ to some other configuration C' at time $x_0 = T$. In the

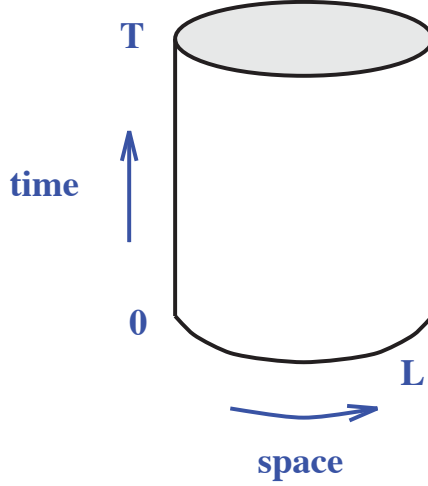


Figure 5.1: Illustration of the Schrödinger functional (SF) space-time manifold. The time direction is finite imposing Dirichlet boundary conditions on the boundary and all three spatial directions have periodic boundary conditions. In case that the matter fields are included, the periodicity in the spacial direction holds up to the phase angle θ (see eq. 5.5).

lattice formulation of the theory, it corresponds to the partition function

$$Z[C, C'] = \int D[\bar{\psi}]D[\psi]D[U]e^{-S[\bar{\psi}, \psi, U]}, \quad (5.2)$$

defined on a four dimensional Euclidean hypercubic lattice of volume $T \times L^3$, $x_\mu = an_\mu$, $n_k = 0, \dots, L-1$, $n_0 = 0, 1, \dots, T$, with a lattice spacing a and with the following conditions on matter and gauge fields.

1. In the spatial directions, periodic boundary conditions are imposed on the gluon fields

$$U_k(x + L\hat{k}/a) = U_k(x). \quad (5.3)$$

On the other hand, the periodicity of quark fields in spatial directions is generalized and they are defined to be periodic up to a phase factor

$$\psi(x + L\hat{k}/a) = e^{i\theta_k} \psi(x), \quad (5.4)$$

$$\bar{\psi}(x + L\hat{k}/a) = e^{-i\theta_k} \bar{\psi}(x). \quad (5.5)$$

2. At time $x_0 = 0$ and $x_0 = T$ the fields are required to satisfy Dirichlet boundary conditions. In the following applications, they are chosen to be homogeneous, except for the spatial components of the vector potentials A_k that

5 Schrödinger Functional

correspond to the classical (chromoelectric) gauge potentials C and C' . The spatial gauge links on the boundaries then take values

$$U_k(x) = \begin{cases} e^{aC_k(x)} & \text{at } x = 0, \\ e^{aC'_k(x)} & \text{at } x = T. \end{cases} \quad (5.6)$$

The fermion fields on the boundary are fixed to some externally given fermion fields $\rho(x), \rho'(x)$ and their conjugates, according to

$$P_+ \psi(x)|_{x_0=0} = \rho(x), \quad P_- \psi(x)|_{x_0=T} = \rho'(x), \quad (5.7)$$

$$\bar{\psi}(x)P_-|_{x_0=0} = \bar{\rho}(x), \quad \bar{\psi}(x)P_+|_{x_0=T} = \bar{\rho}'(x), \quad (5.8)$$

with P_{\pm} being the projection operators $P_{\pm} = (1 \pm \gamma_0)/2$.

The described choice of the boundary conditions type defines the space-time manifold of a four dimensional cylinder. The illustration of the Schrödinger functional geometry is given in Figure 5.1.

Let us for a while consider $SU(3)$ gauge theory, and a gauge action as a function of the gauge fields A . The smooth classical gauge fields C and C' take values in $su(3)$ algebra and they effect an absolute minimum of the action $S_G[A]$. Namely, if C and C' are small, a unique (up to gauge transformation Ω , defined for all lattice points x in the SF cylinder and its boundary) classical solution of the equations of motion $B_{\mu}(x)$ should exist, such that

$$S_G[B] < S_G[A], \quad \forall A \neq B^{\Omega}. \quad (5.9)$$

The field B which satisfies eq. (5.9) is called the induced background field. The boundary field B , as a unique configuration of minimal action dominates the functional integral in the weak coupling regime. Therefore, we can expand the Schrödinger functional effective action (free energy) around the background field B

$$\Gamma[B] \equiv -\ln Z[C, C'] = \frac{1}{g_0^2} \Gamma_0[B] + \Gamma_1[B] + g_0^2 \Gamma_2[B] + \dots, \quad (5.10)$$

$$\Gamma_0[B] \equiv g_0^2 S[B]. \quad (5.11)$$

The above series expansion of the effective action is regulated by a lattice cutoff a and, as it has already been discussed many times, the finiteness of the lattice spacing a always introduces discretization errors. In principle, the choice of the boundary fields C and C' is arbitrary, but a specific one could be used to reduce the lattice artifacts for the observable of interest. In the following we continue the above discussion for the pure gauge and introduce the Schrödinger functional

formulation of the running coupling.

5.3 Renormalized coupling

To overcome the scale problem discussed in section 5.1, we define a non-perturbative renormalized coupling $\bar{g}^2(\mu)$ such that it depends only on one scale. We parametrize the product of the background field and the lattice size ($B \times L$) with the dimensionless variable η . This corresponds to imposing the scaling $1/L$ of the strength of the background field B , which is defined such that it has to satisfy conditions 1. and 2. of section 5.2. The existence of a background field configuration that fulfills these conditions is demonstrated in Ref. [90]. The authors of [90] also give the choice of constant Abelian fields which provides us with tolerable lattice corrections to the effective action for the $SU(3)$ gauge group

$$C_k = \frac{i}{L} \begin{pmatrix} \phi_1 & 0 & 0 \\ 0 & \phi_2 & 0 \\ 0 & 0 & \phi_3 \end{pmatrix}, C'_k = \frac{i}{L} \begin{pmatrix} \phi'_1 & 0 & 0 \\ 0 & \phi'_2 & 0 \\ 0 & 0 & \phi'_3 \end{pmatrix}, \quad (5.12)$$

where

$$\phi_1 = \eta - \frac{\pi}{3}, \quad \phi'_1 = -\phi_1 - \frac{4\pi}{3}, \quad (5.13)$$

$$\phi_2 = -\frac{1}{2}\eta, \quad \phi'_2 = -\phi_3 + \frac{2\pi}{3}, \quad (5.14)$$

$$\phi_3 = -\frac{1}{2}\eta + \frac{\pi}{3}, \quad \phi'_3 = -\phi_2 + \frac{2\pi}{3}. \quad (5.15)$$

The renormalized coupling in the SF scheme can now be defined as the response of the system to an infinitesimal variation of this specific one-parameter family of prescribed constant abelian boundary fields

$$\Gamma' = \frac{\partial \Gamma[B]}{\partial \eta} \propto \frac{1}{\bar{g}^2}. \quad (5.16)$$

The derivative from eq. 5.16 is defined non-perturbatively and at the same time it is finite when expressed in terms of a renormalized coupling from some perturbative renormalization scheme (for example $\bar{g}_{\overline{MS}}$). Therefore, after normalization we arrive at the fully non-perturbative definition of the running coupling that runs only with the system size L

$$\bar{g}^2(L) = \frac{\partial \Gamma_0[B]}{\partial \eta} / \frac{\partial \Gamma[B]}{\partial \eta}. \quad (5.17)$$

5 Schrödinger Functional

The argumentation from sections 5.1 - 5.3 has been carried over to the theory with dynamical fermion degrees of freedom in Ref. [91] and a similar definition of the renormalized SF coupling is obtained for the full QCD

$$\bar{g}^2(L) = \frac{\partial \Gamma_0[B]}{\partial \eta} / \frac{\partial \Gamma[B]}{\partial \eta}, \quad (5.18)$$

$$= k \left(\left\langle \frac{dS_g}{d\eta} \right\rangle^{-1} + \left\langle \frac{dS_{\text{eff}}}{d\eta} \right\rangle^{-1} \right). \quad (5.19)$$

The eq. 5.19 holds since the derivative $\partial \Gamma / \partial \eta$ is an expectation value of some combination of the gauge field variables close to the boundaries $\langle dS/d\eta \rangle$. With this in hand, the numerical calculation of \bar{g}^2 in a Monte Carlo simulation is straightforward, and it thereby also complies with the requirements discussed in section 5.1.

5.4 Step scaling function

We have previously defined the SF coupling $\bar{g}(L)$ such that it depends on a single renormalization scale L . The way to avoid the compromises needed for performing the renormalization non-perturbatively on a single lattice (cf. section 5.1) is to identify the two relevant physical scales in the condition 5.1, namely to set

$$\mu = 1/L. \quad (5.20)$$

In this way, if one wants to obtain the energy dependence of the SF coupling, one may as well just vary the size of the finite-volume system. This dependence is attained by applying a special recursive technique which will be outlined here. We start by defining a quantity, $\sigma(u, s)$, which captures the change of the coupling when the finite box size L is scaled by a factor s

$$\sigma(u, s) \equiv \bar{g}^2(sL) |_{\bar{g}^2(L)=u}. \quad (5.21)$$

This quantity will, in the following, be referred to as the *step scaling function* (SSF). The common choice for the scaling factor is $s = 2$ and from now on we will accommodate the notation $\sigma(u, s = 2) = \sigma(u)$. The renormalization group equation in the continuum (eq. 2.46) indicates that a function that captures this change in the coupling after rescaling the physical size of the finite box exists. This function is exactly the SSF and in the case of interest ($s = 2$) it is obtained as a solution of a recursive equation

$$\bar{g}^2(2L) = \sigma(\bar{g}^2(L)). \quad (5.22)$$

5.5 The $O(a)$ improved Wilson action with SF boundary conditions

The connection of the SSF with the β -function of the renormalization group (eq. 2.47) can be expressed by the following integral

$$-2\ln(2) = \int_u^{\sigma(u)} \frac{dx}{\sqrt{x}\beta(\sqrt{x})}. \quad (5.23)$$

Using the asymptotic expansion of the β -function (eq. 2.50) we obtain the expansion of the step scaling function

$$\sigma(u) = u + s_0 u^2 + s_1 u^3 + s_2 u^4 + \dots, \quad (5.24)$$

$$s_0 = 2b_0 \ln(2), \quad (5.25)$$

$$s_1 = [2b_0 \ln(2)]^2 + 2b_1 \ln(2), \quad (5.26)$$

$$s_2 = [2b_0 \ln(2)]^3 + 10b_0 b_1 [\ln(2)]^2 + 2b_2 \ln(2), \quad (5.27)$$

valid for small values of the coupling $u = \bar{g}^2(L)$. With the definition of the running coupling in the SF scheme given in the previous section, the SSF can be easily (and to high precision) calculated on the lattice by numerical simulations. On a finite lattice, the SSF will have an additional dependence on the lattice resolution a/L and the continuum SSF is obtained by performing the scaling step ($L \rightarrow 2L$) at several different resolutions and performing the continuum extrapolation $a/L \rightarrow 0$. This procedure effectively constructs the so-called *non-perturbative renormalization group* and, although involved, in contrast to simpler approaches which typically compromise with the multiple scales handled on single lattices, it is more amenable to systematic improvement and error control. The details of extracting the continuum SSF from the lattice SSF will be discussed in chapter 6, where we apply the described procedure in the computation of the running coupling in QCD with $N_f = 4$ dynamical fermion flavors.

5.5 The $O(a)$ improved Wilson action with SF boundary conditions

The $O(a)$ improvement of the Wilson action with the gauge and fermion fields obeying the Schrödinger functional boundary conditions (see sec. 5.2) is obtained by a procedure similar to the one outlined in section 2.5. Since the time direction in SF formulation is treated specially, there are additional terms in both the gauge and the fermion part of the action that ensure that the $O(a)$ terms do not arise on the boundaries in time direction. Taking all this into consideration, the $O(a)$

5 Schrödinger Functional

improved Wilson gauge action now reads

$$S_W[U] = \beta \sum_P w(P) \left(1 - \frac{1}{3} \text{Re Tr } U_P\right), \quad (5.28)$$

where U_P and β , as in section 2.3, denote the product of the gauge links around the oriented plaquette P and the bare gauge coupling $\beta = 6/g_0^2$. The weight factors for the corresponding plaquettes $w(P)$ (introduced in Ref. [42]) are given by

$$w(P) = \begin{cases} 1 & U_P \text{ is the plaquette in the bulk,} \\ c_t(g_0) & U_P \text{ is the time-like touching } x_0 = 0 \text{ or } x_0 = T \text{ boundary,} \\ \frac{1}{2}c_s(g_0) & U_P \text{ is the space-like plaquette at } x_0 = 0, T. \end{cases}$$

The proper tuning of the parameters $c_t(g_0)$ and $c_s(g_0)$ gives the wanted cancellation of the discretization effects. As well as with the periodic boundary conditions, the $O(a)$ improvement of the Wilson fermion action in SF also requires an addition of the Sheikholeslami-Wohlert (*clover*) term (cf. eq. 2.37), which is now reduced to the bulk of the lattice. We write here the Sheikholeslami-Wohlert term with an explicit dependence on the lattice spacing a

$$S_{SW}[U, \psi, \bar{\psi}] = a^5 c_{SW} \sum_{x_0=a}^{x_0=T-a} \sum_{\mathbf{x}} \bar{\psi}(x) \frac{i}{4} \sigma_{\mu\nu} \hat{F}_{\mu\nu} \psi(x). \quad (5.29)$$

Additionally, in SF it is needed to add more counterterms in order to ensure the $O(a)$ improvement of the fermion action on the boundaries. We will denote this contribution to the fermion action as S_b and it is given by

$$\begin{aligned} S_b[U, \psi, \bar{\psi}] = \frac{a^4}{2} \sum_x \{ & (\tilde{c}_s - 1) [(\bar{\rho}(x) \gamma_k (\nabla_{\mathbf{k}}^* + \nabla_{\mathbf{k}}) \rho(x)) - (\bar{\rho}'(x) \gamma_k (\nabla_{\mathbf{k}}^* + \nabla_{\mathbf{k}}) \rho'(x))] \\ & + (\tilde{c}_t - 1) [(\bar{\psi}(x) (P_- \nabla_0 + P_+ \overleftarrow{\nabla}_0^*) \psi(x))_{x_0=a} \\ & - (\bar{\psi}(x) (P_- \nabla_0 + P_+ \overleftarrow{\nabla}_0^*) \psi(x))_{x_0=T-a}] \}. \end{aligned} \quad (5.30)$$

For the choice of constant boundary fields C, C' (eq. 5.12), the improvement term for the space-like plaquettes equals zero. Therefore, the computation of c_s is not needed. Setting the boundary quark fields $\rho(x), \rho'(x)$ to zero[91] has as a consequence that the terms which are multiplied with \tilde{c}_s also vanish and one is left only with terms multiplied with c_t and \tilde{c}_t . All that now remains is to tune non-perturbatively or to determine perturbatively the time-like boundary improvement coefficients for the formulation. We give here the perturbative expressions for these coefficients. The gauge action improvement coefficient c_t has been de-

5.6 Algorithmic challenges with SF formulation

terminated up to 2-loops [49], while the \tilde{c}_t has been determined up to 1-loop only, so far [92]

$$c_t(g_0) = 1 + (-0.08900(5) + 0.0191410(1)N_f)g_0^2 + (-0.0294(3) + 0.002(1)N_f + 0.0000(1)N_f^2)g_0^4 + O(g_0^6), \quad (5.31)$$

$$\tilde{c}_t(g_0) = 1 - 0.01795(2)g_0^2 + O(g_0^4). \quad (5.32)$$

Note that the amount of counterterms needed to cancel $O(a)$ effects also depends on the specific choice of boundary conditions in SF formulation. For example, one may define a modified (chirally rotated) boundary conditions in SF, as introduced in [93]. This formulation requires the tuning of an additional dimension 3 boundary counterterm for preserving the chirally rotated boundary conditions in the interacting theory. The theory we are using is simpler in that sense, since the number of boundary counterterms that have to be tuned is smaller. On the other hand, the mentioned alternative formulation of chirally rotated boundary conditions allows for automatic $O(a)$ improvement. Namely, unlike the standard SF formulation that we apply, the chirally rotated SF does not require the Sheikholeslami-Wohlert term or some other bulk $O(a)$ counterterms which are discussed in chapter 6. Additionally, this alternative formulation allows to perform checks of universality of the continuum limit of different observables in both formulations, which has to be unique.

5.6 Algorithmic challenges with SF formulation

We now move to some technical considerations with regard to incorporating the Schrödinger functional approach defined above into the lattice simulations. For previous studies of the SF with $N_f = 0, 2, 4$ flavors, the ALPHA collaboration performed the simulations using the GHMC¹ code. This code was written in the special high-level programming language TAO suitable for APE (Array Processing Experiment) [94] machines with SIMD (Single Instruction Multiple Data) architecture. The APE machines were developed in a joined project of DESY (Germany), INFN (Italy) and University Paris-Sud (France). The runs dedicated to the determination of the running coupling $N_f = 4$ massless quark flavors from Ref. [21, 95] were performed on APEmille and apeNEXT machines. One of the goals of this work was to improve this computation and determine more precisely the coupling for $N_f = 4$ flavors. In order to achieve this, it was necessary to develop a code which can be run on modern PC clusters and conventional supercomputers,

¹GHMC stands for the Generalized Hybrid Monte Carlo algorithm, implemented by the ALPHA collaboration in the programming language TAO and used on different APE machines in the period 1989-2011.

5 Schrödinger Functional

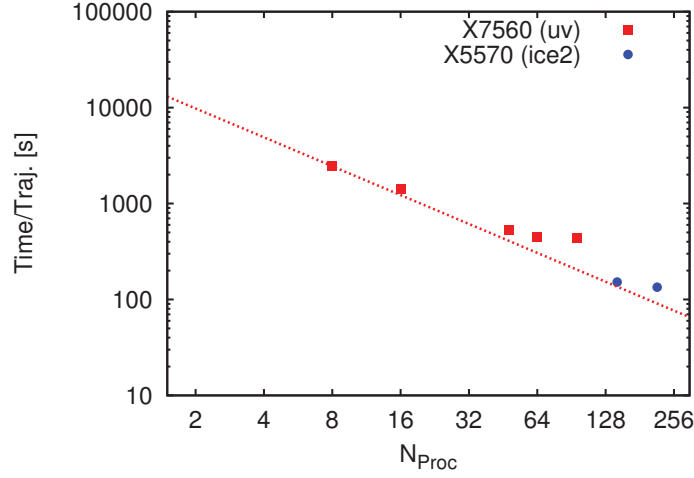


Figure 5.2: Scaling of the SF-MP-HMC code on a 24^4 lattice for $N_f = 2$ flavors of dynamical fermions. The tests are performed on a cluster of 8 core Intel machines with two types of processors: X7560 and X5570 (HLRN, ZiB Berlin). The background field is switched off.

since the development of the APE machines has been stopped and there were no existing computer resources in the world which could accommodate this computation.

5.6.1 Program package SF-MP-HMC: stability and scalability

We have developed a new code for Schrödinger functional simulations which is based on the mass preconditioned [65] Hybrid Monte Carlo algorithm and named it SF-MP-HMC. This implementation is based on the previously mentioned DD-HMC code of Martin Lüscher and our new implementation of the mass preconditioned HMC that was discussed in chapter 4. The new SF-MP-HMC code includes SSE inline-assembly optimization routines and SSE memory prefetch instructions, mainly based on the routines from DD-HMC and MP-HMC. The geometry and routines related to the Sheikholeslami-Wohlert term as well as the used Conjugate Gradient (CG) solver are taken from the new correlation function code of the ALPHA Collaboration[96].

For practical reasons, the code is parallelized only in three (spatial) directions. We first test the scalability of the SF-MP-HMC code starting from the thermalized $N_f = 2$ configurations of 24^4 lattices. This test is done in a setup without the background field, starting from the configurations and parameter sets obtained in the GHMC code studies of the quark mass renormalization from the Schroedinger

5.6 Algorithmic challenges with SF formulation

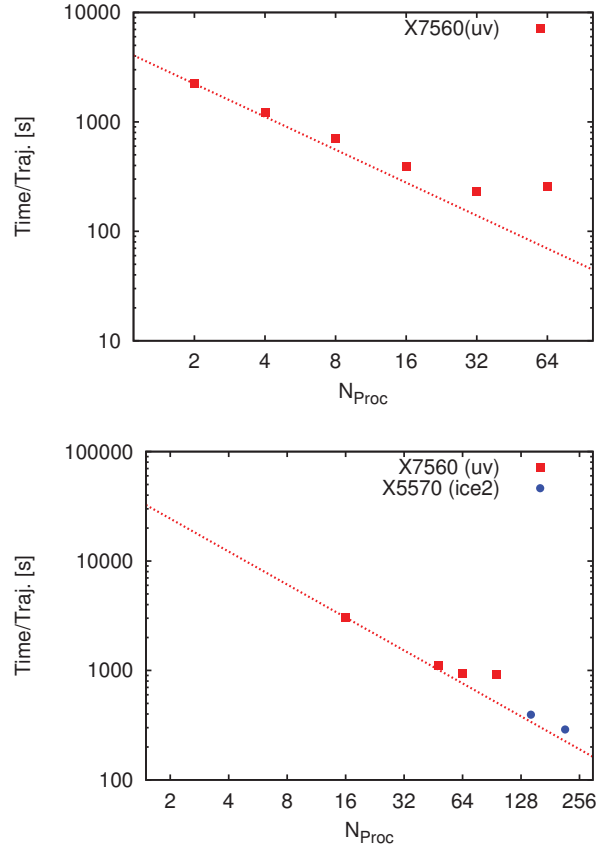


Figure 5.3: Scaling of the SF-MP-HMC code on a 16^4 lattice (up) and a 24^4 lattice (down) for $N_f = 4$ flavors of dynamical fermions. The tests are performed on the cluster of 8 core Intel machines with two types of processors: X7560 and X5570 (HLRN, ZiB Berlin). The background field given in eq. 5.12 for the computation of the coupling is switched on.

functional scheme [20]. The result of the test is shown in Figure 5.2. A very good scaling up to the maximal number of processors for this lattice size can be observed. The geometry needed for running on 96 processors has a very large surface to bulk ratio for the local lattices, therefore a more intensive communication overhead is observed and makes this choice of the number of processors not suitable for longer runs. Hence, optimal choice of the number of processors for this lattice size would be 128 or even 144. In Figure 5.3 we show the scaling of the code on 16^4 and 24^4 lattices with $N_f = 4$ flavors of massless quarks. Good scalability is also observed in these runs.

The Dirichlet boundary conditions imposed on the fermions in SF induce a finite gap in the spectrum of the Dirac operator and serve as a natural infrared

5 Schrödinger Functional

cutoff. Hence, the practical problems of simulating Wilson fermions on the lattice, such as the stability issues discussed in section 4.2.2, do not occur in the SF simulations we are performing² here. To illustrate that, we show in Figure 5.4 the history of the energy violation in a long chain of the simulation on a 24^4 lattice. Spikes similar to those from Figure 4.4 characterizing periodic boundary conditions with Wilson fermions are not present and the energy violation does not leave the range $\Delta H \in [-2, 2]$.

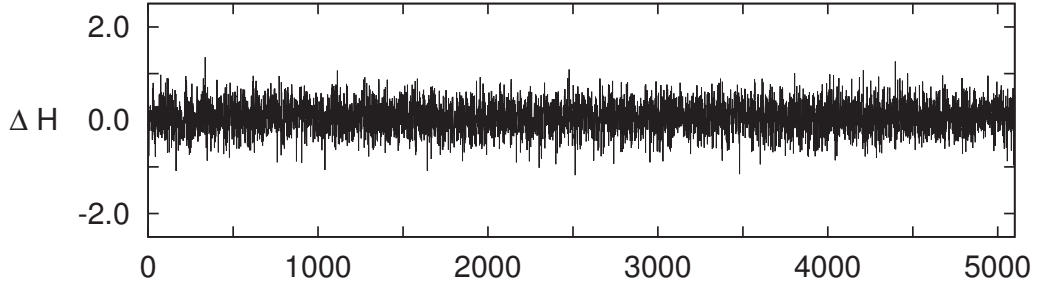


Figure 5.4: History of the energy violation ΔH in the SF-MP-HMC run on the 24^4 lattice(right). The plotted data correspond to roughly 5100 subsequent HMC trajectories of the length $\tau = 2.0$.

²The smallest eigenvalue for the free Dirac operator in SF, with vanishing boundary conditions, is $\lambda_{min}^2 = (\pi/2T)^2$. For the lattice sizes needed in SF simulations of the running coupling (up to $T = L = 24$) we are still protected with the discussed mass gap. Once the lattice size L reaches larger values, problems similar to those for light Wilson quarks on a periodic lattice may occur.

6 Running coupling in $N_f = 4$ theory

We have previously defined the step scaling function in continuum theory. It is also possible to define the lattice step scaling function that is dependent on the lattice resolution and equals the continuum SSF up to the cutoff effects. Here we describe the strategy for the computation of the step scaling function from lattice simulations in the theory with four dynamical fermion flavors. Due to the peculiarities in the SF formulation of the $O(a)$ improved Wilson theory, the way we chose different improvement coefficients has to be discussed. We review here the running coupling and the Lambda parameter results from Ref. [21, 95] and discuss the strategy for improving it. In order to achieve better precision than the authors of [21, 95], it is important to make sure that the quark mass is tuned to zero accordingly with the aimed improved accuracy. We derive the precision criteria to be fulfilled such that the only remaining dependence in the coupling is the one on the system size. After these criteria are fulfilled, we are confident that the systematic errors are negligible in comparison to the statistical ones and it is possible to proceed towards the precise computation of the running coupling for the $N_f = 4$ approximation of QCD. We then perform a continuum extrapolation and arrive to the continuum step scaling function. Finally, we give the value of the Lambda parameter of the theory in units of the system size.

6.1 Lattice step scaling function

To employ lattice simulations for the computation of the step scaling function (SSF) defined in section 5.4, one defines the discretized step scaling function $\Sigma(u, L/a)$, which has an additional dependence on the lattice resolution a/L

$$\Sigma(u, L/a) = \bar{g}^2(2L), \quad u = \bar{g}^2(L), \quad (6.1)$$

with bare coupling g_0 fixed, L/a fixed and vanishing quark mass $m = 0$. Let us recall that the boundary conditions for the fermions given in eq. 5.7 and 5.8 introduce a gap into the spectrum of the Dirac operator and allow for the Schrödinger functional lattice simulations to be performed for vanishing quark masses. We are hence able to supplement the definition of the running coupling by the requirement $m = 0$. Therefore, the lattice SSF also remains independent of the quark mass. The lattice SSF gives the continuum SSF as the lattice spacing is sent

6 Running coupling in $N_f=4$ theory

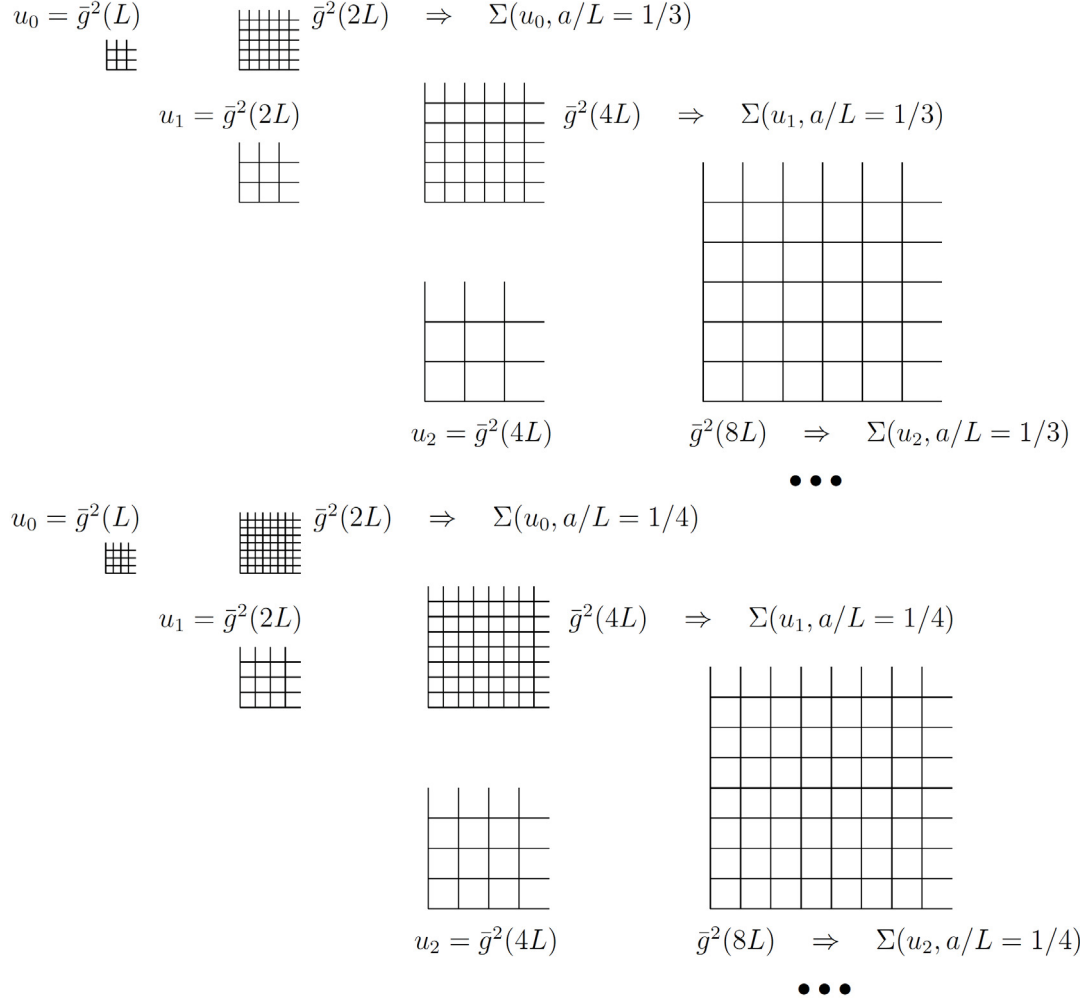


Figure 6.1: A sketch of the recursive finite-size scaling method used in the computation of the SF coupling \bar{g} at different energy scales $\mu = 1/L$. The evolution of the coupling with respect to energy is computed in several steps, changing μ by a factor of 2 in each of the steps. The steps of keeping a fixed lattice resolution a and increasing $L \rightarrow 2L$ (horizontal direction in the figure) are alternated with the steps of keeping the lattice extension L fixed and decreasing the a (vertical direction). In this way, the non-perturbative renormalization group (expression 6.3) is implemented, such that it is not necessary to have large ratios of the scales and therefore the discretization errors are already kept small for $L/a \gg 1$. Illustration is taken over from [97].

6.2 Motivation for precise computation of $N_f=4$ running coupling

to zero

$$\sigma(u) = \lim_{a \rightarrow 0} \Sigma(u, L/a), \quad u = \bar{g}^2(L). \quad (6.2)$$

In order to determine the function $\Sigma(u, L/a)$, the calculation for one rescaling step has to be performed at several different lattice resolutions, and finally the extrapolation $a/L \rightarrow 0$ is taken. In figure 6.1 (taken over from Ref. [97]) the described procedure for computing a sequence of lattice SSF is illustrated. By repeating the step in which the system size L is increased successively by a factor of 2, one gains full control over the continuum SSF $\sigma(u)$. Hence, one is able to reconstruct the non-perturbative renormalization group

$$\bar{g}^2(L) \rightarrow \bar{g}^2(2L) \rightarrow \bar{g}^2(2^2L) \rightarrow \dots \rightarrow \bar{g}^2(L_{\max} = 2^n L) \quad (6.3)$$

in n steps, over a wide range of energy scales.

As already mentioned, the chosen SF setup fulfills the requirement of separating the energy scale relevant for the running $\mu = 1/L$ from the lattice spacing a (see expression 5.1). Therefore, the sizes of the lattices that have to be simulated are of the order of $\mathcal{O}(10)$ and with the computer resources available nowadays it is easy to simulate these lattices with high precision.

6.2 Motivation for precise computation of $N_f = 4$ running coupling

The value of the strong coupling constant is not directly accessible in the experiment, but it is extracted from the experimental measurements by matching to perturbation theory (cf. Table 1.1). The quoted value is usually given in the $\overline{\text{MS}}$ renormalization scheme[15]. Note that $\alpha_{\overline{\text{MS}}}$ is in fact only perturbatively defined. Therefore, extracting the Λ parameter from the asymptotic region of $\alpha_{\overline{\text{MS}}}(\mu \rightarrow \infty)$ is a justified procedure at high energies. On the other hand, at a low renormalization scale, the truncation of the divergent perturbative series is not justified and a large theory error occurs in attempts to extract $\alpha_{\overline{\text{MS}}}(\mu)$ from the observables. As already outlined in chapter 1, different PT predictions for the value of the Lambda parameter in $N_f = 5$ theory differ in more than one sigma. It is therefore advantageous to apply the approach described in section 6.1 for connecting low and high energies and use the well-defined non-perturbative procedure to resolve this discrepancy.

Obtaining $\Lambda_{\overline{\text{MS}}}^{(5)}$ with the non-perturbative approach can be achieved in several

6 Running coupling in $N_f=4$ theory

independent steps. These can be summarized in the following formula[98]

$$\frac{\Lambda_{\overline{MS}}^{(5)}}{f_K} = \frac{1}{f_K L_{\max}} \times \frac{L_{\max}}{L_k} \Lambda_{\text{SF}}^{(4)} L_k \times \frac{\Lambda_{\overline{MS}}^{(4)}}{\Lambda_{\text{SF}}^{(4)}} \times \frac{\Lambda_{\overline{MS}}^{(5)}}{\Lambda_{\overline{MS}}^{(4)}}. \quad (6.4)$$

Let us explain briefly each part of this calculation.

1. First factor $1/f_K L_{\max}$ represents the typical hadronic scale at which we make contact with physical units, in this case determined by the kaon decay constant. L_{\max} is typically of the size 0.5fm. The determination of this term requires continuum extrapolation, therefore a large set of simulations is needed to perform this extrapolation in a well-controlled manner¹.
2. Second factor comes from the intermediate step of connecting low and high energies and yields the relation between $\alpha_{\text{SF}}(1/L_{\max})$ and $\alpha_{\text{SF}}(1/L_k)$, $L_k = 2^{-k} L_{\max}$, which is used to obtain $\Lambda_{\text{SF}}^{(4)} L_{\max}$ as a function of $\alpha_{\text{SF}}(1/L_k)$. L_{\max} is obtained fully non-perturbatively and the Λ_{SF} parameter is obtained by using the three-loop β -function in the SF scheme.
3. Third factor is known exactly, from 1-loop PT $\Lambda_{\overline{MS}}^{(4)}/\Lambda_{\text{SF}}^{(4)} = 2.9065$ [98, 99].
4. Following the strategy for decoupling across the b -threshold from Refs. [100, 101] we would finally obtain $\Lambda_{\overline{MS}}^{(5)}$. The expression for this last decoupling step is currently known to 4-loop in PT. Its estimated contribution to the uncertainty of the final result is about 2%[98].

This strategy allows for full control over the systematic uncertainties. The continuation of this chapter will present current progress towards completing the second term from the above strategy, namely the Lambda parameter for the four flavor theory, in units of the hadronic scale L_{\max} . Currently the computation done in [21] determines this term with the precision of 8%. Our goal was to improve this precision, in a controlled manner, by roughly a factor of two. In the continuation of this chapter, as well as in chapter 7, we will omit writing the index SF explicitly. Namely, from now on holds $\Lambda_{\text{SF}} \equiv \Lambda$.

6.3 Non-perturbative $O(a)$ improvement coefficients for $N_f = 4$ theory

In this work, we use Wilson fermions, which explicitly break chiral symmetry and this symmetry only emerges in the continuum limit. The systematic errors

¹The determination of this term in $N_f = 2$ theory will be addressed in section 7.2.

6.3 Non-perturbative $O(a)$ improvement coefficients for $N_f=4$ theory

associated with the finiteness of the lattice spacing a may be rather large and must be studied carefully. As it is already known, the lattice effects can be reduced in a controlled way by choosing an improved discretization of continuum theory (see section 2.5). We have seen in section 5.5 how the improvement was achieved for the Wilson fermion action with SF boundary conditions. In the massless SF theory, according to Ref. [42], it only remains to improve the local composite fields in order to achieve a complete cancellation of $O(a)$ effects in the correlation functions. Like in the previous work of the ALPHA Collaboration [17, 19–21, 102], the massless scheme is defined by setting the unrenormalized PCAC quark mass²

$$m(x_0) = \frac{\frac{1}{2}(\partial_0 + \partial_0^*)f_A(x_0) + c_A a \partial_0^* \partial_0 f_P(x_0)}{2f_P(x_0)} \quad (6.5)$$

at $x_0 = T/2$ to zero

$$m_1 = m\left(\frac{T}{2}\right) = 0. \quad (6.6)$$

In the above definition of $m(x_0)$, c_A denotes the improvement coefficient of the axial current that is a function of the bare coupling. The coefficient c_A is a subject of both perturbative and non-perturbative determination. In practice, the PCAC mass can vanish only approximately. The issue of tuning the PCAC mass to zero will be discussed in section 6.4.1, after we have decided on the exact definition of m_1 that will be used for this tuning, i.e. how we define c_A (see section 6.3.1). Following the notation of Ref.[43], we define the correlation functions f_A and f_P from eq. 6.5 as

$$f_A(x_0) = -a^6 \sum_{\mathbf{y}, \mathbf{z}} \frac{1}{3} \langle A_0^a(x) \bar{\rho}(\mathbf{y}) \gamma_5 \frac{1}{2} \tau^a \rho(\mathbf{z}) \rangle, \quad (6.7)$$

$$f_P(x_0) = -a^6 \sum_{\mathbf{y}, \mathbf{z}} \frac{1}{3} \langle P^a(x) \bar{\rho}(\mathbf{y}) \gamma_5 \frac{1}{2} \tau^a \rho(\mathbf{z}) \rangle, \quad (6.8)$$

where ρ and $\bar{\rho}$ denote the spatial component of the boundary quark fields³ at time $x_0 = 0$. The unimproved isovector axial current A_μ^a and the pseudo-scalar

²defined from the *partially conserved axial current* (PCAC) relation in a continuum:
 $\langle \partial_\mu f_{A\mu}^a(x) O^a \rangle = 2m \langle f_P^a(x) O^a \rangle$. For more details see [42].

³Note that in eqs. (5.7, 5.8), ρ and $\bar{\rho}'$ denote four-vector boundary fields, while here the notation is changed and ρ' are $\bar{\rho}$ spatial components of the boundary fields at the specified boundary timeslice, in this particular case $x_0 = 0$.

6 Running coupling in $N_f=4$ theory

density P^a are given by

$$A_\mu^a(x) = \bar{\psi}(x) \gamma_\mu \gamma_5 \frac{1}{2} \tau^a \psi(x), \quad (6.9)$$

$$P^a(x) = \bar{\psi}(x) \gamma_5 \frac{1}{2} \tau^a \psi(x). \quad (6.10)$$

One could also define the backward instead of forward correlation functions and they will be denoted by primed quantities

$$f'_A(T - x_0) = +a^6 \sum_{\mathbf{y}, \mathbf{z}} \frac{1}{3} \langle A_0^a(x) \bar{\rho}'(\mathbf{y}) \gamma_5 \frac{1}{2} \tau^a \rho'(\mathbf{z}) \rangle, \quad (6.11)$$

$$f'_P(T - x_0) = -a^6 \sum_{\mathbf{y}, \mathbf{z}} \frac{1}{3} \langle P^a(x) \bar{\rho}'(\mathbf{y}) \gamma_5 \frac{1}{2} \tau^a \rho'(\mathbf{z}) \rangle, \quad (6.12)$$

where $\rho'(\mathbf{y})$, $\bar{\rho}'(\mathbf{y})$, $\rho'(\mathbf{z})$, $\bar{\rho}'(\mathbf{z})$ again denote the spatial component of the boundary quark fields, but this time at the $x_0 = T$ boundary. The forward and backward correlation functions are related to each other, but they are, in general, not the same. Namely, under the time reflection the boundary fields C and C' are swapped and this is where the difference in the forward and backward quantities comes from.

6.3.1 Non-perturbative determination of c_A

In [21] the perturbation theory result for c_A was used, and it is only known to one loop. We explore in the following several alternative ways to define c_A and determine its effect in the tuning of the mass m_1 defined in eq. 6.6. Equation 6.5 can shortly be written as

$$m(x_0) = r(x_0) + c_A s(x_0), \quad (6.13)$$

where the auxiliary functions r and s are defined through

$$r(x_0) = \frac{\frac{1}{4}(\partial_0 + \partial_0^*) f_A(x_0)}{f_P(x_0)}, \quad (6.14)$$

$$s(x_0) = \frac{\frac{1}{2} a \partial_0^* \partial_0 f_P(x_0)}{f_P(x_0)}. \quad (6.15)$$

It is also possible to define the PCAC mass by using backward correlation functions (eq. 6.11 and 6.12) and this definition is usually denoted with m'

$$m'(x_0) = r'(x_0) + c_A s'(x_0) \quad (6.16)$$

6.3 Non-perturbative $O(a)$ improvement coefficients for $N_f=4$ theory

with r' and s' equivalent to eq. 6.14 and 6.14 with backward correlation functions f'_A and f'_P replacing the forward ones. Imposing the condition

$$m(x_0) = m'(x_0), \quad (6.17)$$

would give us the simplest non-perturbative definition of c_A

$$c_A = -\frac{r(x_0) - r'(x_0)}{s(x_0) - s'(x_0)}. \quad (6.18)$$

In Figure 6.2 the value of c_A obtained from this definition of c_A based on the condition 6.17 imposed at time coordinate $x_0 = T/2$ is denoted as $c_{A \text{ NP}}$. Another way to obtain c_A would be to request the following: the time derivatives of the PCAC mass should be equal to zero at x_0 . In Figure 6.2 we denote with $c_{A \text{ NP der. fw.}}$ the value of c_A for different gauge couplings coming from the condition involving the forward correlation functions

$$\partial_0 m(x_0) = 0, \quad (6.19)$$

or in terms of c_A

$$c_A = -\frac{r(x_0 + a) - r(x_0 - a)}{s(x_0 + a) - s(x_0 - a)}. \quad (6.20)$$

We can impose the condition equivalent to eq. 6.19 on the mass obtained with the backward correlation functions

$$\partial_0 m'(x_0) = 0, \quad (6.21)$$

which gives us yet another non-perturbative definition of c_A

$$c_A = -\frac{r'(x_0 + a) - r'(x_0 - a)}{s'(x_0 + a) - s'(x_0 - a)}. \quad (6.22)$$

The c_A extracted from condition 6.21 at time $x_0 = T/2$ is denoted as $c_{A \text{ NP der. bw.}}$ in the plots in Figure 6.2.

The numerical tests of the three proposed non-perturbative definitions of c_A are performed on $L/a = 8$ and 12 lattices. The resulting c_A dependence on the bare coupling g_0^2 is separately plotted for each lattice size in Figure 6.2. The previous non-perturbative determinations of c_A for the fit of the $N_f = 0$ [43] and $N_f = 2$ [103] are also shown in these plots. The question now is which of the four ways of determining c_A should be used as a firm definition of the PCAC mass, thereby defining the massless scheme itself? We observe that the non-perturbative determinations shown in Figure 6.2 are subject to strong cut-

6 Running coupling in $N_f=4$ theory

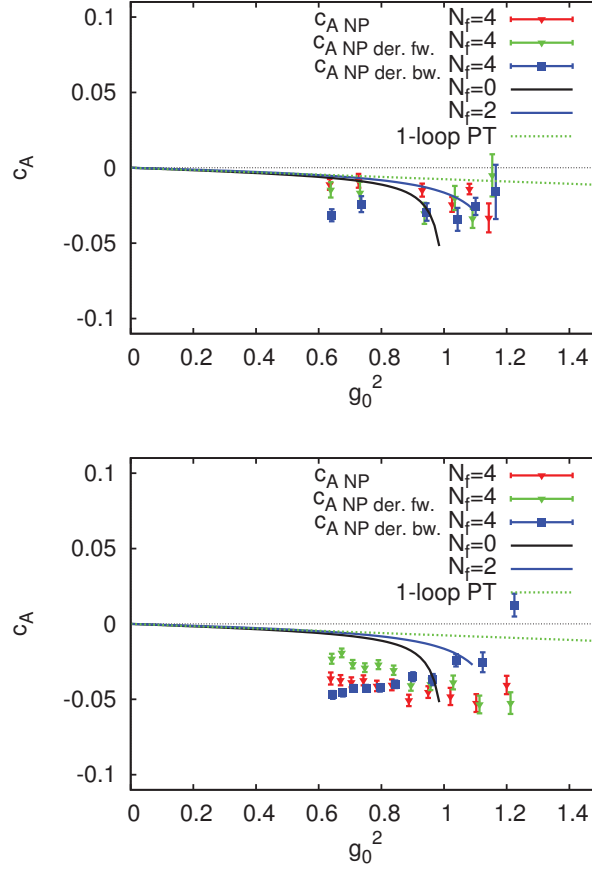


Figure 6.2: Different estimations of the improvement coefficient c_A . The continual lines represent the fit of the $N_f = 0$ and $N_f = 2$ non-perturbative determinations of c_A from [43] and [103]. The points denoted with c_A NP, c_A NP der. fw. and c_A NP der. bw. are obtained from the definitions of c_A given in eq. 6.18, 6.20 and 6.22, respectively. The upper panel shows these determinations for the $L/a = 12$ lattice size, the panel the bottom for $L/a = 8$. The dashed green line represents the 1-loop result (eq. 6.23) from Ref. [92], which is the determination we decide to use in the following, due to the strong cutoff effects in the non-perturbative determinations we performed for $N_f = 4$ and due to the fact that with increasing L/a the non-perturbative data approach to the perturbative curve.

6.3 Non-perturbative $O(a)$ improvement coefficients for $N_f=4$ theory

off effects and when one goes to higher lattice extent, the non-perturbative data approach to the perturbative curve. We hence conclude that the performed non-perturbative determination is not any better than using the 1-loop perturbative result obtained in Ref.[92]

$$c_A = -0.00756(1)g_0^2 \quad (6.23)$$

and we use eq. 6.23 for the numerical simulations that we want to perform. This function is plotted with a dashed green line in Figure 6.2. It would certainly be very interesting to see how the 2-loop expansion differs from the 1-loop expansion, but this would require a rather involved computation that has not been performed yet.

6.3.2 Other $O(a)$ improvement coefficients in $N_f = 4$ simulations

We have already discussed in section 5.5 that the $O(a)$ improvement of the Schrödinger functional requires additional improvement terms on the boundaries. For the choice of the considered boundary conditions, there are two such coefficients: the weight of the time-like plaquettes P attached to the boundary $w(P) = c_t(g_0)$ and the fermionic improvement coefficient \tilde{c}_t . The 2-loop expression of c_t and the 1-loop expression for \tilde{c}_t quoted in equations 5.31 and 5.32 are used to determine these parameters in our simulations.

Let us now devote a few more words to the determination of the Sheikholeslami-Wohlert improvement coefficient c_{SW} , which is crucial for the $O(a)$ improvement of the Wilson fermion action. This coefficient can be determined non-perturbatively — utilizing similar considerations to those applied in the effort to compute c_A non-perturbatively. Namely, one first introduces an alternative definition of the quark mass

$$M(x_0, y_0) = m(x_0) - s(x_0) \frac{m(y_0) - m'(y_0)}{s(y_0) - s'(y_0)} \quad (6.24)$$

$$= r(x_0) - s(x_0) \frac{r(y_0) - r'(y_0)}{s(y_0) - s'(y_0)}. \quad (6.25)$$

In the $O(a)$ improved theory that we are considering, this alternative quark mass definition differs from m only in $O(a^2)$ terms. $M'(x_0, y_0)$ is defined in an analogue way, but with forward and backward correlation functions interchanged. A condition imposed for the determination of c_{SW} was the vanishing of the following difference (see Ref. [43])

$$\Delta M(\frac{3}{4}T, \frac{1}{4}T) = M(\frac{3}{4}T, \frac{1}{4}T) - M'(\frac{3}{4}T, \frac{1}{4}T). \quad (6.26)$$

6 Running coupling in $N_f=4$ theory

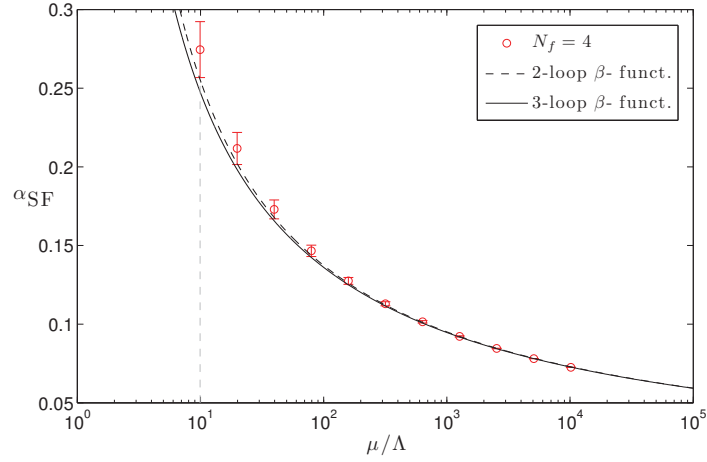


Figure 6.3: The running coupling in $N_f = 4$ obtained from the simulation data in [21], together with the perturbative determinations of the coupling in the Schrödinger functional renormalization scheme to 2- and 3-loops. The originally published data had a mistake in the error analysis. We plot here the data from ref. [21] with the corrected error bars.

The c_A term in the definitions of m and m' (cf. equations 6.13 and 6.16) is canceled in the above definition of the mass. Therefore, in spite of the problems we have experienced in the non-perturbative determination of c_A , with a moderate computational effort it is possible to determine c_{SW} non-perturbatively. This determination is done in Refs. [95, 104] and the resulting interpolation formula is quoted in Table 2.1, together with the results of similar determinations for different numbers of fermion flavors. This interpolating result is used for our simulations that follow.

6.4 Previous computation of the running coupling in $N_f = 4$ Wilson QCD and how to improve it

The running of the QCD coupling in $N_f = 4$ theory has previously been computed non-perturbatively only within two collaborations. The results for the four flavors of staggered fermions are published in Ref. [105], whereas the result for the four flavors of Wilson fermions are published in Refs. [21, 95]. The latter is the only non-perturbative computation of this quantity that has been performed so far for the $N_f = 4$ Wilson QCD. The final result for the Lambda parameter in

6.4 Previous computation of the running coupling in $N_f=4$ Wilson QCD

units of the hadronic scale L_{\max} obtained in Refs. [21, 95] reads⁴

$$\ln(\Lambda L_{\max}) = -2.294(153), \quad \text{at } \bar{g}^2(L_{\max}) = 3.45, \quad (6.27)$$

while the result of the running SF coupling obtained in Refs. [21, 95] is shown in Figure 6.3. The importance of an even more precise non-perturbative determination of the Λ parameter in the $N_f = 4$ theory for the world average of this quantity has already been discussed in chapter 1. The first important step towards this result is the precise determination of the step scaling function in the $N_f = 4$ theory. Our goal is to achieve this step by

- performing a cross-check of the results obtained in [21],
- improving the precision of the previously obtained SSF for roughly a factor of two, while still maintaining control over the systematic errors and keeping them negligible.

For the computation of the coupling, the massless SF scheme is achieved by tuning the PCAC mass (defined in section 6.1) to zero. The value of the hopping parameter κ for which the current quark mass vanishes, κ_c (critical κ), has to be tuned explicitly. We could re-use the entire tuning procedure done in [21, 95], but for the additional ensembles that we add to the following computation we had to perform this procedure ourselves. The starting hint and some more details of the PCAC mass tuning are discussed in appendix 5. Nevertheless, we would like to discuss here one important point regarding the tuning procedure. Namely, in order to achieve the wanted improvement in precision, and at the same time maintain control over the systematics resulting from the tuning of the quark mass to zero, we have to reinvestigate the bounds on the PCAC quark mass m_1 . The criterion for defining a massless scheme in [21] was to achieve $|m_1 L| \leq 0.005$ in the tuning of the quark mass. It is not a priori clear whether this criterion would suffice with the reduced uncertainty of the SSF that we are aiming at. We will therefore discuss the derivation of the bound on $|m_1 L|$ in the following section.

6.4.1 Tuning criteria for the PCAC mass

In order to estimate the systematic error in the SSF coming from the inexact tuning of the PCAC mass to zero, one needs to determine the dependence of the lattice SSF on the quark mass m_1 . The derivative of Σ with respect to $z = m_1 L$

⁴The error on $\ln(\Lambda L_{\max})$ quoted in ref. [21] does not coincide with the error given in eq. 6.27. Value quoted in eq. 6.27 is the corrected value, obtained after a mistake in the previously used error propagation code is removed.

6 Running coupling in $N_f=4$ theory

β	\bar{g}^2	am_1	\bar{g}^2	am'_1
5.0	3.932 (39)	0.03752 (13)	3.638 (34)	0.00037 (14)

Table 6.1: The renormalized coupling results for two $L/a = 8$ simulations obtained in Ref. [21] at the same value of the inverse bare coupling β . The data is used to estimate the numerical derivative in eq. 6.30.

reads

$$\left. \frac{\partial \bar{g}^2(2L)}{\partial z} \right|_{\bar{g}^2(L)=u} = \Phi(a/L) \bar{g}^4(L), \quad z = Lm_1. \quad (6.28)$$

The authors of [19] argue that Φ is a slowly varying function of a/L and give the estimate of its universal part from perturbation theory

$$\Phi(0) = 0.00957 N_f. \quad (6.29)$$

We perform here an additional non-perturbative estimation of the derivative 6.28. For that purpose, we use the two sets of $L/a = 8$ simulations from Ref. [21] and obtain

$$\left. \frac{\partial \bar{g}^2(2L)}{\partial z} \right|_{\beta=5.0, L/a=8} = \Phi(a/L) \bar{g}^4(L) = 0.98(17), \quad z = Lm_1, \quad (6.30)$$

at the highest value of the renormalized coupling that has been considered in Ref. [21]. The data taken from [21] for the purpose of this estimation are given in Table 6.1. We show the two discussed estimates of $\Phi(a/L)$ in Figure 6.4. To be on a safe side, we take for the new universal estimate of $\Phi(a/L)$ the non-perturbative value

$$\Phi(a/L) = 0.08 \quad \text{at} \quad L/a = 8, \quad (6.31)$$

coming from the upper bound depicted with the dashed blue line in Figure 6.4. Due to the mentioned weak dependence of Φ on a/L , we use this value in the following estimations of the limit to $|Lm_1|$ for all lattice extents considered.

Coming to the reduction of the statistical error in SSF, let us recall that the typical statistical precision of the SSF from Monte Carlo simulations reads

$$\Delta(\bar{g}^{-2}) = \frac{1}{\bar{g}^4} \Delta(\bar{g}^2). \quad (6.32)$$

We require the systematic error coming from the mismatch in the tuning of the

6.4 Previous computation of the running coupling in $N_f=4$ Wilson QCD

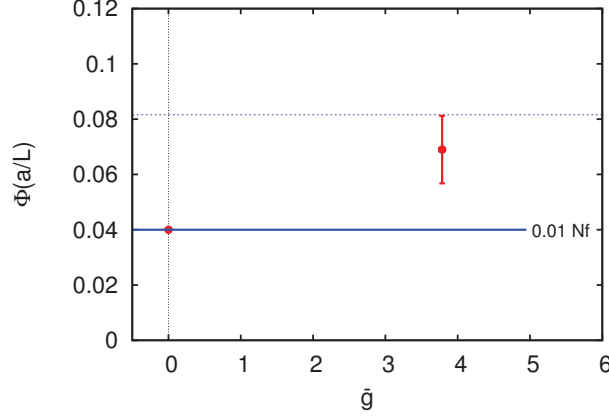


Figure 6.4: Dependence of function $\Phi(a/L)$ on \bar{g}^2 . At $\bar{g}^2 = 0$ we have the perturbative(continuum) value for s/\bar{g}^4 given in 6.29. The red point at $\bar{g}^2 \approx 3.9$ comes from the non-perturbative estimate in eq. 6.30 at $L/a = 8$.

PCAC mass to be at most *one third* of the statistical error in the SSF

$$\Delta^{\text{sys}}(\bar{g}(2L)) \leq \frac{1}{3} \bar{g}^4(L) \Delta^{\text{stat}}(\bar{g}^{-2}(2L)). \quad (6.33)$$

Using the non-perturbatively obtained value from eq. 6.31 we estimate the systematic error to be

$$\Delta^{\text{sys}}(\bar{g}(2L)) = \frac{\partial \bar{g}^2(2L)}{\partial z} |z| \approx 0.08 \bar{g}^4(L) |z|, \quad z = m_1 a \times \frac{L}{a}. \quad (6.34)$$

Finally, we obtain the limit on $m_1 L$, such that the condition 6.33 is satisfied

$$|m_1 a| \leq \frac{a}{L} \times \frac{1}{3} \times \frac{1}{0.08} \times \Delta^{\text{stat}}(\bar{g}^{-2}(2L)). \quad (6.35)$$

In Appendix 6, we quote the statistical precision for the lattices $L/a = 6, 8$ from Ref [21]. We can see that the tuning of the PCAC mass performed in [21] already satisfies the bound 6.35, even if we were to reduce the statistical error by a factor of two in the simulations we plan to perform. This facilitates the setting up of new simulations, since the predefined values of κ_{cr} from [21] may be used. The new parameter sets that we add to the previous study have to be tuned to satisfy the derived bound from 6.35. Some more details of the additional tuning are given in Appendix 7. We also show in Tables 3 - 5 of Appendix 6 that, in the final set of our new simulations, we have reached the precision required by expression 6.35.

6.5 New result of the running coupling in $N_f = 4$ theory

6.5.1 Simulations

We have simulated a wide range of energies from hadronic to high energy scales, where the matching to perturbation theory is performed. This range is covered by the choice of inverse bare gauge couplings $\beta \in [5.2, 9.45]$, for which the non-perturbative estimate of c_{SW} from [104] holds. Since in the previous study of $N_f = 4$ running coupling [21] the lattices $L = 4$ have proven to have large cutoff effects, we proceed immediately to simulating $(L = T)$ $L = 6, 8$ lattices. The simulations are performed using the SF-MP-HMC package specially developed for this purpose, whose performance has been discussed in section 5.6.1.

Note that unlike the measurement of the standard lattice observables where the number of MDUs of $\mathcal{O}(100 - 1000)$ suffices for precise estimation of the observable, the SF coupling is very noisy and requires $\mathcal{O}(100000)$ MDU for each parameter set $(\beta, L/a)$ in order to obtain an aimed precision of the order of percent. Due to the infrared cutoff that the SF formulation provided and the fact that our strategy does not need large lattice extents (since finite volume is treated as an observable), one is still able to achieve the required precision for the parameter sets of interest.

Obtaining a high precision estimate for the SF coupling from lattices larger than $L = 16$ was not possible with the GHMC code used in [21]. We demonstrate here that simulating $L = 24$ lattices is a realistic task with the SF-MP-HMC package and modern computational resources. To this end, we add one simulation point for the $L = 12$ lattice, in order to check the cutoff effects of our estimate from $L = 6, 8$ lattices. To keep the mass effects in the step scaling negligible, the hopping parameter is tuned such that the PCAC mass fulfills the criteria 6.35. The values of the renormalized coupling and the PCAC mass measured in the simulations of lattices $L = 6, 8, 12$ respectively are given in Tables 6.2, 6.3 and 6.4.

6.5.2 Improved lattice step scaling function

The lattice step scaling function $\Sigma(u, L/a)$ in the $\mathcal{O}(a)$ improved theory is expected to have lattice effects of order $\mathcal{O}(a^2)$. This is, however, not entirely true, although we use the non-perturbatively determined value of c_{SW} . Namely, for the boundary improvement coefficients that we use to define the SF scheme we have only perturbative estimates on disposal (see section 6.3). Therefore, the $\mathcal{O}(a)$ ef-

6.5 New result of the running coupling in $N_f=4$ theory

		$L/a = 6$		$L/a = 12$	
β	κ	\bar{g}^2	am_1	\bar{g}^2	am_1
5.25	0.138027	2.7487(60)	-0.00159(77)	3.591(26)	+0.00107(28)
5.55	0.137173	2.3658(57)	+0.00151(73)	2.904(17)	+0.00091(17)
5.85	0.136443	2.0944(47)	+0.00119(68)	2.498(16)	+0.00114(28)
6.45	0.135190	1.6983(26)	-0.00070(48)	1.9641(76)	-0.00089(10)
7.05	0.134123	1.4402(16)	+0.00084(42)	1.6124(48)	-0.00028(11)
7.65	0.133261	1.2497(12)	-0.00122(36)	-	-
8.25	0.132538	1.1045(09)	+0.00025(33)	1.2053(31)	-0.000330(64)
8.85	0.131935	0.9900(07)	+0.00011(32)	-	-
9.45	0.131411	0.8987(06)	-0.00018(28)	0.9624(17)	-0.000587(48)

Table 6.2: The results of the measurements of the renormalized coupling \bar{g}^2 and the tuned PCAC mass from the simulations of $L/a = 6$ and $L/a = 12$ lattices. All runs include 160000MDU or more.

		$L/a = 8$		$L/a = 16$	
β	κ	\bar{g}^2	am_1	\bar{g}^2	am_1
5.44	0.137507	2.7265(75)	+0.00047(45)	3.532(38)	-0.00127(16)
5.88	0.136393	2.2203(64)	+0.00037(41)	2.701(27)	-0.00121(20)
6.32	0.135433	1.8776(43)	+0.00056(26)	2.188(14)	-0.00131(14)
6.76	0.134597	1.6294(31)	+0.00042(21)	1.855(11)	-0.00046(16)
7.2	0.133903	1.4444(23)	-0.00014(20)	1.6375(74)	-0.00094(12)
7.64	0.133275	1.3046(16)	+0.00041(19)	1.4385(57)	-0.00069(10)
8.08	0.132736	1.1840(13)	+0.00019(17)	1.2906(46)	-0.00093(12)
8.52	0.132249	1.0855(11)	+0.00036(16)	1.1772(36)	-0.00055(11)
8.96	0.131821	1.0013(10)	+0.00035(17)	1.0827(31)	-0.00053(10)
9.4	0.131442	0.9314(09)	+0.00017(24)	0.9982(32)	-0.000498(91)

Table 6.3: The results of the measurements of the renormalized coupling \bar{g}^2 and the tuned PCAC mass from the simulations of $L/a = 6$ and $L/a = 12$ lattices. All runs include 160000MDU or more.

		$L/a = 12$		$L/a = 24$	
β	κ	\bar{g}^2	am_1	\bar{g}^2	am_1
9.45	0.131397	0.9629(19)	-0.000096(82)	1.0415(58)	-0.000472(82)

Table 6.4: A single point for the running from $L/a = 12$ and $L/a = 24$, performed in order to check the cutoff effects, which are discussed in section 6.5.4. Both runs include roughly 140000MDU.

6 Running coupling in $N_f=4$ theory

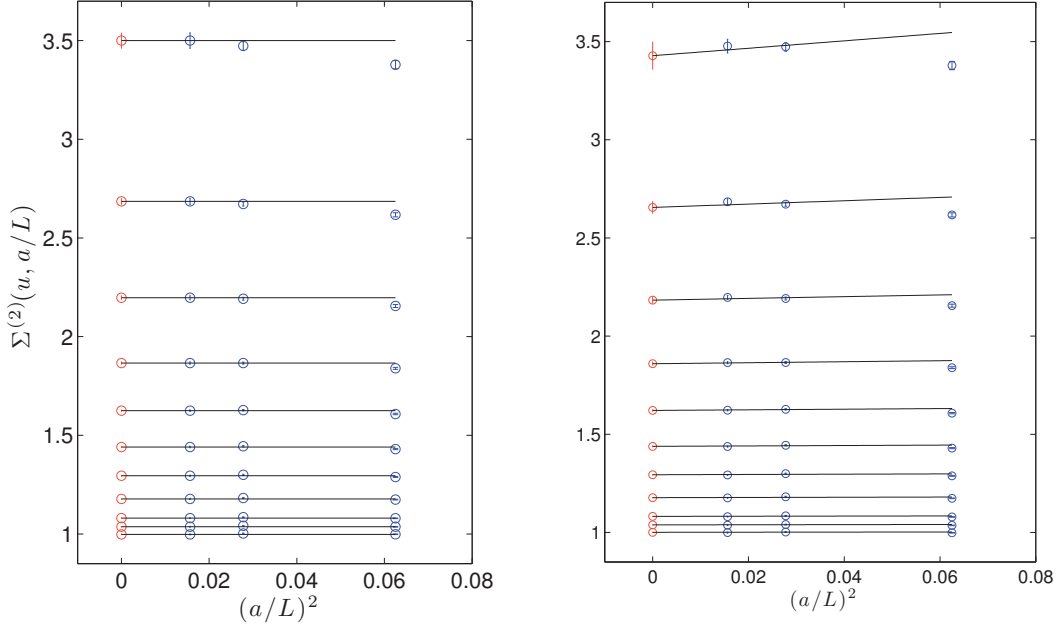


Figure 6.5: The *improved* lattice step scaling function $\Sigma^{(2)}(u, L/a)$ for $N_f = 4$ theory, obtained by performing a constant fit involving $L = 8$ data only (left panel) and the same quantity obtained performing a global fit of $L = 6, 8$ data (right panel).

fects are not fully cancelled, but this input from perturbation theory nevertheless guarantees that $O(a)$ effects in the SSF appear starting at two loop order.

It is additionally very important to take advantage of all possible input from perturbation theory that could lead to further improvement of the SSF. In this respect, we exploit the perturbative expansion of the quantity

$$\delta(u, a/L) = \frac{\Sigma(u, a/L) - \sigma(u)}{\sigma(u)} = \delta_1(a/L)u + \delta_2(a/L)u^2 + \dots, \quad (6.36)$$

with the dependence of the coefficients δ_1 and δ_2 on N_f known from [106]

$$\delta_1(a/L) = \delta_{10}(a/L) + \delta_{11}(a/L)N_f \quad (6.37)$$

$$\delta_2(a/L) = \delta_{20}(a/L) + \delta_{21}(a/L)N_f + \delta_{22}(a/L)N_f^2. \quad (6.38)$$

The numerical values of these coefficients for the lattice extents of interest are given in Table 6.5. Following the approach from [107] (also applied in [105] and [21]), we define the *improved* version of the lattice SSF which should have smaller

6.5 New result of the running coupling in $N_f=4$ theory

discretization errors than the original Σ

$$\Sigma^{(2)}(u, a/L) = \frac{\Sigma(u, a/L)}{1 + \delta_1(a/L)u + \delta_2(a/L)u^2}. \quad (6.39)$$

The cutoff effects of $\Sigma^{(2)}(u, a/L)$ will start at order $a \times u^4$ and additionally all terms of order $a^m \times u^n$, for any m and $n \leq 3$ are cancelled. The only remaining $O(a)$ effects in $\Sigma^{(2)}(u, a/L)$ ($a \times u^4$) have proven to be small for $N_f = 2$ theory [19]. We expect the same to be the case in $N_f = 4$ theory and the improved step scaling function is then expected to converge to the continuum SSF *effectively* at the rate

$$\Sigma^{(2)}(u, a/L) = \sigma(u) + O(a^2). \quad (6.40)$$

Note that this approach of correcting the lattice SSF can be applied irrespective of whether or not the action is improved.

6.5.3 Continuum limit of the SSF

The standard computation of the SSF, as described in section 6.1, would require that we tune the inverse bare coupling β such that the renormalized coupling is fixed to a certain value $\bar{g}^2(L) = u$ and compute the lattice SSF $\Sigma(u, L/a)$ at the tuned values of β for a range of u and for different lattice extents L/a . This procedure is computationally expensive, since each tuning of β produces an additional cost. Still, as there was no alternative known, this was the procedure of choice for many computations of the ALPHA collaboration in the past[17–20]. A more convenient proposal which reduces the computational cost and tuning procedure was given in [108]. The authors suggest to perform simulations at several values of bare coupling at L/a and then perform an interpolation of the running coupling $\bar{g}^2(\beta, L/a)$ with a smooth function of β . This procedure has proven to be successful in both computations of the $N_f = 4$ running coupling performed so far [21, 105] and we decide to follow the authors of [21] in their choice of the

L/a	δ_1	δ_2
6	−0.0045	0.0013
8	−0.0028	0.00013
12	−0.0010	0.00003

Table 6.5: Discretization errors of the SSF (eq. 6.36) for $N_f = 4$ and $L/a = 6, 8, 12$. The expansion coefficients are computed from the perturbative results given in [106].

6 Running coupling in $N_f=4$ theory

u	L/a	$\Sigma(u, a/L)$	$\Sigma^{(2)}(u, a/L)$	u	L/a	$\Sigma(u, a/L)$	$\Sigma^{(2)}(u, a/L)$
0.9300	4	0.9953(16)	0.9986(16)	1.4435	4	1.6132(43)	1.6127(43)
	6	0.9986(17)	1.0018(17)		6	1.6224(41)	1.6286(41)
	8	0.9986(31)	1.0007(31)		8	1.6200(50)	1.6252(50)
0.9629	4	1.0332(16)	1.0354(16)	1.6285	4	1.8503(59)	1.8456(58)
	6	1.0368(20)	1.0400(20)		6	1.8603(53)	1.8676(53)
	8	1.0354(23)	1.0376(23)		8	1.8607(66)	1.8673(66)
1.0000	4	1.0742(18)	1.0774(18)	1.8700	4	2.1700(77)	2.1567(76)
	6	1.0801(24)	1.0834(24)		6	2.1833(74)	2.1918(74)
	8	1.0775(20)	1.0800(20)		8	2.186(10)	2.195(10)
1.0813	4	1.1686(22)	1.1716(22)	2.2003	4	2.639(13)	2.607(12)
	6	1.1763(30)	1.1803(30)		6	2.658(13)	2.668(13)
	8	1.1720(25)	1.1750(25)		8	2.660(21)	2.672(21)
1.1787	4	1.2848(24)	1.2874(24)	2.6870	4	3.458(22)	3.374(21)
	6	1.2936(32)	1.2982(31)		6	3.466(22)	3.476(22)
	8	1.2887(27)	1.2921(27)		8	3.461(35)	3.480(35)
1.2972	4	1.4299(30)	1.4315(30)				
	6	1.4390(33)	1.4443(33)				
	8	1.4347(34)	1.4388(34)				

Table 6.6: Results for $\Sigma(u, a/L)$ and $\Sigma^{(2)}(u, a/L)$ for lattice sizes $L/a = 6, 8$ and couplings u . Values at $L/a = 4$ are taken over from [21] and are only given just for comparison: they do not enter in our analysis.

interpolation formula motivated by perturbation theory

$$\bar{g}^2(\beta, L/a) = \frac{6}{\beta} \left[\sum_{m=0}^n c_{m, L/a} \left(\frac{6}{\beta} \right)^m \right]^{-1}. \quad (6.41)$$

In the above interpolation, no coefficients were fixed to the perturbative values of any kind. We have checked that the dependence of the final results on the details of this interpolation ($n = 4, 5$) is negligible. After the interpolation has been performed, we compute $\Sigma(u, L/a)$ for a range of u from small to large couplings, starting from the value $u = 0.93$ and choosing the remaining couplings such that the recursion 6.3 is roughly fulfilled. The resulting values for the lattice SSF $\Sigma(u, L/a)$ and its improved form $\Sigma^{(2)}(u, a/L)$, after the above described interpolation has been performed, are given in Table 6.6. The continuum limit of the SSF is obtained in two different ways

6.5 New result of the running coupling in $N_f=4$ theory

u	$\sigma(u)$	$\Delta(\sigma(u))$
0.93	1.0007	0.0031
0.9629	1.0376	0.0023
1.0000	1.0800	0.0021
1.0813	1.1750	0.0025
1.1787	1.2921	0.0027
1.2972	1.4388	0.0034
1.4435	1.6252	0.0050
1.6285	1.8673	0.0066
1.8700	2.1949	0.0103
2.2203	2.6721	0.0208
2.6870	3.4800	0.0353

Table 6.7: Continuum extrapolation of the step scaling function, performing the constant fit on the L/a data from Table 6.6 (cf. Figure 6.5).

- **Global fit.** Perform a fit to $L/a = 6, 8$ data

$$\Sigma^{(2)}(u, a/L) = \sigma(u) + \rho u^4 (a/L)^2, \quad (6.42)$$

with a continuum SSF $\sigma(u)$ that depends on u and a global parameter ρ which quantifies the cutoff effects.

- **Constant fit.** At each coupling u perform a constant fit involving $L/a = 8$ data only.

The continuum extrapolation of the improved lattice SSF $\Sigma^{(2)}(u, a/L)$ for the case when the global fit is performed is plotted in the left panel of Figure 6.5 and the case with the constant fit of $L/a = 8$ data is plotted in the right panel of Figure 6.5. Both in Table 6.6 and in Figure 6.5, in addition to $L/a = 6, 8$, we also give $L/a = 4$ data, which is taken over from [21]. The latter is here just to guide the eye and does not enter any further analysis. We can conclude from Figure 6.5, as well as from the value of the parameter ρ (cf. eq. 6.42)

$$\rho = 0.035(52) \quad (6.43)$$

that the cutoff effects tend to be small. Note that the difference between $\Sigma^{(2)}(u, L/a)$ and $\Sigma(u, L/a)$ in Table 6.6 is small. Also, the results of the $L/a = 8$ data agree with the results from a global fit of $L/a = 6, 8$ within one sigma. Nevertheless, to be on the safe side and eliminate the cutoff effects of $L/a = 6$ data fully, in the following we will only quote as our main result the constant fit of $L/a = 8$ data (as it has been done in [21]). In Table 6.7, we give the values of the continuum extrapolated values for the SSF for the constant fit of $L/a = 8$. We will come back

6 Running coupling in $N_f=4$ theory

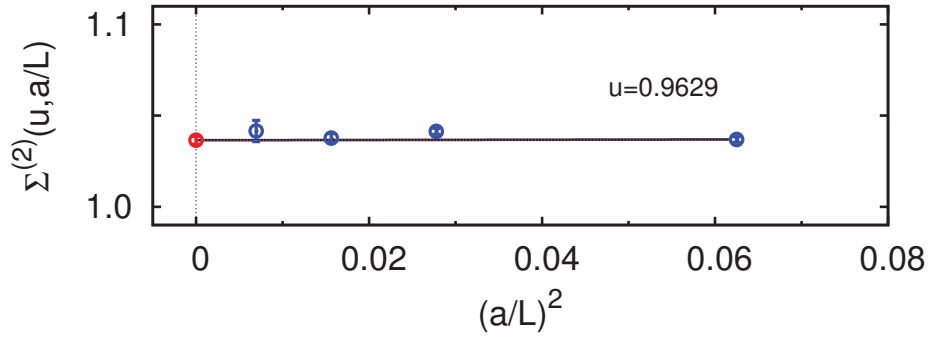


Figure 6.6: The extrapolation of SSF at $u = 0.9629$ for $L = 6, 8$ data. This is the value of the coupling where the $L = 12$ simulation is performed. The $L = 6, 8$ lattices are used in the computation of the SSF and the running coupling in sections 6.5.3 and 6.5.5 and $L/a = 4$ point is taken from [21] just as an illustration of the cutoff effects. The linear fit of $L/a = 8$ data and the global fit of $L/a = 6, 8$ data plotted on top of each other. They both agree with the additional $L/a = 12$ simulation data within errorbars. The red point shows the continuum value obtained from the constant fit of the $L/a = 8$ data.

to the discussion of the cutoff effects in section 6.5.4.

6.5.4 Cutoff effects

In order to check the cutoff effects of taking only $L/a = 6, 8$ lattices in the computation of the running coupling, we repeat one horizontal step of Figure 6.5 and add one more (finer) lattice resolution, corresponding to the $L/a = 12$ simulation given in Table 6.4. We can conclude that as a consequence of the careful choice of the definition of the coupling itself as well as the other details of the discretization, the dependence of the SSF on the lattice resolution turns out to be extremely weak so that the continuum extrapolations ($a/L \rightarrow 0$) are already rather safe with the small lattice extents used in [21], as well as in this study.

6.5.5 Running coupling

After performing the continuum limit of the SSF at the chosen values of u , we use a fifth order polynomial to obtain the interpolating estimate of $\sigma(u)$ at the whole range of couplings $0 \leq u \leq 2.7$. As already mentioned, we use for this purpose

6.5 New result of the running coupling in $N_f=4$ theory

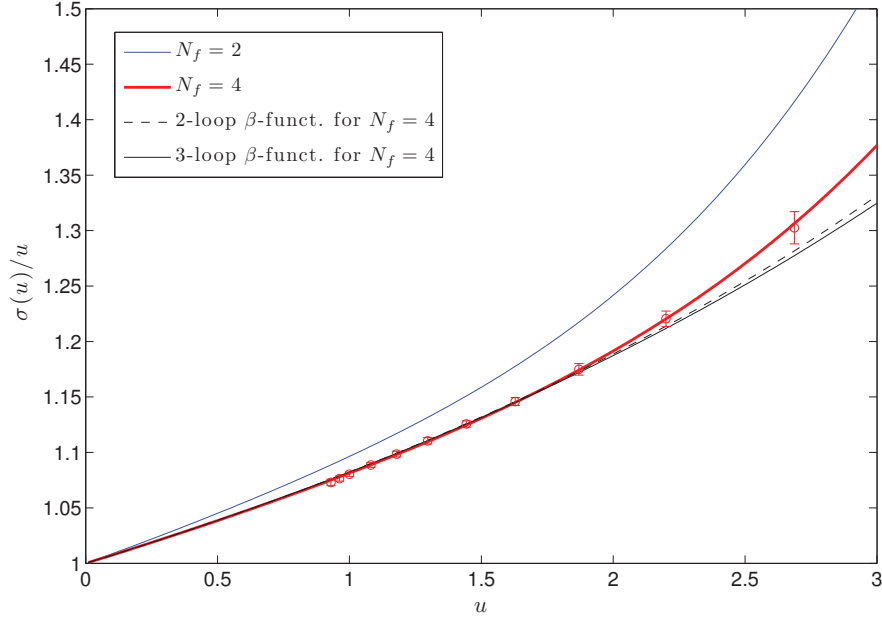


Figure 6.7: Continuum step scaling function for $N_f = 4$ theory. The result for $N_f = 2$ is given for comparison. Dashed lines are the perturbative results from integrations with the 2-loop and 3-loop beta function.

the results coming from the constant fit of $L/a = 8$ data (cf. Table 6.7) and obtain

$$\sigma(u) = u + s_0 u^2 + s_1 u^3 - 0.012 u^4 + 0.012 u^5, \quad 0 \leq u \leq 2.7. \quad (6.44)$$

The fit of the non-perturbative $N_f = 4$ data is plotted in Figure 6.7, together with the non-perturbative result for $N_f = 2$ theory [19] and the 2- and 3-loop perturbative result for $N_f = 4$ theory. Coefficients s_0 and s_1 are universal (cf. eq. 5.25 and 5.26) and obtained from perturbation theory. We notice the agreement we obtain with the perturbative estimates of the SSF over the whole interval of coupling u . Namely, our interpolation agrees with the PT result within one sigma, except at the largest coupling where the difference is slightly larger, but still smaller than two sigma. Finally, we complete step 2. of the strategy to extract the Lambda parameter described in section 6.2. Namely, we use the fit function obtained in 6.44 to give the estimate of $\ln(\Lambda L_{\max})$ in $N_f = 4$ theory. Starting from the highest coupling $u_{\max} = \bar{g}^2(L_{\max})$, chosen such that the associated scale L_{\max} is in the hadronic range, we recursively solve the following equation n -times

$$\sigma(\bar{g}^2(L/2)) = \bar{g}^2(L). \quad (6.45)$$

6 Running coupling in $N_f=4$ theory

i	u_i	$\ln(\Lambda L_{\max})$
0	3.45	-2.028
1	2.656(19)	-2.067(23)
2	2.193(19)	-2.079(35)
3	1.871(17)	-2.079(42)
4	1.635(14)	-2.073(48)
5	1.453(13)	-2.065(55)
6	1.309(12)	-2.055(61)
7	1.191(11)	-2.046(68)
8	1.0934(97)	-2.036(74)
9	1.0105(90)	-2.027(80)
10	0.9394(83)	-2.018(86)

Table 6.8: Values estimated for $\ln(\Lambda L_{\max})$ for the value of L_{\max} set with $\bar{g}^2(L_{\max}) = 3.45$. We take our final result from the step $i = 9$.

In this way, we obtain values for $\bar{g}^2(L_{\max}/2^i)$, $i = 1 \dots n$, where for a sufficiently large number of steps, we arrive to the regime where this coupling is perturbative and it is safe to express Λ in terms of L_{\max} using the perturbative expansion from eq. 2.54

$$(\Lambda L_{\max}) = 2^i (b_0 \bar{g}^2)^{-\frac{b_1}{2b_0^2}} e^{-\frac{1}{2b_0 \bar{g}^2}} e^{-\int_0^{\bar{g}} dx [\frac{1}{\beta(x)} + \frac{1}{b_0 x^3} - \frac{b_1}{b_0^2 x}]} . \quad (6.46)$$

The values for $\ln(\Lambda L_{\max})$ are given in Table 6.8. We take our final result from the step $i = 9$ from Table 6.8

$$\ln(\Lambda L_{\max}) = -2.027(80). \quad (6.47)$$

The choice of the step for quoting the final result ($i = 9$) is taken to be the same as in Ref. [21]. Note that, taking into account the data obtained in this work, the choice $i = 9$ could be considered overconservative since the plateau in $\ln(\Lambda L_{\max})$ with our data arrives earlier than in [21]. Therefore, already reading off a final value from the step $i = 5$ is a viable choice.

As it was discussed in section 6.2, it's still a significant challenge for future work to perform step 1. of the described strategy which would enable us to quote the value of the Λ parameter in physical units.

Finally, in Figure 6.8 we show the running coupling in the SF scheme, expressed in units of Λ . Even at the strongest coupling included in the computation, the obtained non-perturbative result shows the agreement with the perturbation theory

6.5 *New result of the running coupling in $N_f=4$ theory*

estimates within one standard deviation. With the results of [21], a 2-sigma effect at the largest considered value of the SF coupling has been reported, but due to the error in the error analysis code, the final error estimate in this work is underestimated. Our results agree with the corrected result from [21] within one sigma. Nevertheless, it is expected that at energies higher than the ones considered in this study the deviation of the non-perturbatively obtained SF coupling from the perturbative estimate will appear. For that reason it is very important to extend this study to lower energies and some interesting proposals for how this can be done will be discussed in Chapter 8.

6 Running coupling in $N_f=4$ theory

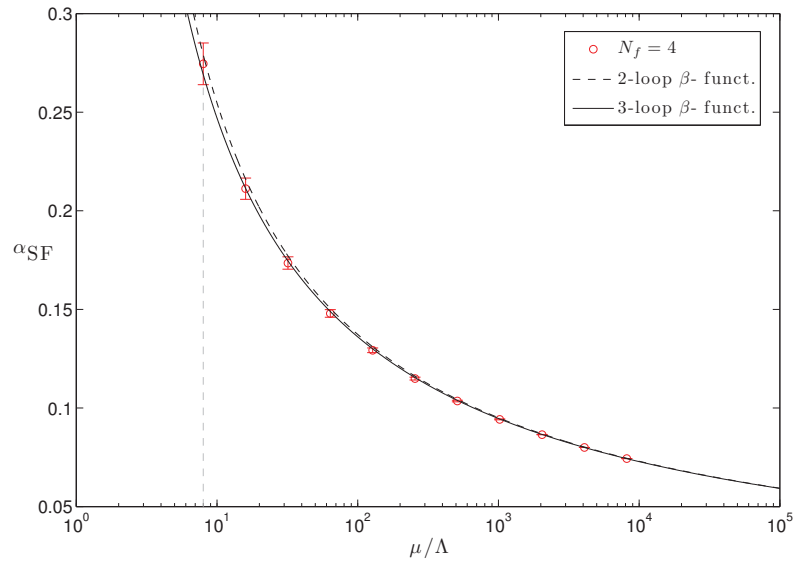


Figure 6.8: The running coupling in $N_f = 4$ obtained from the simulations summarized in section 6.5.1, employing a procedure described in section 6.5.3. The perturbative determinations of the coupling in the Schrödinger functional renormalization scheme to 2- and 3-loops are also given.

7 The strange quark mass and the Lambda parameter for $N_f = 2$ theory

The determination of the Lambda parameter in units of the hadronic scale L_{max} from chapter 6 is an important step towards the final comparison of this parameter from the perturbation theory and from the lattice. Nevertheless, the impact of this determination on the phenomenological applications will be possible only after the scale of the simulations is set and the quantities in physical units are attained. Performing the set of large scale simulations at $N_f = 4$ is a tedious and lengthy project, predicted to be finished in the next couple of years. Until this has been achieved, we go one step back and use the running of the coupling and running of the mass data from ALPHA collaboration [19, 20], in order to perform a determination of the Lambda parameter and the strange quark mass for two flavour QCD. This represents the finalization of a long-term program of the ALPHA collaboration of computing these parameters for $N_f = 2$ theory, using the Schrödinger functional strategy to overcome the multi-scale problem and keep the full control over the systematic errors. The results which will be presented here are obtained with the help of the precise scale determination from an extensive set of large scale simulations produced with the DD-HMC code and the MP-HMC code discussed in chapter 4. In the scale setting a physical quantity used is the kaon decay constant f_K . With this scale we achieve a total error of approx. 2%, employing two different strategies for the chiral extrapolation which agree within errorbars. First part of this chapter will be dedicated to the improved scale setting and afterwards we move towards giving the physical values for the RGI values of the strange quark mass and Λ -parameter, in the setup with two dynamical flavors of light quarks. The results which will be presented here have already been published in Refs. [24, 109]. Text of sections 7.1 and 7.2 (with minor modifications to match the notation of Ref. [24]) is fully taken over from Ref. [109]. Text of the sections 7.3.1 and 7.4.1 as well as all the plots and tables in this chapter (7) are taken over from Ref. [24].

7 The strange quark mass and the Lambda parameter for $N_f=2$ theory

id	L/a	β	κ	κ_s	R_0	$m_\pi[\text{MeV}]$	$m_\pi L$
A2	32	5.2	0.13565	0.135438(20)	5.485(21)	630	7.7
A3			0.13580	0.135346(20)	5.674(32)	490	6.0
A4			0.13590	0.135285(20)	5.808(34)	380	4.7
A5			0.13594	0.135257(20)	5.900(24)	330	4.0
E4	32	5.3	0.13610	0.135836(17)	—	580	6.2
E5			0.13625	0.135777(17)	6.747(59)	440	4.7
F6	48		0.13635	0.135741(17)	6.984(51)	310	5.0
F7			0.13638	0.135730(17)	7.051(43)	270	4.3
N4	48	5.5	0.13650	0.136278(08)	9.32(30)	550	6.5
N5			0.13660	0.136262(08)	9.31(26)	440	5.2
N6			0.13667	0.136250(08)	9.55(11)	340	4.0
O7	64		0.13671	0.136243(08)	9.68(10)	270	4.2

Table 7.1: Overview of the ensembles used in this study. We give the label, the spatial extent of the lattice, $\beta = 6/g_0^2$, the hopping parameter κ of the sea quarks, the hopping parameter κ_s of the strange quark, the scale $R_0 = r_0/a$, the mass of the sea pion m_π and the product $m_\pi L$, which is always larger or equal than 4. All lattices have dimension $T \times L^3$ with $T = 2L$.

7.1 Lattice parameters

The following study is based on ensembles generated within the CLS effort, with the Wilson plaquette gauge action together with $N_f = 2$ mass-degenerate flavors of $O(a)$ improved Wilson fermions. The simulations are using either M. Lüscher's implementation of the DD-HMC algorithm (cf. section 4.1 and [68]), or our implementation of the MP-HMC algorithm (cf. chapter 4 and [74]). The list of ensembles used in the analysis is shown in Table 7.1. Lattice spacings are ranging from 0.05fm to 0.08fm and their precise determination will be presented in the following section. The ensembles cover a wide range of pion masses going down to 270MeV, whereas all lattice volumes satisfy the requirement $m_\pi L \geq 4$ to keep finite volume effects under control.

7.2 Setting the scale from f_K

To determine the scale and match to experimental values we have to extrapolate decay constants to the physical quark masses. For this we use two variants based on chiral perturbation theory (ChPT). The first one employs SU(3) chiral perturbation theory with a quenched strange quark [110]. The aim here is to minimize the chiral corrections by keeping the sum $(M_{\text{light}} + M_s)$ of the light quark mass and

7.2 Setting the scale from f_K

the strange quark mass approximately fixed. Chiral corrections are expected to be well behaved, since in this setup all Goldstone bosons have a mass of at most the physical kaon mass ($\approx 500\text{MeV}$). The second approach uses SU(2) ChPT expanding only in the light quark mass ($M_{\text{light}} = (M_u + M_d)/2$) [111]. Whereas the first strategy is most useful for $N_f = 2$, the second one is equally well applicable in $N_f = 2$ theory with a quenched strange quark and in the $N_f = 2 + 1$ theory, the only difference being the low energy constants. The difference between the two strategies in approaching the physical point is illustrated in the left panel of Figure 7.1.

Let us already at the very beginning point out the distinction we make in notation of the kaon decay constant in physical units f_K and in lattice units F_K

$$F_K \equiv a f_K. \quad (7.1)$$

In the setup described in the next two sections we use two quarks with hopping parameters $\kappa_1 = \kappa_2$ and two additional quenched quarks with hopping parameters $\kappa_3 = \kappa_4$. From these we build pseudoscalars, pions with mass m_π from two quarks with $\kappa_1 = \kappa_2 = \kappa_{\text{sea}}$. The kaons we build from quarks with hopping parameters (κ_1, κ_3) . The physical point is defined by $m_{\pi, \text{phys}} = 134.8\text{MeV}$ and $m_{K, \text{phys}} = 494.2\text{MeV}$, the values in QCD with the electromagnetic interaction being switched off[112]. The two strategies differ in how κ_3 is chosen as a function of κ_1 .

In the following computations we have included the effect of the autocorrelations in the error analysis in a very conservative way. The details can be found in Appendix 7. Let us just mention here that for the estimation of the error we take into account the tail of the autocorrelation function[50]. Thus, we are convinced that we have statistical errors fully under control. They are computed following the procedures detailed in [113, 114].

7.2.1 Partially quenched SU(3) Chiral Perturbation Theory (Strategy 1)

In this approach we define the strange quark hopping parameter κ_3 through the dimensionless ratio

$$R_K = \frac{m_K^2(\kappa_1, \kappa_3)}{f_K^2(\kappa_1, \kappa_3)} = \frac{m_{K, \text{phys}}^2}{f_{K, \text{phys}}^2}, \quad (7.2)$$

for each value κ_1 and the gauge coupling (β), such that the l.h.s. of the equation remains equal to the constant ratio $R = m_{K, \text{phys}}^2 / f_{K, \text{phys}}^2$. Rather than a fixed

7 The strange quark mass and the Lambda parameter for $N_f=2$ theory

[!htbp]

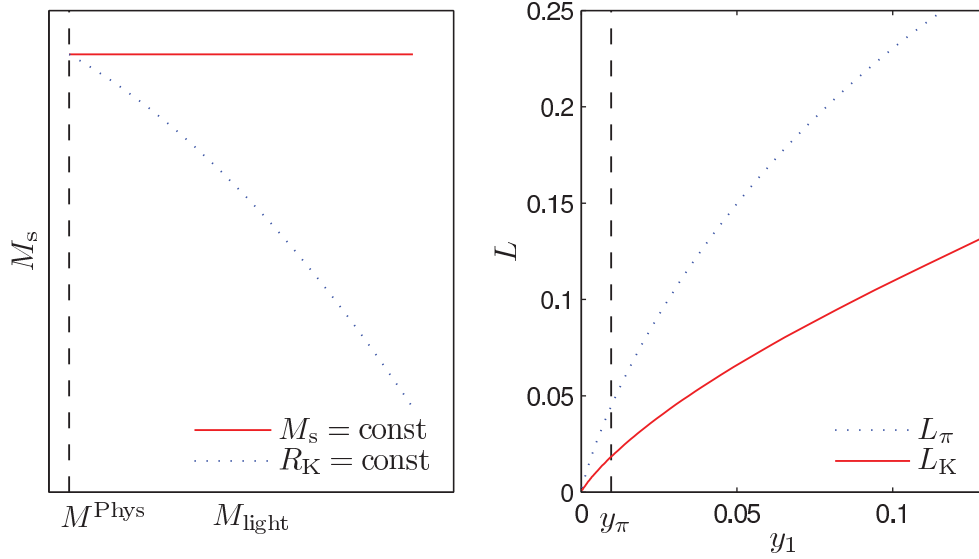


Figure 7.1: Left: A sketch of the two approaches for chiral extrapolation to the physical point. Strategy 1 (dotted line) imposes the condition on the sum of the strange and light quark mass: $M_s + M_{\text{light}} = \text{const.} + O(M^2)$, where $M_{\text{light}} = (M_u + M_d)/2$, while the second strategy (full line) keeps the strange quark mass M_s constant during the extrapolation. Right: the two functions L_K and L_π , see eq. 7.6 and 7.11 respectively, in the interval $y_1 \in [0, y_K]$.

strange quark mass, this corresponds to $M_s + M_{\text{light}} = \text{const.}$ to lowest order in the expansion in the quark masses and this is expected to give a flat chiral extrapolation for f_K . The condition 7.2 determines a value of $\kappa_3 = h(\kappa_1)$ as a function of the sea quark hopping parameter and it can be obtained by interpolation. After the dependence of κ_3 on κ_1 is determined, it remains to extrapolate the decay constant $F_K(\kappa_1, h(\kappa_1))$ to the physical point, defined by the dimensionless ratio

$$R_\pi = \frac{m_\pi^2(\kappa_1, h(\kappa_1))}{f_K^2(\kappa_1, h(\kappa_1))} = \frac{m_{\pi, \text{phys}}^2}{f_{K, \text{phys}}^2}. \quad (7.3)$$

7.2 Setting the scale from f_K

In the last step we use the prediction of the above functional form coming from SU(3) ChPT[110]

$$f_K(\kappa_1, h(\kappa_1)) = f_{K,\text{phys}} \left[1 + \bar{L}_K(y_1, y_K) + \left(\alpha_4 - \frac{1}{4} \right) (y_1 - y_\pi) + \mathcal{O}(y^2) \right], \quad (7.4)$$

$$\bar{L}_K(y_1, y_K) = L_K(y_1, y_K) - L_K(y_\pi, y_K), \quad (7.5)$$

$$L_K = -\frac{1}{2} y_1 \log(y_1) - \frac{1}{8} y_1 \log(2y_K/y_1 - 1), \quad (7.6)$$

where the variables y are defined as

$$y_1 = \frac{m_\pi^2(\kappa_1)}{8\pi^2 f_K^2(\kappa_1, h(\kappa_1))}, \quad (7.7)$$

$$y_K = \frac{m_{K,\text{phys}}^2}{8\pi^2 f_{K,\text{phys}}^2} = 0.12857 \quad (7.8)$$

$$y_\pi = \frac{m_{\pi,\text{phys}}^2}{8\pi^2 f_{K,\text{phys}}^2} = 0.00958. \quad (7.9)$$

Because of eq. 7.2, we have $y_3 \equiv m_K^2(\kappa_1, h(\kappa_1)) / [8\pi^2 f_K^2(\kappa_1, h(\kappa_1))] = 2y_K - y_1 + \mathcal{O}(y^2)$ and y_3 does not appear in eq. 7.4. In the right panel of Figure 7.1 we

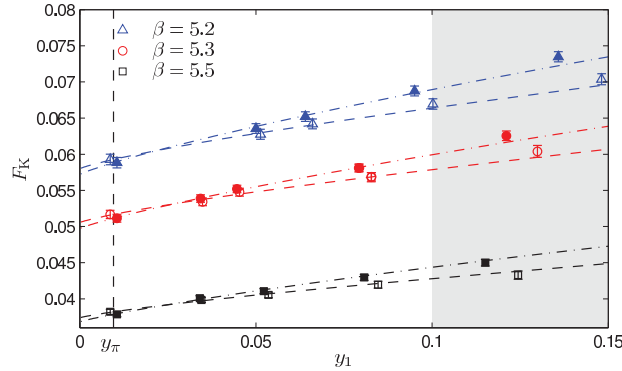


Figure 7.2: Chiral extrapolation of the kaon decay constant in lattice units for all three values of β . Open symbols and dashed lines correspond to strategy 1, while filled symbols and dash-dotted lines represent the outcome of the strategy 2. The extrapolated results coming from both strategies agree at the physical point. They are obtained by applying the global fit for all three values of gauge couplings β , imposing a cut $y_1 < 0.1$.

7 The strange quark mass and the Lambda parameter for Nf=2 theory

compare the chiral log function L_K to the one describing the chiral behavior of f_π ,

$$f_\pi(\kappa_1) = f_{\pi,\text{phys}} \left[1 + \bar{L}_\pi(y_1) + (\alpha_4 + \frac{1}{2}\alpha_5)(y_1 - y_\pi) + \mathcal{O}(y_1^2) \right], \quad (7.10)$$

$$L_\pi(y_1) = -y_1 \log(y_1), \quad (7.11)$$

$$\bar{L}_\pi(y_1) = L_\pi(y_1) - L_\pi(y_\pi). \quad (7.12)$$

Our condition 7.2 leads to the specific combination of chiral logarithms 7.6, which has very little curvature and is overall much smaller than L_π ; the suppression of the light quark mass dependence thus extends also to the NLO chiral logarithms. This suggests that the chiral extrapolation is much easier than for f_π and was one of our reasons to select f_K to set the scale. Of course, the counter terms α_i do not contribute in Fig. 7.1 (right), but as they are linear in y_1 , they also introduce no curvature. At the order in the chiral expansion represented in eq. 7.4, $\mathcal{O}(y_1^2)$, we can also replace

$$y_1 \rightarrow \tilde{y}_1 = \frac{m_\pi^2(\kappa_1)}{8\pi^2 f_\pi^2(\kappa_1)}, \quad (7.13)$$

with the corresponding replacement $y_\pi \rightarrow \tilde{y}_\pi$, which serves us as a check of the typical size of $\mathcal{O}(y^2)$ effects. The effect of this change on the example of the observable $r_0 f_K$ (see Appendix 7) shows that the cutoff effects are small and justifies the motivation for dropping the terms such as $a^2 y_1$ in the chiral expansion 7.4. Since this is the case, we determine the values of the kaon decay constant in lattice units at the physical point $F_{K,\text{phys}}$ by a direct application of

$$F_K(\kappa_1, h(\kappa_1)) = F_{K,\text{phys}} \left[1 + \bar{L}_K(y_1, y_K) + (\alpha_4 - \frac{1}{4})(y_1 - y_\pi) \right]. \quad (7.14)$$

Here the data at the three different β are combined in a global fit with one common value of α_4 , but, of course, with different $F_{K,\text{phys}}$ for the three different β . The lattice spacings are then obtained from

$$a = \frac{F_{K,\text{phys}}}{f_{K,\text{phys}}}. \quad (7.15)$$

Results are shown in Table 7.2, together with those from our alternative strategy which will be discussed in the following section.

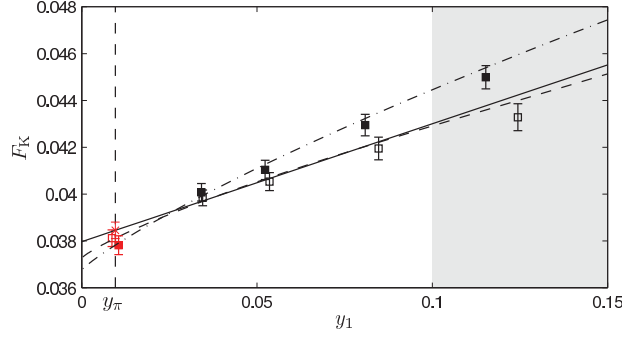


Figure 7.3: Detailed comparison of strategy 1, strategy 2 and a linear extrapolation at $\beta = 5.5$. The symbols are the same as in Figure 7.2 with the solid line representing the linear extrapolation of the open symbols. Note that the slopes given by the low energy parameters are determined from the global fit to all three β values.

7.2.2 SU(2) Chiral Perturbation Theory (Strategy 2)

In this approach, we work at the fixed strange quark mass and perform a chiral extrapolation in the light quark mass (M_{light}) using SU(2) chiral perturbation theory[111], also known as heavy meson ChPT. Since we are working with Wilson fermions, one has to keep fixed the axial Ward identity (PCAC) mass of the strange quark. We denote average quark masses of flavors r and s as m_{rs} ($r, s = 1, \dots, 4$), defined in a similar way as the PCAC mass in eq. 6.5 (cf. Appendix 7). The bare PCAC masses of the sea and the valence quark are defined by

$$m_1(\kappa_1) = m_{12} \quad m_3(\kappa_1, \kappa_3) = m_{34}. \quad (7.16)$$

We now extrapolate in the light quark mass at fixed mass of the strange quark. Namely, we tune for each sea quark mass the strange quark's hopping parameter such that the PCAC mass m_{34} has a prescribed value μ , which is independent of κ_1 . In principle, we should keep m_R^{34} fixed, but since the setting of certain improvement coefficients to zero (see eq. 36 in Appendix 9) cancels the κ_1 dependence of the ratio m_R^{34}/m_{34} , then keeping m_{34} fixed is equally good. This defines the function $\kappa_3 = s(\kappa_1, \mu)$. In practice, we first interpolate the data for $m_{34}(\kappa_1, \kappa_3)$ in κ_3 and then solve

$$am_{34}(\kappa_1, s(\kappa_1, \mu)) = \mu \quad (7.17)$$

for s , where the left hand side is represented by the interpolation formula. To find the value of μ corresponding to the physical point, we then perform a SU(2)

7 The strange quark mass and the Lambda parameter for Nf=2 theory

extrapolation [115, 116] to the chiral limit defined by condition 7.3. We first extrapolate $M_K^2 = (am_K)^2$ and F_K in y_1 to $y_1 = y_\pi$ at fixed value of μ

$$\begin{aligned} F_K(\kappa_1, s(\kappa_1, \mu)) &= P(\mu) \left[1 - \frac{3}{8} [y_1 \log(y_1) - y_\pi \log(y_\pi)] + \alpha_f(\mu)(y_1 - y_\pi) + O(M^2) \right] \\ M_K^2(\kappa_1, s(\kappa_1, \mu)) &= Q(\mu) \left[1 + \alpha_m(\mu)(y_1 - y_\pi) + O(M^2) \right]. \end{aligned} \quad (7.18)$$

These expressions represent the asymptotic expansions for small y_1 at fixed μ correct up to error terms of order y_1^2 . Let us note here that SU(2) ChPT for kaons does not take into account kaon loops as opposed to SU(3) ChPT. This corresponds to the production of *two* kaons, i.e., states with an energy of around one GeV. From this point of view SU(2) ChPT is not really worse than ChPT in the pion sector where $|\rho \pi\rangle$ intermediate states are dropped. From eq. 7.18, $Q(\mu)$ and $P(\mu)$ are computable for arbitrary values of μ . The requirement that m_K^2/f_K^2 attains its physical value at the physical light quark mass then defines μ_s , which at the same time sets the scale of the simulations

$$a = \frac{P(\mu_K)}{f_K} \quad \text{at} \quad \frac{Q(\mu_s)}{P(\mu_s)^2} = \frac{m_{K,\text{phys}}^2}{f_{K,\text{phys}}^2}. \quad (7.19)$$

The values of the lattice spacings from this strategy are shown in Table 7.2. Comparing to the results of the first strategy, we find a very good agreement as demonstrated in Figure 7.2. The details of comparing chiral extrapolations with different

β	Strategy 1			Strategy 2		
	5.2	5.3	5.5	5.2	5.3	5.5
$a[\text{fm}]$	0.0755	0.0658	0.0486	0.0749	0.0651	0.0482
$\Delta_{\text{stat.}} a$	0.0009	0.0007	0.0004	0.0009	0.0007	0.0004
$\Delta_{\text{syst.}} a$	0.0007	0.0007	0.0005	0.0012	0.0010	0.0007

Table 7.2: Lattice spacings from the first strategy obtained by applying SU(3) ChPT(left, [110]) and from the second strategy, based on SU(2) ChPT(right, [115, 116]). The first line shows the values of the lattice spacing in fm from both strategies and the second line shows the statistical error. $\Delta_{\text{syst.}}$ is the systematic error due to the chiral extrapolation obtained as a difference between the chiral and the linear fit.

value of the cut on y_π to the linear extrapolation are given in Appendix 7. We take the central values from the results of strategy 1 with cut $y_1^{\text{max}} = 0.1$ as our final result for the following applications. As a systematic error we take into account the deviations to the fit following strategy 2 and to a simple linear extrapolation; for our smallest lattice spacing these different extrapolations are compared more

closely in Figure 7.3.

7.3 Determination of the Λ parameter

To calibrate the overall energy scale, we take advantage of the non-perturbative Schrödinger functional scheme discussed in chapter 5. It is again used as an intermediate scheme which connects the low and high energy physics, but this time for studying the running of the coupling and the quark mass in $N_f = 2$ Wilson theory. The results which will be used in the following determination of the Lambda parameter and the strange quark mass in this theory use the initial non-perturbative running data from [19, 20]. We then follow the strategy explained in section 7.2.2 and fix a large enough value of the coupling $\bar{g}^2(L_1)$ which is in the low-energy region and relates the associated distance, L_1 , to a non-perturbative, infinite-volume observable, in our case f_K . We defined in this work L_1 through $\bar{g}^2(L_1) = 4.484$. At this value of the coupling we have a large and precisely tuned set of pairs $(L_1/a, \beta)$. Reanalyzing the data of ref. [19] at this point, we get the continuum value of

$$\Lambda L_1 = 0.264(15). \quad (7.20)$$

What remains to be done is to compute $f_K L_1$ in the continuum limit. To this end, we have to combine the updated data for L_1/a of ref. [24] with the decay constant F_K at physical quark masses in the previous section. Since the data points for L_1/a and F_K are at different values of β , we need to interpolate L_1/a to the values of the latter. This interpolation is addressed in appendix 7. Finally, the product $f_K L_1$ can be extrapolated to the continuum limit. [!htbp]

7.3.1 Continuum value of the Λ parameter

Figure 7.4 shows that in the continuum extrapolation of $L_1 f_K$ the cut-off effects are smaller than the statistical uncertainties; the numerical values are given in Table 7.4. Indeed, a constant extrapolation gives a $\chi^2/\text{d.o.f.}$ below unity. However, we use a linear extrapolation, allowing for $O(a^2)$ effects hidden by the statistical fluctuations. In this extrapolation the covariance between the three points from the interpolation in L_1/a is taken into account. For comparison with results in the literature, we give all results also in units of $r_0|_{y_1=y_\pi}$. The two combinations evaluate to

$$f_K L_1 = 0.315(8)(2) \quad r_0/L_1 = 1.252(33) \quad (7.21)$$

in the continuum limit. The final results come from strategy 1 for the chiral ex-

7 The strange quark mass and the Lambda parameter for $N_f=2$ theory

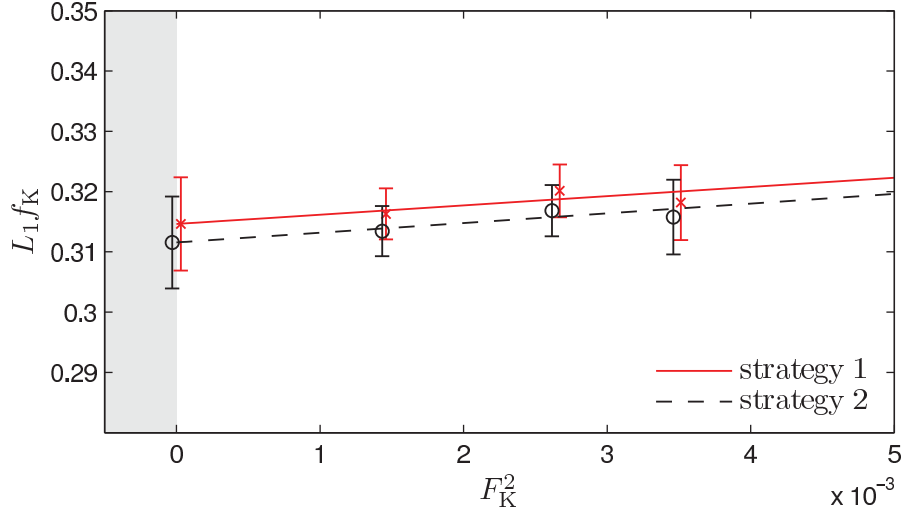


Figure 7.4: Continuum extrapolation of the product of lattice kaon decay constant f_K and matching scale L_1 , defined with $\bar{g}^2(L_1) = 4.484$. Even though the data show no cutoff effects, we have used a linear extrapolation to account for uncertainties from $O(a^2)$ effects within the error bars. The two strategies for the chiral extrapolation of $F_K = af_K$ agree well within the statistical uncertainties.

β	F_K
5.2	0.0593(7)(6)
5.3	0.0517(6)(6)
5.5	0.0382(4)(3)

Table 7.3: The kaon decay constant at the physical quark mass and the corresponding lattice spacing. The first error is statistical, the second systematic error due to the chiral extrapolation.

7.4 Determination of the strange quark mass

trapolation of F_K , given in Table 7.3. Strategy 2 is used to estimate the systematic

β	L_1/a	$L_1 f_K$	r_0/L_1	\bar{m}_s/f_K
5.2	5.367(82)	0.318(6)(3)	1.155(22)	0.530(12)(6)
5.3	6.195(51)	0.320(5)(4)	1.169(15)	0.577(11)(7)
5.5	8.280(80)	0.316(4)(2)	1.213(17)	0.617(11)(5)
cont.		0.315(8)(2)	1.252(33)	0.678(12)(5)

Table 7.4: Values of L_1/a , $L_1 f_K$, r_0/L_1 and \bar{m}_s/f_K at the three values of β . For the latter three, we also give the value extrapolated to the continuum limit. The running mass in the Schrödinger Functional scheme \bar{m}_s is given at the renormalization scale L_1 .

uncertainty; however, it is small compared to the statistical errors and we do not give it separately. We therefore quote

$$\Lambda^{(2)}/f_K = 0.84(6) \quad \text{and} \quad r_0 \Lambda^{(2)} = 0.331(22). \quad (7.22)$$

Now, as a result of our analysis, the error is dominated by the error on ΛL_1 (cf. eq. 7.20). We translate to the $\overline{\text{MS}}$ scheme using $\Lambda_{\overline{\text{MS}}}^{(2)} = 2.382035(3)\Lambda^{(2)}$ [90, 99] and find

$$\Lambda_{\overline{\text{MS}}}^{(2)} = 310(20) \text{ MeV} \quad \text{and} \quad r_0 \Lambda_{\overline{\text{MS}}}^{(2)} = 0.789(52). \quad (7.23)$$

7.4 Determination of the strange quark mass

We now proceed to the computation of the strange quark mass. The strategy we use is the one originally suggested in Ref. [18], which splits up the computation into several steps, similarly to the strategy applied for the computation of the Lambda parameter (cf. eq. 6.4). It circumvents the multi-scale problem a direct approach would face and therefore allows for a good control over the systematic errors. Earlier results have been presented in Ref. [20], here we improve on them with a much higher statistical and systematic accuracy.

To briefly summarize the procedure, the renormalized RGI mass M_s is given in terms of the bare PCAC mass m_s by

$$M_s = Z_M m_s = \frac{M}{\bar{m}(L)} \bar{m}_s(L) = \frac{M}{\bar{m}(L)} \frac{Z_A}{Z_P(L)} m_s, \quad (7.24)$$

where the computation of the renormalization constant Z_M is split in two steps.

7 The strange quark mass and the Lambda parameter for Nf=2 theory

The continuum value of the universal first factor M/\bar{m} has been computed in [20] for the two flavor theory which we consider here. It does not depend on the quark flavor or the lattice regularization. For the second factor, updated values of Z_P are given in [24]. Of course, the first factor and Z_P have to be evaluated at a common renormalization scale L . While the authors of [20] used $L = L_{\max}$ with $\bar{g}^2(L_{\max}) = 4.61$, we choose here $L = L_1$ with $\bar{g}^2(L_1) = 4.484$ as in the previous section. The first factor in eq. 7.24 is

$$M/\bar{m} = 1.308(16) \quad (7.25)$$

at this scale from a re-evaluation of the data from [20].

For the bare strange quark mass at physical light quark masses m_s , the final ingredient of eq. 7.24, we again follow the two strategies presented in section 7.2. Of the two, the second holds the strange quark mass fixed as a function of the light quark mass and is therefore the natural choice for this analysis. We still use strategy 1 as a cross check to estimate systematic effects from the chiral extrapolation.

Strange quark mass from strategy 2

The hopping parameter of the strange quark κ_s is a non-trivial function of κ_1 , defined in strategy 2 as

$$\kappa_s = s(\kappa_1, \mu_s), \quad (7.26)$$

with $s(\kappa_1, \mu)$ given in eq. 7.17. Its numerical determination as well as the determination of μ_s have been explained in section 7.2.2. The resulting values of κ_s are listed in Table 7.1. Expressing M_s in units of f_K we eliminate Z_A and get

$$\frac{M_s}{f_{K,\text{phys}}} = \frac{M}{\bar{m}(L)} \times \frac{1}{Z_P(L)} [1 + (\tilde{b}_A - \tilde{b}_P)\mu_s] \frac{\mu_s}{F_{K,\text{phys}}^{\text{bare}}}, \quad (7.27)$$

with $F_{K,\text{phys}}^{\text{bare}} = F_{K,\text{phys}}/Z_A$. The second factor is $O(a)$ improved, if we neglect, as before, a tiny correction $(\bar{b}_A - \bar{b}_P)am_{\text{sea}}$ (see Appendix 9).

Strange quark mass from strategy 1

Within this strategy, it is most natural to determine the combination $M_s + M_{\text{light}}$, the sum of strange and light quark mass, since this combination is kept fixed at lowest order in chiral perturbation theory along the trajectory defined by eq. (7.2). The first order corrections are easily incorporated from [110] such that we arrive

7.4 Determination of the strange quark mass

after renormalization as in eq. (7.27) at

$$\frac{2m_{13}(\kappa_1, h(\kappa_1))}{Z_P f_K(\kappa_1, h(\kappa_1))} = \frac{\bar{m}_s + \hat{m}}{f_{K,\text{phys}}} \left[1 + \bar{L}_m(y_1, y_K) + \left(\alpha_{4,6} - \frac{1}{4}\right)(y_1 - y_\pi) + \mathcal{O}(y^2) \right] \quad (7.28)$$

$$\bar{L}_m(y_1, y_K) = L_m(y_1, y_K) - L_m(y_\pi, y_K), \quad \alpha_{4,6} = 3\alpha_4 - 4\alpha_6, \quad (7.29)$$

$$L_m(y_1, y_K) = -\left(y_K - \frac{3}{8}y_1\right) \log(2y_K/y_1 - 1) - y_K \log(y_1), \quad (7.30)$$

which we can use to extract $(M_s + M_{\text{light}})/f_{K,\text{phys}}$ and the combination of low energy constants $\alpha_{4,6}$. Removing the contribution of the average light quark mass M_{light} amounts to multiplying by a correction factor $M_s = (M_s + M_{\text{light}})(1 - \rho)$, where ρ is a small number and can therefore be incorporated by its lowest order chiral perturbation theory estimate

$$\rho \equiv \frac{M_{\text{light}}}{M_s + M_{\text{light}}} \approx \frac{m_\pi^2}{2m_K^2} = 0.037. \quad (7.31)$$

Because of this last approximation, we prefer the determination of M_s from strategy 2 and use the one here just as a consistency check.

7.4.1 Strange quark mass in the continuum limit

For strategy 2, the strange quark mass is already at physical light quark masses by definition. For strategy 1, the extrapolation follows the same principles as before: we neglect cut-off effects in the NLO terms of the chiral expansion. The corresponding fit to the data is displayed in Fig. 7.5 on the left, which demonstrates that this assumption holds well within the statistical accuracy. Also shown for comparison is a linear extrapolation which agrees within the uncertainties with the values obtained from the ChPT formulae.

The values of \bar{m}_s/f_K for the two strategies as a function of the lattice spacings are plotted in Figure 7.5 on the right. Already at finite lattice spacing the two sets seem to be shifted with respect to another and therefore have parallel continuum extrapolations which, however, agree within uncertainties. The data fits well the assumption that only leading cut-off effects are present and we observe a correction of 8% from our value on the finest lattices. Since we prefer strategy 2 for conceptual reasons, we quote as a final result with statistical and systematic

7 The strange quark mass and the Lambda parameter for $N_f=2$ theory

uncertainties

$$\bar{m}_s/f_K = 0.678(12)(5), \quad (7.32)$$

$$M_s/f_K = 0.887(19)(7), \quad (7.33)$$

$$M_s = 138(3)(1) \text{ MeV}, \quad (7.34)$$

where we use $M/\bar{m} = 1.308(16)$ as quoted before. For reference, we also give the numbers in the $\overline{\text{MS}}$ scheme. This conversion is the only part of the computation in which we need to take recourse to perturbation theory, known in this case to four loops, which differs from the 2- and 3-loop result by only a small amount. We use the same method as described in Ref. [20], but with the new value of $\Lambda_{\overline{\text{MS}}}$ which leads us to $\bar{m}^{\overline{\text{MS}}}(2 \text{ GeV})/M = 0.740(12)$ and

$$\bar{m}_s^{\overline{\text{MS}}}(2 \text{ GeV}) = \frac{M_s}{f_K} \frac{\bar{m}^{\overline{\text{MS}}}(2 \text{ GeV})}{M} f_{K,\text{phys}} = 102(3)(1) \text{ MeV}. \quad (7.35)$$

Here also the statistical uncertainty of $\Lambda_{\overline{\text{MS}}}$ is included.

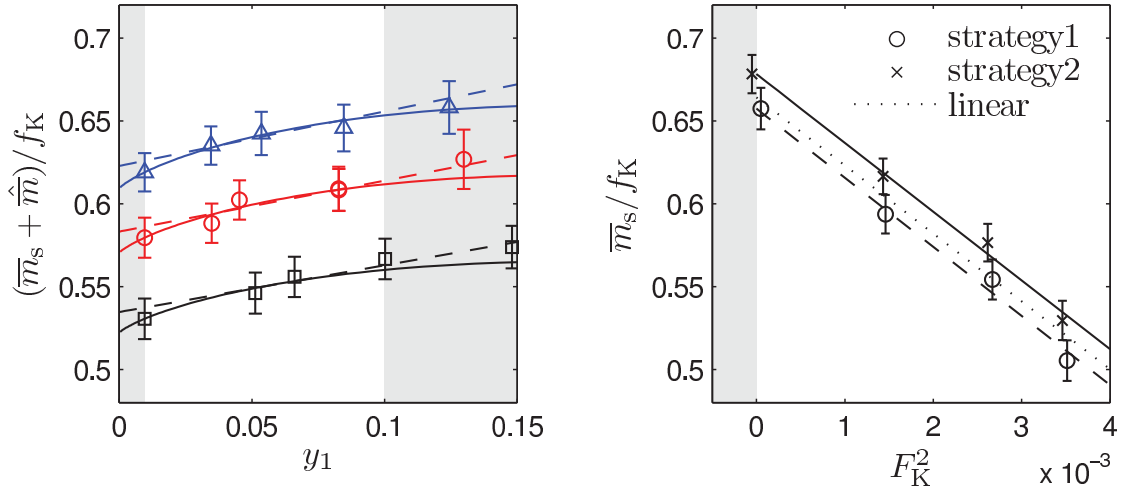


Figure 7.5: Left: Chiral extrapolation of the strange quark mass according to strategy 1. The solid line indicates a corresponding linear fit which gives a value that agrees within uncertainties at the physical point. Right: Continuum extrapolation of the strange quark mass in units of f_K for the results of the two strategies.

8 Conclusions and outlook

The aim of this work was to improve the existing determinations of the fundamental parameters of two and four flavor QCD. In $N_f = 2$ theory, we give the final result for the Lambda parameter and the strange quark mass in physical units, with a control over all possible sources of systematic errors. In $N_f = 4$ theory, we have computed the precise value of the Lambda parameter in the units of L_{\max} . A prerequisite for obtaining these results was to develop two new effective program packages, which include various modern algorithmic improvements.

In order to give a final $N_f = 2$ estimate of the fundamental QCD parameters in physical units, the continuum and chiral extrapolation had to be performed. For this to be achieved, a wide range of quark masses, lattice spacings and lattice volumes, using a single lattice formulation of the theory needed to be simulated. We have discussed in chapter 4 the practical constraints of the initial algorithm of choice for CLS consortium, DD-HMC, in completing such a task. The tool derived from it as the part of this work, MP-HMC program package, has been successfully used to simulate largest lattice extents and smallest lattice spacings in the CLS effort. Developing MP-HMC package was crucial for the continuum limit studies taken in section 7 of this work, but its application has also a broader scope. Namely, the gauge configurations produced with this code provided a valuable input for the studies within the heavy quark physics [117–120], finite temperature studies [121, 122], different scale setting methods [123], etc. Especially the set of configurations at $a = 0.0486\text{fm}$ and $m_\pi = 270\text{MeV}$ is helpful for the estimation of lattice effects for all mentioned studies involving $N_f = 2$ dynamical flavors. Simulating smaller lattice spacings than $a = 0.04\text{fm}$ with periodic boundary conditions is not possible with the HMC algorithm, due to its critical slowing down [50, 124].

The second goal of this thesis was to improve the precision of the $N_f = 4$ running coupling computation, previously done in [21]. Starting from MP-HMC and adjusting for the Schrödinger functional geometry we have developed SF-MP-HMC package, which also has high flexibility in exploiting modern computational resources. The scalability of this code is demonstrated in section 5.6.1. The computation in [21] was done on the apeNEXT machine at DESY Zeuthen over a period of one year and simulating larger lattices than $L/a = 16$ was technically impossible. With the SF-MP-HMC code we were able to obtain roughly four times more statistics in less than four months on a supercomputer HLRN and local PC cluster of HU Berlin. By completing a single scaling step from $L/a = 12$

8 Conclusions and outlook

to $L/a = 24$ in chapter 6 (cf. sections 6.5.5 and 6.5.4), we have demonstrated that with SF-MP-HMC code the simulations of larger lattices are feasible in a short period of time. It is now a matter of computational resources to perform more of these simulations and improve the determination of the running coupling even further.

With the new and more precise determination of the running coupling in chapter 6.5.5 we see a deviation from the perturbation theory predictions that is smaller than one standard deviation, while the uncertainty of the perturbation theory estimate is certainly larger than that. Although one would not expect that perturbation theory gives reliable estimate of the coupling in the low energy regime, the agreement in this case could be explained by the particular choice of the renormalization scheme. Namely, for certain definitions of the renormalization scheme, the results obtained from PT and from non-perturbative methods may agree up to the low energies and for some renormalization schemes the difference appears at much higher energy scales. As an example demonstrating the scheme dependence of the agreement of the perturbative and non-perturbative estimates of certain quantities, we can look at the non-perturbative studies of the running of the two multiplicatively renormalizable four-quark operator in several different finite volume renormalization schemes done in Ref. [125]. The comparison of the non-perturbative result with the perturbation theory estimates from [126] have shown agreement up to the high values of SF coupling in some schemes and very early deviation from the perturbative result in others. A large spread of numerical values e.g. for the two loop anomalous dimension in [126] for different SF renormalization schemes has suggested that different schemes show deviation from perturbation theory at different energy scales. There is no way to check up to which distances is the perturbative expansion in a specific renormalization scheme valid other than by doing a well controlled non-perturbative calculation.

The finite size scaling method used here for the computation of the running coupling allows for full control of the systematic errors. On the other hand, the dedicated sets of simulations have to be done for each pair of couplings used in the interpolation of continuum SSF and going higher with the SF coupling, the statistical precision decreases. Requiring certain precision of the computed SSF sets a limit on how high we can go in the coupling range and at the same time achieve the aimed precision of the SSF with a reasonable computational cost. Hence, for extending the range of simulated couplings, a new and less noisy way to define the coupling would be very welcome. A promising direction for such a definition might be following the lines of [127] and defining a running coupling from the gradient flow, as it has recently been studied in [128–130]. According to [130], the application of this definition of the coupling in SF scheme has proven to have mild cutoff effects in $N_f = 2$ and it gives high statistical precision with a modest numerical effort. Therefore, this is a good candidate for improving the $N_f = 4$ computation of the running coupling as well.

For the computation of the SF running coupling, the simulations in the finite (small) box were needed, therefore simulating Schrödinger functional was in principle not a computationally demanding task. If one wants to work with the mentioned gradient flow coupling, SF simulations with larger lattice extents become very interesting field to study. Therefore, further implementation optimization of the SF-MP-HMC code and algorithmic improvements become desirable. For instance, it would be interesting to check whether the deflated or block solver would give significant speed up of SF simulations.

Last but not least, setting the scale of the dimensionful quantities on the lattice is a crucial step in delivering QCD predictions relevant for phenomenological applications. In chapter 7, we set the scale for the $N_f = 2$ CLS simulations using kaon decay constant. To control the dependence on the light quark mass, we apply two different strategies for the chiral extrapolation. This careful procedure enables us to achieve a total error in the lattice spacing of approx 2%. Finally, we were able to complete the non-perturbative calculations of the strange quark mass and the Lambda parameter in two flavor QCD, by giving their values in physical units with relative error smaller than 7%. Performing such a procedure for the $2 + 1 + 1$ simulations remains a challenge for the following years.

Appendix A

1 Chiral representation of gamma matrices

The chiral representation for the Dirac matrices, which was used in this work, is given by

$$\gamma_k = \begin{pmatrix} 0 & -i\sigma_k \\ i\sigma_k & 0 \end{pmatrix} \quad \gamma_4 = \begin{pmatrix} 0 & \mathbf{1} \\ \mathbf{1} & 0 \end{pmatrix} \quad (1)$$

where $k = 1, 2, 3$, and $\sigma_{1,2,3}$ are the 2×2 Pauli matrices and $\mathbf{1}$ is a 2×2 unit matrix, given by

$$\sigma_1 = \begin{pmatrix} 0 & 1 \\ 1 & 0 \end{pmatrix} \quad \sigma_2 = \begin{pmatrix} 0 & -i \\ i & 0 \end{pmatrix} \quad \sigma_3 = \begin{pmatrix} 1 & 0 \\ 0 & -1 \end{pmatrix} \quad \mathbf{1} = \begin{pmatrix} 1 & 0 \\ 0 & 1 \end{pmatrix}. \quad (2)$$

They satisfy the following relations

$$\{\sigma_i, \sigma_j\} = 2\delta_{ij} \quad [\sigma_i, \sigma_j] = 2i\epsilon_{ijk}\sigma_k \quad (3)$$

where ϵ_{ijk} is the totally antisymmetric tensor. With these definitions, the Dirac matrices have properties

$$\gamma_\mu = \gamma_\mu^\dagger \quad \{\gamma_\mu, \gamma_\nu\} = 2\delta_{\mu\nu}. \quad (4)$$

The γ_5 matrix is defined as

$$\gamma_5 \equiv \gamma_1\gamma_2\gamma_3\gamma_4 \Rightarrow \gamma_5 = \begin{pmatrix} \mathbf{1} & 0 \\ 0 & -\mathbf{1} \end{pmatrix}, \quad (5)$$

thus satisfying

$$\gamma_5 = \gamma_5^\dagger \quad \gamma_5^2 = \mathbf{1}_{4 \times 4} \quad \{\gamma_\mu, \gamma_5\} = 0. \quad (6)$$

Appendix A

2 $SU(3)$ group and $su(3)$ algebra

The Lie algebra of $SU(3)$ group is denoted as $su(3)$. It consists of complex 3×3 matrices which fulfill following conditions

$$X^\dagger = -X \quad \text{and} \quad \text{Tr} X = 0. \quad (7)$$

The exponential series

$$e^X = 1 + \sum_{k=1}^{\infty} \frac{X^k}{k!} \quad (8)$$

converges to an element of $SU(3)$ group. The representation of $su(3)$ used in this work is given with the basis

$$T^a \in su(3), \quad a = 1 \dots 8, \quad (9)$$

such that

$$\text{Tr}\{T^a T^b\} = -\frac{1}{2}\delta^{ab}. \quad (10)$$

With respect to this basis, the element $X \in su(3)$ is represented as

$$X = \sum_{a=1}^8 X^a T^a, \quad (11)$$

$$X^a = -2\text{Tr}\{X T^a\} \in \mathcal{R}. \quad (12)$$

The scalar product on $su(3)$ is given by

$$(X, Y) = \sum_{a=1}^8 X^a Y^a = -2\text{Tr}\{XY\}. \quad (13)$$

Appendix B

We give in the following some analytical and technical remarks which complete the description of the algorithmic choices needed for the MP-HMC package development.

3 Inverse of Q_S via Q^{-1}

Using Shur decomposition, we can write the inverse of Q as:

$$Q^{-1} = \begin{pmatrix} Q_{ee} & Q_{eo} \\ Q_{oe} & Q_{oo} \end{pmatrix}^{-1} \quad (14)$$

$$= \begin{pmatrix} 1 & 0 \\ Q_{oo}^{-1}Q_{oe} & 1 \end{pmatrix} \begin{pmatrix} Q_{ee} - Q_{eo}Q_{oo}^{-1}Q_{oe} & 0 \\ 0 & Q_{oo} \end{pmatrix} \begin{pmatrix} 1 & -Q_{eo}Q_{oo}^{-1} \\ 0 & 1 \end{pmatrix}. \quad (15)$$

The inverse of the operator $Q_S = 1 - Q_{ee}^{-1}Q_{eo}Q_{oo}^{-1}Q_{oe}$, can be constructed from the inverted full hermitean dirac operator

$$Q = \gamma_5 D = \begin{pmatrix} Q_{ee} & Q_{eo} \\ Q_{oe} & Q_{ee} \end{pmatrix}, \quad (16)$$

in the following way

$$\{Q_S^{-1}\} = P_e Q^{-1} Q_{ee} P_e. \quad (17)$$

With some modifications, this result can be used to construct the inverse of the symmetrically preconditioned operator with a shift in mass: $W = Q_S + \rho$. Let us introduce an auxiliary operator:

$$\tilde{Q} = \begin{pmatrix} X_{ee} & Q_{eo} \\ Q_{oe} & Q_{ee} \end{pmatrix}, \quad (18)$$

Appendix B

where X_{ee} is an arbitrary operator acting in the set of even points only. Using Shur decomposition, we can write the inverse of \tilde{Q} as

$$\tilde{Q}^{-1} = \begin{pmatrix} X_{ee} & Q_{eo} \\ Q_{oe} & Q_{oo} \end{pmatrix}^{-1} \quad (19)$$

$$= \begin{pmatrix} 1 & 0 \\ Q_{oo}^{-1}Q_{oe} & 1 \end{pmatrix} \begin{pmatrix} X_{ee} - Q_{eo}Q_{oo}^{-1}Q_{oe} & 0 \\ 0 & Q_{oo} \end{pmatrix} \begin{pmatrix} 1 & -Q_{eo}Q_{oo}^{-1} \\ 0 & 1 \end{pmatrix}. \quad (20)$$

By applying projections to the even points from left and right, we obtain somewhat more general expression than (4.17):

$$(X_{ee} - Q_{eo}Q_{oo}^{-1}Q_{oe})^{-1} = P_e \tilde{Q}^{-1} P_e \quad (21)$$

$$(Q_{ee}^{-1}X_{ee} - Q_{ee}^{-1}Q_{eo}Q_{oo}^{-1}Q_{oe})^{-1} = P_e \tilde{Q}^{-1} Q_{ee} P_e$$

and appropriate choice of:

$$X_{ee} = (1 + \rho)X_{ee} \quad (22)$$

gives us exactly the wanted inverse

$$\begin{aligned} W^{-1} &= (Q_S + \rho)^{-1} \\ &= (1 + \rho - Q_{ee}^{-1}Q_{eo}Q_{oo}^{-1}Q_{oe})^{-1} \\ &= P_e \tilde{Q}^{-1} Q_{ee} P_e. \end{aligned} \quad (23)$$

4 Hasenbusch preconditioning for $N_{PF} = 3$ pseudofermions

In case $N_{PF} = 3$ we have:

$$\begin{aligned} \det Q_S^\dagger Q_S &= \det\{W_0 W_0^\dagger\} \det\{[W_0^{-1}W_1][W_0^{-1}W_1]^\dagger\} \det\{[W_1^{-1}W_2][W_1^{-1}W_2]^\dagger\} \\ &\propto \int D\phi_0^\dagger D\phi_0 D\phi_1^\dagger D\phi_1 D\phi_2^\dagger D\phi_2 e^{-\sum_{i=1}^3 S_{PF_i}} \\ S_{PF_0} &= \phi_0^\dagger (W_0 W_0^\dagger)^{-1} \phi_0 \\ S_{PF_1} &= \phi_1^\dagger ([W_0^{-1}W_1][W_0^{-1}W_1]^\dagger)^{-1} \phi_1 \\ S_{PF_2} &= \phi_2^\dagger ([W_1^{-1}W_2][W_1^{-1}W_2]^\dagger)^{-1} \phi_2, \end{aligned} \quad (24)$$

5 Run parameters of the $N_f=2$ ensembles produced with DD- and MP-HMC

where

$$W_0 = Q_S + \rho_0, \quad (25)$$

$$W_1 = Q_S + \rho_1, \quad (26)$$

$$W_2 = Q_S, \quad \rho_0 > \rho_1. \quad (27)$$

The expression for S_{PF_0} is exactly the same as the one of S_{PF_1} in the previous section, therefore the variation has the same form. Let us compute the variation of S_{PF_1} :

$$\begin{aligned} \delta S_{PF_1} &= \phi_1^\dagger \delta \{ W_0^\dagger W_1^{\dagger-1} W_1^{-1} W_0 \} \phi_1 \\ &= \phi_1^\dagger \delta \{ (W_1 + \Delta\rho)^\dagger W_1^{\dagger-1} W_1^{-1} (W_1 + \Delta\rho W_1) \} \phi_1 \\ &= \phi_1^\dagger \delta \{ ((1 + \Delta\rho W_1^{-1})^\dagger (1 + \Delta\rho W_1^{-1})) \} \phi_1 \\ &= \phi_1^\dagger \delta \{ (1 + \rho Q_S^{-1})^\dagger (1 + \rho Q_S^{-1}) \} \phi_1 \\ &= \phi_1^\dagger [(1 + \rho Q_S^{-1})^\dagger \delta \{ (1 + \rho Q_S^{-1}) \} + H.c.] \phi_1 \\ &= \phi_1^\dagger [(1 + \rho Q_S^{\dagger-1}) \rho \delta \{ Q_S^{-1} \} + H.c.] \phi_1. \end{aligned}$$

5 Run parameters of the $N_f = 2$ ensembles produced with DD- and MP-HMC

Appendix B

id	block	R_{active}	τ	N_0	N_1	N_2	acc. rate	MD time
A3	8^4	0.37	2	4	5	125	0.91	8030
A4	8^4	0.37	2	4	5	150	0.85	8090
E5f	8^4	0.37	0.5	4	5	22	0.87	16000
E5g	8^4	0.37	4	4	5	176	0.83	16180
F6	8^4	0.37	2	4	5	260	0.89	4800
F7a	8^4	0.37	2	4	5	350	0.84	5600
F7b	8^4	0.37	2	4	5	350	0.87	4000
N4	$8^2 12^2$	0.44	0.5	4	5	24	0.88	3700
N5	$8^2 12^2$	0.44	0.5	4	5	24	0.87	3800

Table 1: Parameters of the DD-HMC algorithm for the ensembles used in this thesis. We give the HMC block size, the corresponding ratio of active links R_{active} , the trajectory length, the (relative) step sizes of the gauge, block fermion and global fermion force. This is followed by the measured acceptance rate and the total statistics after thermalization. The table is taken over from Ref. [24].

id	κ_1	κ_2	τ	N_0	N_1	N_2	N_3	acc. rate	MD time
A5c	0.135887	0.134250	2	9	1	1	32	0.93	1160
A5d	0.135887	0.134250	2	9	1	1	32	0.92	1700
N6	0.136552	0.133857	2	9	1	1	16	0.84	4000
O7	0.136550	0.135000	2	9	1	2	16	0.83	4000

Table 2: Parameters of the MP-HMC algorithm for the ensembles used in this thesis. The κ_i parametrize the preconditioning masses and are followed by the trajectory length and the (relative) step numbers per trajectory. Also the acceptance rate and the statistics after thermalization are given. The table is taken over from Ref. [24].

Appendix C

6 Limits for the tuning of the PCAC mass

The limits for the tuning of am_1 (as discussed in Section 6.4.1) are given in Tables 3-5.

β	$\bar{g}^2(L)$	$am_1(L)$	$\Delta_{stat}\bar{g}_{old}^{-2}(2L)$	$am_1^{max}(L)$	$am_1^{max}(L)(1-loop)$
5.25	2.749 (13)	-0.00005 (16)	0.0035	0.0012	0.0009
5.55	2.3507(92)	0.00110 (13)	0.0035	0.0012	0.0009
5.85	2.0865(71)	0.00053 (11)	0.0036	0.0012	0.0009
6.45	1.6948(46)	-0.000294(94)	0.0037	0.0013	0.0010
7.05	1.4361(32)	0.000488(78)	0.0033	0.0013	0.0010
7.65	1.2500(24)	0.000437(69)		0.0010	0.0009
8.25	1.1025(18)	0.000435(62)	0.0034	0.0014	0.0010
8.85	0.9908(14)	0.000154(57)		0.0010	0.0009
9.45	0.8975(12)	0.000237(51)	0.0034	0.0012	0.0010

Table 3: Values of \bar{g}^2 and am_1 from old $L/a = 6$ simulations are given. The last column denotes the required limit on am_1 such that the limit given in section 6.4.1 is fulfilled.

7 Tuning of the κ_{crit} on the new parameter sets

We give in Figure the tuning of the kappa critical (of $1/\kappa$) as the function of PCAC quark mass. As a guideline for the starting simulation we use the interpolation formula given in [95]. This fit is based on the experience of the non-perturbative c_{SW} determination in [104] and reads

$$\kappa_c = 1/8 + \kappa_c^{(1)} g_0^2 + 0.000129 g_0^4 + 0.00747 g_0^2 - 0.007716 g_0^8 + 0.002748 g_0^{10}, \quad (28)$$

Appendix C

β	$\bar{g}^2(L)$	$am_1(L)$	$\Delta_{stat}\bar{g}_{old}^{-2}(2L)$	$am_1^{max}(L)$	$am_1^{max}(L)(1\text{-loop})$
5.0	3.638 (34)	0.00037 (14)		0.0008	0.0005
5.44	2.705 (16)	0.000640(83)	0.0035	0.0009	0.0006
5.88	2.225 (11)	0.000306(66)	0.0054	0.0014	0.0010
6.32	1.8728(77)	0.000288(57)	0.0049	0.0013	0.0010
6.76	1.6319(56)	0.000748(58)	0.0046	0.0012	0.0010
7.2	1.4364(42)	0.000041(44)		0.0008	0.0006
7.64	1.3046(35)	0.000233(40)	0.0045	0.0012	0.0010
8.08	1.1852(29)	0.000069(38)		0.0008	0.0006
8.52	1.0886(24)	0.000328(36)	0.0048	0.0012	0.0010
8.96	1.0034(20)	0.000368(33)		0.0008	0.0007
9.4	0.9308(17)	0.000284(32)	0.0048	0.0013	0.0011

Table 4: Values of \bar{g}^2 and am_1 from old $L/a = 8$ simulations are given. The last column denotes the required limit on am_1 such that the limit given in section 6.4.1 is fulfilled.

β	$\bar{g}^2(L)$	$am_1(L)$	$\Delta_{stat}\bar{g}_{max}^{-2}(2L)$	$am_1^{max}(L)(\text{tree})$
5.25	3.635 (46)	0.000929(56)	0.003	0.00052

Table 5: Values of \bar{g}^2 and am_1 from the preliminary set of $L/a = 12$ simulations are given. The last column denotes the required limit on am_1 such that the limit given in section 6.4.1 is fulfilled.

7 Tuning of the kappa critical on the new parameter sets

for $0 \leq g_0^2 \leq 1.2$. For each parameter set we perform two more simulations and obtain the κ_{crit} from the linear interpolation and additionally check if the obtained κ_{crit} satisfies the bound on the PCAC mass given in section 6.4.1. For the results presented in Chapter 6 only the $\beta = 9.4$ is further used, but we give here the corresponding procedure for different values of the gauge coupling considered.

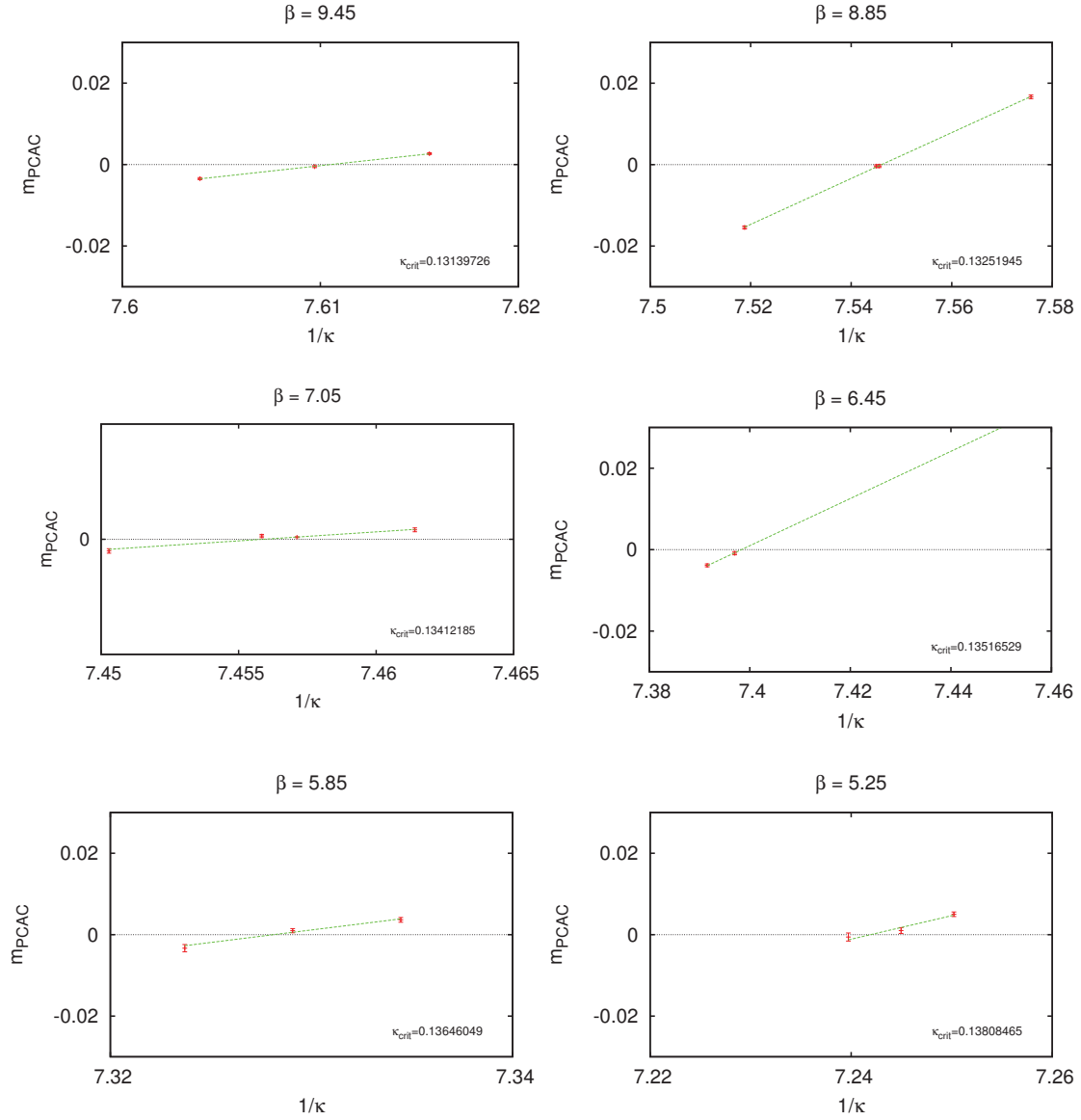


Figure 1: Tuning of the kappa critical for L=12 lattices.

Appendix D

8 Error analysis

8.1 Autocorrelations

The effect of the autocorrelations of the Monte Carlo data has been taken into account in the error analysis following the procedure from Ref. [113]. In brief, for all observables $F = F(a_1, \dots, a_n)$, functions of expectation values $a_i = \langle A_i \rangle$ of primary observables A_i , we compute an estimator of the autocorrelation function

$$\Gamma_F(t) = \sum_{i,j} f_i(\vec{a}) f_j(\vec{a}) \langle (A_i(t) - a_i)(A_j(0) - a_j) \rangle \quad (29)$$

where $f_i = \partial_i F(\vec{a})$. The argument t indicates the Monte Carlo time. The integrated autocorrelation time is then

$$\tau_{\text{int}}(F) = \frac{1}{2} + \sum_{t=1}^{\infty} \frac{\Gamma_F(t)}{\Gamma_F(0)} . \quad (30)$$

which then enters the statistical error of the observable σ_F from N measurements

$$\sigma_F^2 = 2 \frac{\tau_{\text{int}}(F)}{N} \Gamma_F(0) . \quad (31)$$

The sum in eq. (30) is normally truncated at a “window” W [114] which balances the statistical uncertainty due to the limited sample size and the systematic error coming from neglecting the tail for $t > W$. The value of W is determined from the measurement of $\rho_F(t) = \Gamma_F(t)/\Gamma_F(0)$ alone and for each F separately.

8.2 Autocorrelation function of the SF coupling

For the estimation of the autocorrelations in the computation of the running coupling for each data set analysed in section 6, we apply previously described procedure. To be on the safe side, instead of taking the standard window defined with $S_\tau = 2.0$ (according to [113]), we use in our analysis a rather conservative choice of $S_\tau = 5.0$. The examples of the autocorrelation function for $L = 12$ and $L = 24$ data are shown in Figure 2.

Appendix D

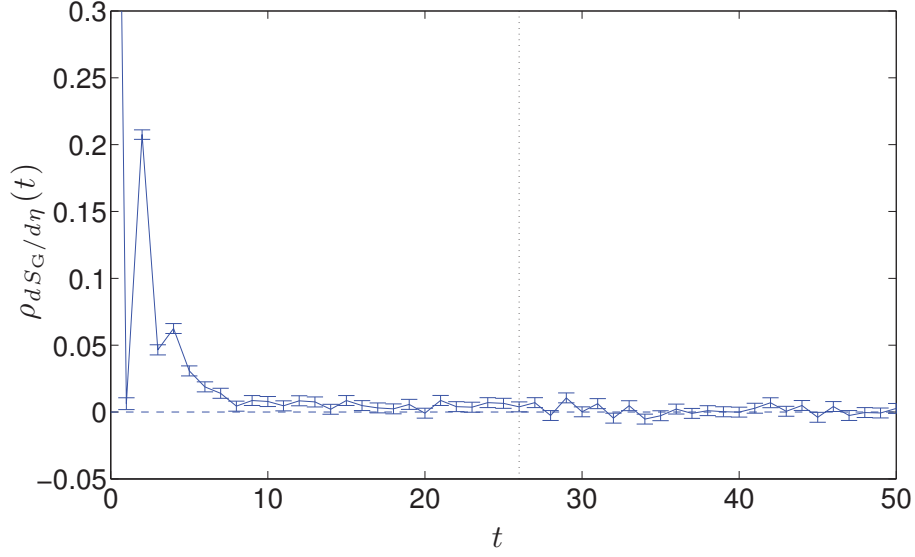


Figure 2: Autocorrelation function of $dS_G/d\eta$ for the $L=12$ lattice. The dashed line gives a window. The standard method of ref. [113] gives a window $W = W_l$ and $\tau_{\text{int}} = 0.7$, compared to $\tau_{\text{int}} = 4$.

8.3 Improved error analysis of lattice QCD simulations

Neglecting the tail above W leads — at least on average — to an underestimation of τ_{int} and the statistical error of the observable. It is particularly problematic in the presence of slow modes of the Monte Carlo transition matrix which only couple weakly to the observable in question. To account for them, in the analysis of $N_f = 2$ data in section 7, we use the method outlined in ref. [50], estimating their time constants from observables to which the slow modes couple strongly. Using them, we can then estimate the tails of the autocorrelation functions of the observables we are interested in and arrive at a more conservative error estimate.

Experience tells us that for small lattice spacing the topological charge is particularly sensitive to slow modes[50, 131], for which we use the field theoretical definition after smoothing the field by the Wilson flow[127] integrated up to t_0 . Actually, only the square of the charge needs to be considered, because we are only interested in parity even observables. Unfortunately we are not in the position to accurately determine its autocorrelation time for most of our ensembles. We therefore combine the scaling laws found in pure gauge theory[50] with the measurement for our high statistics ensembles E5 and arrive at the estimate

$$\tau_{\text{exp}}(\beta) = 200 \frac{c_\tau e^{7(\beta-5.5)}}{R_{\text{active}}}, \quad (32)$$

with $c_\tau = 2$ for trajectories of length $\tau = 0.5$ and $c_\tau = 1$ for $\tau = 2$ and 4. The values of R_{active} can be found in Table 1 for the DD-HMC algorithm and is equal to one for the MP-HMC.

An example of the procedure is given in Fig. 3, showing the autocorrelation function of the kaon decay constant f_K on the O7 ensemble. Using the standard procedure[113, 114], the sum in eq. (30) is truncated at the window W_l from which we would get $\tau_{\text{int}} = 0.7$. When the contribution of the tail is included, the improved estimate gives $\tau_{\text{int}} = 4$, which translates to a more than doubled error estimate.

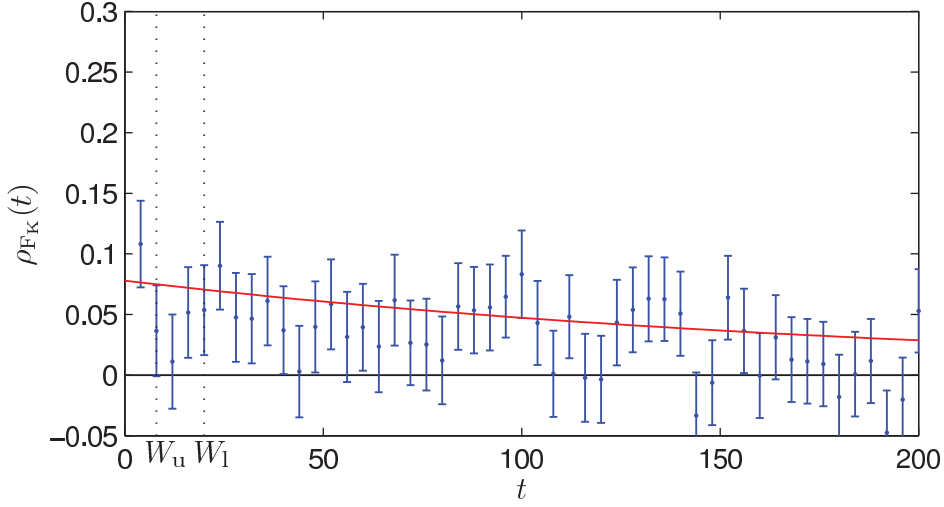


Figure 3: Autocorrelation function of f_K for the O7 lattice. The line gives our estimate for its tail. The standard method of ref. [113] gives a window $W = W_l$ and $\tau_{\text{int}} = 0.7$, compared to $\tau_{\text{int}} = 4$ including the tail contribution which we add from $W = W_u$, or more than a factor two in the error of the observable.

9 Observables used in chapter 7

The computation of our pseudoscalar observables is based on two-point functions of the pseudoscalar density and the time component of the axialvector current. At a fixed κ_{sea} they are constructed from two valence quarks r and s

$$f_{\text{PP}}^{rs}(x_0) = -a^3 \sum_{\vec{x}} \langle P^{rs}(x) P^{sr}(0) \rangle \quad (33)$$

$$f_{\text{AP}}^{rs}(x_0) = -a^3 \sum_{\vec{x}} \langle A_0^{rs}(x) P^{sr}(0) \rangle \quad (34)$$

Appendix D

with $P^{rs} = \bar{\psi}_r \gamma_5 \psi_s$ and $A_0^{rs} = \bar{\psi}_r \gamma_0 \gamma_5 \psi_s$. Using the PCAC relation, average quark masses of flavors r and s can then be defined as

$$m_{rs}(x_0) = \frac{\frac{1}{2}(\partial_0 + \partial_0^*)f_{AP}(x_0) + c_A a \partial_0^* \partial_0 f_{PP}(x_0)}{2f_{PP}(x_0)}. \quad (35)$$

For sufficiently large x_0 the mass $m_{rs}(x_0)$ will have a plateau over which we can average. From its value m_{rs} the renormalized quark mass m_R^{rs} is obtained

$$m_R^{rs} = \frac{Z_A(1 + \bar{b}_A a m_{\text{sea}} + \tilde{b}_A a m_{rs})}{Z_P(1 + \bar{b}_P a m_{\text{sea}} + \tilde{b}_P a m_{rs})} m_{rs}, \quad (36)$$

with $m_{\text{sea}} = m_{12}$. We use one-loop perturbation theory for the improvement coefficients \bar{b}_A , \bar{b}_P , \tilde{b}_A and \tilde{b}_P , noting that they multiply very small terms. At this order in perturbation theory

$$\bar{b}_A = \bar{b}_P = 0, \quad (37)$$

while

$$\tilde{b}_A = 1 + 0.06167 g_0^2 \quad \text{and} \quad \tilde{b}_P = 1 + 0.06261 g_0^2 \quad (38)$$

computed from the perturbative coefficients of [132]. Here we use the updated values of the non-perturbatively determined Z_A and Z_P from [24].

Acknowledgments

I would like to express my gratitude to Prof. Ulli Wolff, for giving me the opportunity to attain my PhD in his group and to thank both U. Wolff and Rainer Sommer for advice and stimulating discussions during my PhD journey. Thank you for everything I have learned from you!

I would like to give my special thanks to Stefan Schaefer, who has guided me patiently through the first years of my PhD. I additionally kindly thank P. Frittsch, F. Knechtli, B. Leder and F. Virotta for our collaboration on the two flavor project, as well as to A. Athinodorou, J. Heitger, H. Simma and C. Wittemeier for providing me with various crosschecks and input needed for the SF code.

Thanks to Andreas Athinodorou for the valuable discussions and constant encouragement. Muchas gracias to Alberto Ramos for the critical reading of a part of this thesis, for inspiring debates and all OMBs. In the final phase of this work, I benefited from a number of useful discussions on Schrödinger Functional with Stefan Sint. Many thanks! I am also thankful to Carsten Urbach for R-project tips & tricks, scripts and all the useful and friendly advice. Moreover, I am honored to be graced by the help of Marina Peneva in correcting my clumsy English throughout the whole thesis.

The completion of this work would not be possible without the support of the *German Science Foundation (DFG)* under the grants GRK1504 and SFB/TR9-03. I am additionally grateful to Martin zur Nedden for his engagement in the doctoral research school "*Mass, spectrum, symmetry*", from which I benefited greatly. The writing up of this thesis was finalized at the *University of Southampton*, and I would like to thank my new colleagues for their patience during those months. Furthermore, I am thankful to Prof. Michael Müller-Preussker for accepting to chair the defense committee, as well as Prof. L. Lellouch for investing his time in refereeing the thesis.

I am grateful to all participants of *DS (2009-2012)* for their involvement and the exciting discussions. Many thanks to A. Ramos and F. Bernardoni for waking up the Wednesday meetings, despite the fact they made me fatter. Thanks to all my colleagues in *DESY Zeuthen* and at *HU Berlin*, especially to Alberto, Andreas, Elenita, Fabio, Filippo, Jen and Petra for all the interesting discussions and joint

Acknowledgments

scientific extracurriculars. Last but not least, thanks to the whole SBP team for making me miss Berlin even more since I have been away.

Every adventure has its downfalls, though, and I would not have made through some of them without Julia Dobbert and Lazar Krstić. Thank you for inspiring me to fight for my goals. I would also like to thank Julia Dobbert for encouraging my participation at the *FINCA mentoring program* and workshops in 2010, that has evolved to my membership in *Kommission für Frauenförderung* in 2011, whose members I would like to thank for their engagement and cooperation.

I cannot thank enough Marko, Iva and Bane for being there for me and loving me all the way. Thank you so much Andja, Jovana, Kristina, Magdalena, Maja, Marija and Milanče for sharing the most beautiful as well as most difficult moments of the past years with me, and for encouraging me throughout this experience. I would like to express my enormous thanks to the whole *YelloV Team Berlin*, for generously accepting me in their amazing team, and making Berlin my real home. Vielen Dank! Thanks to Ana, Andrej, Bane, Bojana², Bratislav, Gaga, Jeca, Jovana, Kaća, Mara, Nataša, Nenad², Šef, Stefan, and Žarko for providing me with an absolutely perfect roundup of my PhD. Finally, I would like to thank my aunt Milka, together with my parents Ivanka and Marinko for all their love and support. Hvala vam od srca!

Bibliography

- [1] Georges Aad et al. Observation of a new particle in the search for the Standard Model Higgs boson with the ATLAS detector at the LHC. *Phys.Lett.*, B716:1–29, 2012. doi: 10.1016/j.physletb.2012.08.020.
- [2] Serguei Chatrchyan et al. Observation of a new boson at a mass of 125 GeV with the CMS experiment at the LHC. *Phys.Lett.*, B716:30–61, 2012. doi: 10.1016/j.physletb.2012.08.021.
- [3] Rainer Sommer. Nonperturbative renormalization of QCD. hep-ph/9711243, 1997.
- [4] William E. Caswell. Asymptotic Behavior of Nonabelian Gauge Theories to Two Loop Order. *Phys.Rev.Lett.*, 33:244, 1974. doi: 10.1103/PhysRevLett.33.244.
- [5] D.R.T. Jones. Two Loop Diagrams in Yang-Mills Theory. *Nucl.Phys.*, B75: 531, 1974. doi: 10.1016/0550-3213(74)90093-5.
- [6] D.J. Gross and Frank Wilczek. Ultraviolet Behavior of Nonabelian Gauge Theories. *Phys.Rev.Lett.*, 30:1343–1346, 1973. doi: 10.1103/PhysRevLett.30.1343.
- [7] H. David Politzer. Reliable Perturbative Results for Strong Interactions? *Phys.Rev.Lett.*, 30:1346–1349, 1973. doi: 10.1103/PhysRevLett.30.1346.
- [8] Kenneth G. Wilson. Confinement of Quarks. *Phys.Rev.*, D10:2445–2459, 1974. doi: 10.1103/PhysRevD.10.2445.
- [9] Karl Jansen, Chuan Liu, Martin Luscher, Hubert Simma, Stefan Sint, et al. Nonperturbative renormalization of lattice QCD at all scales. *Phys.Lett.*, B372:275–282, 1996. doi: 10.1016/0370-2693(96)00075-5.
- [10] G. Martinelli, C. Pittori, Christopher T. Sachrajda, M. Testa, and A. Vladikas. A General method for nonperturbative renormalization of lattice operators. *Nucl.Phys.*, B445:81–108, 1995. doi: 10.1016/0550-3213(95)00126-D.

Bibliography

- [11] S. Durr, Z. Fodor, C. Hoelbling, S.D. Katz, S. Krieg, et al. Lattice QCD at the physical point: light quark masses. *Phys.Lett.*, B701:265–268, 2011. doi: 10.1016/j.physletb.2011.05.053.
- [12] S. Durr, Z. Fodor, C. Hoelbling, S.D. Katz, S. Krieg, et al. Lattice QCD at the physical point: Simulation and analysis details. *JHEP*, 1108:148, 2011. doi: 10.1007/JHEP08(2011)148.
- [13] C.T.H. Davies, C. McNeile, K.Y. Wong, E. Follana, R. Horgan, et al. Precise Charm to Strange Mass Ratio and Light Quark Masses from Full Lattice QCD. *Phys.Rev.Lett.*, 104:132003, 2010. doi: 10.1103/PhysRevLett.104.132003.
- [14] C. McNeile, C.T.H. Davies, E. Follana, K. Hornbostel, and G.P. Lepage. High-Precision c and b Masses, and QCD Coupling from Current-Current Correlators in Lattice and Continuum QCD. *Phys.Rev.*, D82:034512, 2010. doi: 10.1103/PhysRevD.82.034512.
- [15] J. Beringer et al. Review of Particle Physics (RPP). *Phys.Rev.*, D86:010001, 2012. doi: 10.1103/PhysRevD.86.010001.
- [16] ALPHA Collaboration. URL <http://www-zeuthen.desy.de/alpha/>.
- [17] Martin Luscher, Rainer Sommer, Peter Weisz, and Ulli Wolff. A Precise determination of the running coupling in the SU(3) Yang-Mills theory. *Nucl.Phys.*, B413:481–502, 1994. doi: 10.1016/0550-3213(94)90629-7.
- [18] Stefano Capitani, Martin Luscher, Rainer Sommer, and Hartmut Wittig. Nonperturbative quark mass renormalization in quenched lattice QCD. *Nucl.Phys.*, B544:669–698, 1999. doi: 10.1016/S0550-3213(98)00857-8.
- [19] Michele Della Morte et al. Computation of the strong coupling in QCD with two dynamical flavors. *Nucl.Phys.*, B713:378–406, 2005. doi: 10.1016/j.nuclphysb.2005.02.013.
- [20] Michele Della Morte et al. Non-perturbative quark mass renormalization in two-flavor QCD. *Nucl.Phys.*, B729:117–134, 2005. doi: 10.1016/j.nuclphysb.2005.09.028.
- [21] Fatih Tekin, Rainer Sommer, and Ulli Wolff. The Running coupling of QCD with four flavors. *Nucl.Phys.*, B840:114–128, 2010. doi: 10.1016/j.nuclphysb.2010.07.002.
- [22] Martin Luscher, Peter Weisz, and Ulli Wolff. A Numerical method to compute the running coupling in asymptotically free theories. *Nucl.Phys.*, B359: 221–243, 1991. doi: 10.1016/0550-3213(91)90298-C.

- [23] Martin Luscher, Rainer Sommer, Ulli Wolff, and Peter Weisz. Computation of the running coupling in the SU(2) Yang-Mills theory. *Nucl.Phys.*, B389: 247–264, 1993. doi: 10.1016/0550-3213(93)90292-W.
- [24] Patrick Fritzsche, Francesco Knechtli, Bjorn Leder, Marina Marinkovic, Stefan Schaefer, et al. The strange quark mass and Lambda parameter of two flavor QCD. *Nucl.Phys.*, B865:397–429, 2012. doi: 10.1016/j.nuclphysb.2012.07.026.
- [25] S. Alekhin, J. Blumlein, and S. Moch. Parton Distribution Functions and Benchmark Cross Sections at NNLO. *Phys.Rev.*, D86:054009, 2012. doi: 10.1103/PhysRevD.86.054009.
- [26] A.D. Martin, W.J. Stirling, R.S. Thorne, and G. Watt. Uncertainties on $\alpha(S)$ in global PDF analyses and implications for predicted hadronic cross sections. *Eur.Phys.J.*, C64:653–680, 2009. doi: 10.1140/epjc/s10052-009-1164-2.
- [27] Konrad Osterwalder and Robert Schrader. Axioms for euclidean green’s functions. *Commun.Math.Phys.*, 31:83–112, 1973. doi: 10.1007/BF01645738.
- [28] Konrad Osterwalder and Robert Schrader. Axioms for Euclidean Green’s Functions. 2. *Commun.Math.Phys.*, 42:281, 1975. doi: 10.1007/BF01608978.
- [29] Christof Gattringer and Christian B. Lang. Quantum chromodynamics on the lattice. *Lect.Notes Phys.*, 788:1–211, 2010. doi: 10.1007/978-3-642-01850-3.
- [30] Thomas DeGrand and Carleton E. Detar. Lattice methods for quantum chromodynamics. *New Jersey, USA: World Scientific*, 345 p, 2006.
- [31] J. Smit. Introduction to quantum fields on a lattice: A robust mate. *Cambridge Lect.Notes Phys.*, 15:1–271, 2002.
- [32] H.J. Rothe. Lattice gauge theories: An Introduction. *World Sci.Lect.Notes Phys.*, 43:1–381, 1992.
- [33] M. Creutz. Quarks, gluons and lattices. Cambridge, Uk: Univ. Pr. 169 P. (Cambridge Monographs On Mathematical Physics), 1983.
- [34] Martin Luscher. Computational Strategies in Lattice QCD. arXiv:1002.4232 [hep-lat], 2010.
- [35] Martin Luscher. Advanced lattice QCD. hep-lat/9802029, 1998.
- [36] Rajan Gupta. Introduction to lattice QCD: Course. hep-lat/9807028, 1997.

Bibliography

- [37] Holger Bech Nielsen and M. Ninomiya. No Go Theorem for Regularizing Chiral Fermions. *Phys.Lett.*, B105:219, 1981. doi: 10.1016/0370-2693(81)91026-1.
- [38] Holger Bech Nielsen and M. Ninomiya. Absence of Neutrinos on a Lattice. 1. Proof by Homotopy Theory. *Nucl.Phys.*, B185:20, 1981. doi: 10.1016/0550-3213(81)90361-8.
- [39] Holger Bech Nielsen and M. Ninomiya. Absence of Neutrinos on a Lattice. 2. Intuitive Topological Proof. *Nucl.Phys.*, B193:173, 1981. doi: 10.1016/0550-3213(81)90524-1.
- [40] K. Symanzik. Continuum Limit and Improved Action in Lattice Theories. 1. Principles and ϕ^4 Theory. *Nucl.Phys.*, B226:187, 1983. doi: 10.1016/0550-3213(83)90468-6.
- [41] K. Symanzik. Continuum Limit and Improved Action in Lattice Theories. 2. $O(N)$ Nonlinear Sigma Model in Perturbation Theory. *Nucl.Phys.*, B226:205, 1983. doi: 10.1016/0550-3213(83)90469-8.
- [42] Martin Luscher, Stefan Sint, Rainer Sommer, and Peter Weisz. Chiral symmetry and $O(a)$ improvement in lattice QCD. *Nucl.Phys.*, B478:365–400, 1996. doi: 10.1016/0550-3213(96)00378-1.
- [43] Martin Luscher, Stefan Sint, Rainer Sommer, Peter Weisz, and Ulli Wolff. Nonperturbative $O(a)$ improvement of lattice QCD. *Nucl.Phys.*, B491:323–343, 1997. doi: 10.1016/S0550-3213(97)00080-1.
- [44] Karl Jansen and Rainer Sommer. $O(\alpha)$ improvement of lattice QCD with two flavors of Wilson quarks. *Nucl.Phys.*, B530:185–203, 1998. doi: 10.1016/S0550-3213(98)00396-4.
- [45] N. Yamada et al. Non-perturbative $O(a)$ -improvement of Wilson quark action in three-flavor QCD with plaquette gauge action. *Phys.Rev.*, D71:054505, 2005. doi: 10.1103/PhysRevD.71.054505.
- [46] Yu-bing Luo. On-shell improved lattice QCD with staggered fermions. *Phys.Rev.*, D57:265–275, 1998. doi: 10.1103/PhysRevD.57.265.
- [47] T. van Ritbergen, J.A.M. Vermaseren, and S.A. Larin. The Four loop beta function in quantum chromodynamics. *Phys.Lett.*, B400:379–384, 1997. doi: 10.1016/S0370-2693(97)00370-5.
- [48] O.V. Tarasov, A.A. Vladimirov, and A. Yu. Zharkov. The Gell-Mann-Low Function of QCD in the Three Loop Approximation. *Phys.Lett.*, B93:429–432, 1980. doi: 10.1016/0370-2693(80)90358-5.

- [49] Achim Bode, Peter Weisz, and Ulli Wolff. Two loop computation of the Schrodinger functional in lattice QCD. *Nucl.Phys.*, B576:517–539, 2000. doi: 10.1016/S0550-3213(00)00187-5.
- [50] Stefan Schaefer, Rainer Sommer, and Francesco Virota. Critical slowing down and error analysis in lattice QCD simulations. *Nucl.Phys.*, B845:93–119, 2011. doi: 10.1016/j.nuclphysb.2010.11.020.
- [51] S. Duane, A.D. Kennedy, B.J. Pendleton, and D. Roweth. Hybrid Monte Carlo. *Phys.Lett.*, B195:216–222, 1987. doi: 10.1016/0370-2693(87)91197-X.
- [52] David J.E. Callaway and Aneesur Rahman. The microcanonical ensemble: a new formulation of lattice gauge theory. *Phys.Rev.Lett.*, 49:613, 1982. doi: 10.1103/PhysRevLett.49.613.
- [53] David J.E. Callaway and Aneesur Rahman. Lattice gauge theory in microcanonical ensemble. *Phys.Rev.*, D28:1506, 1983. doi: 10.1103/PhysRevD.28.1506.
- [54] I.P. Omelyan, I.M. Mryglod, and R. Folk. Symplectic analytically integrable decomposition algorithms: classification, derivation, and application to molecular dynamics, quantum and celestial mechanics simulations, 2003. ISSN 0010-4655.
- [55] Martin Luscher and Stefan Schaefer. Lattice QCD without topology barriers. *JHEP*, 1107:036, 2011. doi: 10.1007/JHEP07(2011)036.
- [56] A.D. Kennedy, P.J. Silva, and M.A. Clark. Shadow Hamiltonians, Poisson Brackets, and Gauge Theories. arXiv:1210.6600 [hep-lat], 2012.
- [57] M.A. Clark and A.D. Kennedy. Asymptotics of Fixed Point Distributions for Inexact Monte Carlo Algorithms. *Phys.Rev.*, D76:074508, 2007. doi: 10.1103/PhysRevD.76.074508.
- [58] A.D. Kennedy and M.A. Clark. Speeding up HMC with better integrators. *PoS*, LAT2007:038, 2007.
- [59] Rainer Sommer Harvey B. Meyer. The molecular dynamics forces in simulations of nf=2 clover fermions in the schroedinger functional. DESY-Zeuthen, August 2005. ALPHA Collaboration internal notes.
- [60] C.T.H. Davies et al. High precision lattice QCD confronts experiment. *Phys.Rev.Lett.*, 92:022001, 2004. doi: 10.1103/PhysRevLett.92.022001.

Bibliography

- [61] A. Ukawa. Computational cost of full QCD simulations experienced by CP-PACS and JLQCD Collaborations. *Nucl.Phys.Proc.Suppl.*, 106:195–196, 2002. doi: 10.1016/S0920-5632(01)01662-0.
- [62] C. Urbach, K. Jansen, A. Shindler, and U. Wenger. HMC algorithm with multiple time scale integration and mass preconditioning. *Comput.Phys.Commun.*, 174:87–98, 2006. doi: 10.1016/j.cpc.2005.08.006.
- [63] K. Jansen and C. Urbach. tmLQCD: A Program suite to simulate Wilson Twisted mass Lattice QCD. *Comput.Phys.Commun.*, 180:2717–2738, 2009. doi: 10.1016/j.cpc.2009.05.016.
- [64] Martin Luscher. Lattice QCD and the Schwarz alternating procedure. *JHEP*, 0305:052, 2003. doi: 10.1088/1126-6708/2003/05/052.
- [65] Martin Hasenbusch. Speeding up the hybrid Monte Carlo algorithm for dynamical fermions. *Phys.Lett.*, B519:177–182, 2001. doi: 10.1016/S0370-2693(01)01102-9.
- [66] M. Hasenbusch and K. Jansen. Speeding up the Hybrid Monte Carlo algorithm for dynamical fermions. *Nucl.Phys.Proc.Suppl.*, 106:1076–1078, 2002. doi: 10.1016/S0920-5632(01)01933-8.
- [67] J.C. Sexton and D.H. Weingarten. Hamiltonian evolution for the hybrid Monte Carlo algorithm. *Nucl.Phys.*, B380:665–678, 1992. doi: 10.1016/0550-3213(92)90263-B.
- [68] Martin Luscher. Schwarz-preconditioned HMC algorithm for two-flavour lattice QCD. *Comput.Phys.Commun.*, 165:199–220, 2005. doi: 10.1016/j.cpc.2004.10.004.
- [69] M. Luscher. <http://luscher.web.cern.ch/luscher/dd-hmc/index.html>. DD-HMC algorithm for two-flavour lattice QCD.
- [70] Robert G. Edwards and Balint Joo. The Chroma software system for lattice QCD. *Nucl.Phys.Proc.Suppl.*, 140:832, 2005. doi: 10.1016/j.nuclphysbps.2004.11.254.
- [71] Martin Luscher and Stefan Schaefer. Lattice QCD with open boundary conditions and twisted-mass reweighting. *Comput.Phys.Commun.*, 184:519–528, 2012. doi: 10.1016/j.cpc.2012.10.003.
- [72] L. Del Debbio, Leonardo Giusti, M. Luscher, R. Petronzio, and N. Tantalo. QCD with light Wilson quarks on fine lattices. II. DD-HMC simulations and data analysis. *JHEP*, 0702:082, 2007. doi: 10.1088/1126-6708/2007/02/082.

- [73] CLS. Coordinated lattice simulations. URL <https://twiki.cern.ch/twiki/bin/view/CLS/>.
- [74] Marina Marinkovic and Stefan Schaefer. Comparison of the mass preconditioned HMC and the DD-HMC algorithm for two-flavour QCD. *PoS, LATTICE2010:031*, 2010.
- [75] S A Schwarz and Hermann Amandus Schwarz. *Gesammelte Mathematische Abhandlungen*. BiblioLife, 2009. ISBN 1113936274.
- [76] Martin Luscher. Solution of the Dirac equation in lattice QCD using a domain decomposition method. *Comput.Phys.Commun.*, 156:209–220, 2004. doi: 10.1016/S0010-4655(03)00486-7.
- [77] Martin Luscher. Local coherence and deflation of the low quark modes in lattice QCD. *JHEP*, 0707:081, 2007. doi: 10.1088/1126-6708/2007/07/081.
- [78] Martin Luscher. Deflation acceleration of lattice QCD simulations. *JHEP*, 0712:011, 2007. doi: 10.1088/1126-6708/2007/12/011.
- [79] S. Durr, Z. Fodor, C. Hoelbling, R. Hoffmann, S.D. Katz, et al. Scaling study of dynamical smeared-link clover fermions. *Phys.Rev.*, D79:014501, 2009. doi: 10.1103/PhysRevD.79.014501.
- [80] Karl Jansen and Chuan Liu. Implementation of Symanzik’s improvement program for simulations of dynamical Wilson fermions in lattice QCD. *Comput.Phys.Commun.*, 99:221–234, 1997. doi: 10.1016/S0010-4655(96)00128-2.
- [81] S. Aoki et al. Polynomial hybrid Monte Carlo algorithm for lattice QCD with odd number of flavors. *Phys.Rev.*, D65:094507, 2002. doi: 10.1103/PhysRevD.65.094507.
- [82] Rainer Sommer. A stabilized HMC. ALPHA Collaboration Internal Notes, April 2010.
- [83] K. Symanzik. Schrodinger Representation and Casimir Effect in Renormalizable Quantum Field Theory. *Nucl.Phys.*, B190:1, 1981. doi: 10.1016/0550-3213(81)90482-X.
- [84] Ulli Wolff. Monte carlo estimate of the background field coupling renormalization in the Heisenberg model. *Nucl.Phys.*, B265:537, 1986. doi: 10.1016/0550-3213(86)90172-0.
- [85] Ulli Wolff. Anomalous scale transformations and functional integrals. *Nucl.Phys.*, B265:506, 1986. doi: 10.1016/0550-3213(86)90171-9.

Bibliography

- [86] Rainer Sommer. Non-perturbative QCD: Renormalization, $O(a)$ -improvement and matching to Heavy Quark Effective Theory. 2006.
- [87] Rainer Sommer. Introduction to Non-perturbative Heavy Quark Effective Theory. *"Modern perspectives in lattice QCD"*, Les Houches, pages 517–590, August 3-28, 2010.
- [88] Stefan Sint. The Chirally rotated Schrödinger functional with Wilson fermions and automatic $O(a)$ improvement. *Nucl.Phys.*, B847:491–531, 2011. doi: 10.1016/j.nuclphysb.2011.02.002.
- [89] J. Gonzalez Lopez, K. Jansen, D.B. Renner, and A. Shindler. A quenched study of the Schroedinger functional with chirally rotated boundary conditions: non-perturbative tuning. 2012.
- [90] Martin Luscher, Rajamani Narayanan, Peter Weisz, and Ulli Wolff. The Schrodinger functional: A Renormalizable probe for nonAbelian gauge theories. *Nucl.Phys.*, B384:168–228, 1992. doi: 10.1016/0550-3213(92)90466-O.
- [91] Stefan Sint. On the Schrodinger functional in QCD. *Nucl.Phys.*, B421:135–158, 1994. doi: 10.1016/0550-3213(94)90228-3.
- [92] M. Luscher and P. Weisz. $O(a)$ improvement of the axial current in lattice QCD to one loop order of perturbation theory. *Nucl.Phys.*, B479:429–458, 1996. doi: 10.1016/0550-3213(96)00448-8.
- [93] Stefan Sint. The Schrodinger functional with chirally rotated boundary conditions. *PoS*, LAT2005:235, 2006.
- [94] APE (Arrayray Processor Experiment) Group Projects, 1984-2012,. URL http://apegate.roma1.infn.it/mediawiki/index.php/APE_tesi.
- [95] Fatih Tekin. *The strong coupling constant of QCD with four flavors*. PhD thesis, Humboldt Universität zu Berlin, 2010. URL <http://edoc.hu-berlin.de/docviews/abstract.php?id=37473>.
- [96] A. Athenodorou, M. Della Morte, H. Simma, and C. Wittemeier. Schroedinger functional correlation functions (sfcf) package. ALPHA Collaboration, 2010-2013.
- [97] Jochen Heitger. *Non-perturbative renormalization in Quantum Chromodynamics and Heavy Quark Effective Theory*. Habilitationsschrift, Westfälischen Wilhelms-Universität zu Münster, 2005.
- [98] Siegfried Bethke, Andre H. Hoang, Stefan Kluth, Jochen Schieck, Iain W. Stewart, et al. Workshop on Precision Measurements of α_s . 2011.

- [99] Stefan Sint and Rainer Sommer. The Running coupling from the QCD Schrodinger functional: A One loop analysis. *Nucl.Phys.*, B465:71–98, 1996. doi: 10.1016/0550-3213(96)00020-X.
- [100] Werner Bernreuther and Werner Wetzel. Decoupling of Heavy Quarks in the Minimal Subtraction Scheme. *Nucl.Phys.*, B197:228, 1982. doi: 10.1016/0550-3213(82)90288-7.
- [101] K.G. Chetyrkin, Johann H. Kuhn, and M. Steinhauser. RunDec: A Mathematica package for running and decoupling of the strong coupling and quark masses. *Comput.Phys.Commun.*, 133:43–65, 2000. doi: 10.1016/S0010-4655(00)00155-7.
- [102] Joyce Garden, Jochen Heitger, Rainer Sommer, and Hartmut Wittig. Precision computation of the strange quark’s mass in quenched QCD. *Nucl.Phys.*, B571:237–256, 2000. doi: 10.1016/S0550-3213(99)00714-2.
- [103] Michele Della Morte, Roland Hoffmann, and Rainer Sommer. Non-perturbative improvement of the axial current for dynamical Wilson fermions. *JHEP*, 0503:029, 2005. doi: 10.1088/1126-6708/2005/03/029.
- [104] Fatih Tekin, Rainer Sommer, and Ulli Wolff. Symanzik improvement of lattice QCD with four flavors of Wilson quarks. *Phys.Lett.*, B683:75–79, 2010. doi: 10.1016/j.physletb.2009.11.055.
- [105] Paula Perez-Rubio and Stefan Sint. Non-perturbative running of the coupling from four flavour lattice QCD with staggered quarks. *PoS, LATTICE2010*:236, 2010.
- [106] Bernd Gehrman, Juri Rolf, Stefan Kurth, and Ulli Wolff. Schrodinger functional at negative flavor number. *Nucl.Phys.*, B612:3–24, 2001. doi: 10.1016/S0550-3213(01)00363-7.
- [107] Giulia de Divitiis et al. Universality and the approach to the continuum limit in lattice gauge theory. *Nucl.Phys.*, B437:447–470, 1995. doi: 10.1016/0550-3213(94)00019-B.
- [108] Thomas Appelquist, George T. Fleming, and Ethan T. Neil. Lattice Study of Conformal Behavior in SU(3) Yang-Mills Theories. *Phys.Rev.*, D79:076010, 2009. doi: 10.1103/PhysRevD.79.076010.
- [109] Marina Marinkovic, Stefan Schaefer, Rainer Sommer, and Francesco Virotta. Strange quark mass and Lambda parameter by the ALPHA collaboration. *PoS, LATTICE2011*:232, 2011.

Bibliography

- [110] Stephen R. Sharpe. Enhanced chiral logarithms in partially quenched QCD. *Phys.Rev.*, D56:7052–7058, 1997. doi: 10.1103/PhysRevD.62.099901, 10.1103/PhysRevD.56.7052.
- [111] Tanmoy Bhattacharya, Rajan Gupta, Weonjong Lee, Stephen R. Sharpe, and Jackson M.S. Wu. Improved bilinears in lattice QCD with non-degenerate quarks. *Phys.Rev.*, D73:034504, 2006. doi: 10.1103/PhysRevD.73.034504.
- [112] Gilberto Colangelo, Stephan Durr, Andreas Juttner, Laurent Lellouch, Heinrich Leutwyler, et al. Review of lattice results concerning low energy particle physics. *Eur.Phys.J.*, C71:1695, 2011. doi: 10.1140/epjc/s10052-011-1695-1.
- [113] Ulli Wolff. Monte Carlo errors with less errors. *Comput.Phys.Commun.*, 156: 143–153, 2004. doi: 10.1016/S0010-4655(03)00467-3, 10.1016/j.cpc.2006.12.001.
- [114] Neal Madras and Alan D. Sokal. The Pivot algorithm: a highly efficient Monte Carlo method for selfavoiding walk. *J.Statist.Phys.*, 50:109–186, 1988. doi: 10.1007/BF01022990.
- [115] A. Roessl. Pion kaon scattering near the threshold in chiral SU(2) perturbation theory. *Nucl.Phys.*, B555:507–539, 1999. doi: 10.1016/S0550-3213(99)00336-3.
- [116] C. Allton et al. Physical Results from 2+1 Flavor Domain Wall QCD and SU(2) Chiral Perturbation Theory. *Phys.Rev.*, D78:114509, 2008. doi: 10.1103/PhysRevD.78.114509.
- [117] F. Bahr et al. $|V_{ub}|$ determination in lattice QCD. arXiv:1211.6327, 2012.
- [118] Felix Bahr, Fabio Bernardoni, Alberto Ramos, Hubert Simma, Rainer Sommer, et al. $B \rightarrow \pi$ form factor with 2 flavours of $O(a)$ improved Wilson quarks. *PoS, LATTICE2012*:110, 2012.
- [119] F. Bernardoni, B. Blossier, J. Bulava, M. Della Morte, P. Fritzsche, et al. B-physics from HQET in two-flavour lattice QCD, 2012.
- [120] Benoit Blossier, John Bulava, Michele Della Morte, Michael Donnellan, Patrick Fritzsche, et al. M_B and f_B from non-perturbatively renormalized HQET with $N_f=2$ light quarks. *PoS, LATTICE2011*:280, 2011.
- [121] Bastian B. Brandt, Anthony Francis, Harvey B. Meyer, Owe Philipsen, and Hartmut Wittig. QCD thermodynamics with two flavours of Wilson fermions on large lattices. *PoS, LATTICE2012*:073, 2012.

- [122] Bastian B. Brandt, Anthony Francis, Harvey B. Meyer, and Hartmut Wittig. Thermal Correlators in the rho channel of two-flavor QCD. *JHEP*, 1303:100, 2013. doi: 10.1007/JHEP03(2013)100.
- [123] Stefano Capitani, Michele Della Morte, Georg von Hippel, Bastian Knippschild, and Hartmut Wittig. Scale setting via the Omega baryon mass. *PoS, LATTICE2011*:145, 2011.
- [124] Luigi Del Debbio, Haralambos Panagopoulos, and Ettore Vicari. Theta dependence of $su(n)$ gauge theories. *JHEP*, 0208:044, 2002.
- [125] M. Guagnelli, J. Heitger, C. Pena, S. Sint, and A. Vladikas. Non-perturbative renormalization of left-left four-fermion operators in quenched lattice QCD. *JHEP*, 0603:088, 2006. doi: 10.1088/1126-6708/2006/03/088.
- [126] Filippo Palombi, Carlos Pena, and Stefan Sint. A Perturbative study of two four-quark operators in finite volume renormalization schemes. *JHEP*, 0603:089, 2006. doi: 10.1088/1126-6708/2006/03/089.
- [127] Martin Luscher. Properties and uses of the Wilson flow in lattice QCD. *JHEP*, 1008:071, 2010. doi: 10.1007/JHEP08(2010)071.
- [128] Zoltan Fodor, Kieran Holland, Julius Kuti, Daniel Negradi, and Chik Him Wong. The Yang-Mills gradient flow in finite volume. *JHEP*, 1211:007, 2012. doi: 10.1007/JHEP11(2012)007.
- [129] Zoltan Fodor, Kieran Holland, Julius Kuti, Daniel Negradi, and Chik Him Wong. The gradient flow running coupling scheme. *PoS, LATTICE2012*:050, 2012.
- [130] Patrick Fritzsche and Alberto Ramos. The gradient flow coupling in the Schrödinger Functional. arXiv:1301.4388, 2013.
- [131] Stefan Schaefer, Rainer Sommer, and Francesco Virotta. Investigating the critical slowing down of QCD simulations. *PoS, LAT2009*:032, 2009.
- [132] Stefan Sint and Peter Weisz. Further results on $O(a)$ improved lattice QCD to one loop order of perturbation theory. *Nucl.Phys.*, B502:251–268, 1997. doi: 10.1016/S0550-3213(97)00372-6.

List of Figures

2.1	Illustration of the two dimensional lattice, with its characteristic objects used in lattice QCD.	10
3.1	Quenched vs. dynamical fermions simulations.	37
3.2	Computer resources as a function of the quark mass “Berlin Wall” figure.	38
3.3	Illustration of the lattice covered by non-overlapping blocks.	40
4.1	Scaling of the DD-HMC algorithm with different solver types. . . .	45
4.2	Diagrams of the contributions to F_μ^{SW}	51
4.3	Diagrams of the contributions to F_μ^{det}	53
4.4	Histories of the energy violation ΔH , the maximum and average forces F_2 and F_1	57
4.5	Average plaquette and the theoretical acceptance with the cut of the forces	58
4.6	Scaling of the MP-HMC program package	60
5.1	Illustration of the Schrödinger functional (SF) space-time manifold	67
5.2	Scaling of the SF-MP-HMC code for $N_f = 2$ flavors of dynamical fermions.	74
5.3	Scaling of the SF-MP-HMC code for $N_f = 4$ flavors of dynamical fermions.	75
5.4	History of the energy violation ΔH in the SF-MP-HMC run	76
6.1	A sketch of the recursive finite-size scaling method used in the computation of the SF coupling \bar{g} at different energy scales $\mu = 1/L$	78
6.2	Different estimations of the improvement coefficient c_A	84
6.3	The running coupling in $N_f = 4$ obtained from the simulation data in [21]	86
6.4	Non-perturbative estimation of the derivative $\frac{\partial \bar{g}^2(2L)}{\partial z}$: $\Phi(a/L)$ as a function of \bar{g}^2	89
6.5	The <i>improved</i> lattice step scaling function $\Sigma^{(2)}(u, L/a)$ for $N_f = 4$ theory	92
6.6	The extrapolation of SSF at $u = 0.9629$ for $L = 6, 8$ data as a check of the cutoff effects	96

List of Figures

6.7	Continuum step scaling function for $N_f = 4$ theory	97
6.8	The running coupling in $N_f = 4$ obtained from the simulations summarized in section 6.5.1	100
7.1	A sketch of the two approaches for chiral extrapolation to the phys- ical point.	104
7.2	Chiral extrapolation of the kaon decay constant in lattice units for all three values of β	105
7.3	Detailed comparison of strategy 1, strategy 2 and a linear extrapo- lation at $\beta = 5.5$	107
7.4	Continuum extrapolation of the product of lattice kaon decay con- stant f_K and matching scale L_1 , defined with $\bar{g}^2(L_1) = 4.484$	110
7.5	Left: Chiral extrapolation of the strange quark mass according to strategy 1. Right: Continuum extrapolation of the strange quark mass in units of f_K	114
1	Tuning of the kappa critical for L=12 lattices	127
2	Autocorrelation function of $dS_G/d\eta$ for the L=12 lattice	130
3	Autocorrelation function of f_K for the O7 lattice	131

List of Tables

1.1	Determination of the Lambda parameter from lattice gauge theory and perturbation theory estimations	4
2.1	Non-perturbative determinations of the Sheikholeslami-Wohlert coefficient c_{SW} for different number of dynamical quark flavors N_f . .	18
4.1	Distribution of the total time of a single MP-HMC trajectory into different types of computation.	62
4.2	Comparison of the mass preconditioned version of the HMC algorithm with DD-HMC	63
4.3	Overview of the ensembles generated with MP-HMC.	64
4.4	Overview of the HMC parameters used in the simulations.	64
6.1	The renormalized coupling results for two $L/a = 8$ simulations obtained in Ref. [21]	88
6.2	The renormalized coupling \bar{g}^2 and the tuned PCAC mass from the simulations of $L/a = 6$ and $L/a = 12$ lattices.	91
6.3	The renormalized coupling \bar{g}^2 and the tuned PCAC mass from the simulations of $L/a = 6$ and $L/a = 12$ lattices	91
6.4	The renormalized coupling \bar{g}^2 and the tuned PCAC mass from the simulations of $L/a = 12$ and $L/a = 24$ lattices	91
6.5	Discretization errors of the SSF (eq. 6.36) for $N_f = 4$ and $L/a = 6, 8, 12$	93
6.6	Results for $\Sigma(u, a/L)$ and $\Sigma^{(2)}(u, a/L)$ for lattice sizes $L/a = 6, 8$ and couplings u	94
6.7	Continuum extrapolation of the step scaling function	95
6.8	Values estimated for $\ln(\Lambda L_{\max})$ for the value of L_{\max} set with $\bar{g}^2(L_{\max}) = 3.45$. We take our final result from the step $i = 9$	98
7.1	Overview of the ensembles used in the study of the Lambda parameter and the strange quark mass in $N_f = 2$ theory.	102
7.2	Lattice spacings from the first strategy obtained by applying SU(3) ChPT and from the second strategy, based on SU(2) ChPT	108
7.3	The kaon decay constant at the physical quark mass and the corresponding lattice spacing	110

List of Tables

7.4	Values of L_1/a , $L_1 f_K$, r_0/L_1 and \overline{m}_s/f_K at the three values of β	111
1	Parameters of the DD-HMC algorithm for the ensembles used in this thesis	124
2	Parameters of the MP-HMC algorithm for the ensembles used in this thesis	124
3	Values of \bar{g}^2 and am_1 from old $L/a = 6$ simulations and the required limit on am_1	125
4	Values of \bar{g}^2 and am_1 from old $L/a = 8$ simulations and the required limit on am_1	126
5	The required limit on am_1 for $L/a = 12$	126